Fabrication of Distributed Feedback Devices Using X-ray Lithography

by

Vincent V. Wong

S. B., Massachusetts Institute of Technology (1991)
S. M., Massachusetts Institute of Technology (1991)

Submitted to the Department of Electrical Engineering and Computer Science
in partial fulfillment of the requirements for the degree of

Doctor of Philosophy

at the

MASSACHUSETTS INSTITUTE OF TECHNOLOGY

August 1995

Author ....
Department of Electrical Engineering and Computer Science
August 4, 1995

Certified by ....
Henry I. Smith
Joseph F. and Nancy P. Keithley Professor of Electrical Engineering
Thesis Supervisor

Accepted by ....
Frederic R. Morgenthaler
Chairman, Departmental Committee on Graduate Students

Fabrication of Distributed Feedback Devices Using X-ray Lithography

by

Vincent V. Wong

Submitted to the Department of Electrical Engineering and Computer Science
on August 4, 1995, in partial fulfillment of the
requirements for the degree of
Doctor of Philosophy

Abstract

Distributed feedback structures are essential for many applications in optics where wavelength-selectivity is required. This thesis focuses on the development of nanofabrication techniques for the fabrication of distributed feedback devices for optical communications. The distributed feedback laser and Bragg-grating-based optical filters - single-pole, multiple-pole and integrated resonant channel-dropping filters - are technology drivers to demonstrate these nanofabrication techniques. A combination of holographic, spatial-phase-locked electron-beam lithography and x-ray lithography is used to fabricate the necessary phase-coherent grating structures. A laterally-coupled distributed-feedback laser is proposed which offers the potential for simpler processing and consequently higher yields. Computer simulations are performed which indicate that such a device structure provides sufficient coupling for laser action. A novel technique based on ion implantation is developed for patterning lateral gratings on deep ridge waveguides. Finally, high-quality single-pole, quarter-wave-shifted Bragg resonators, the building block of the integrated resonant channel-dropping filter, are fabricated in a silica-on-silicon materials system using a self-aligned process and step-and-repeat x-ray lithography. The first demonstration of multiple-pole optical filters is also presented.

Thesis Supervisor: Henry I. Smith
Title: Joseph F. and Nancy P. Keithley Professor of Electrical Engineering

Thesis Reader: Hermann A. Haus
Title: Institute Professor, Professor of Electrical Engineering

Thesis Reader: Clifton G. Fonstad
Title: Professor of Electrical Engineering

Acknowledgments

I have truly benefited from the guidance, expertise and support (both technical and moral) offered to me by many individuals. To these individuals, I would like to express my most sincere appreciation.

I thank Professor Hank Smith for taking me on as a privileged member of the NanoStructures Lab. He has provided both insight and encouragement throughout the course of this work. I thank him for instilling upon me know-how and philosophy which I will carry with me and use in the 'real world' for many years to come. I thank him for always keeping his door open, for always being willing to roll-up his sleeves, and for always providing a clear path towards the solution to a problem. Finally, I thank him for being a good tennis partner. I can only hope to play as well as he does in the years to come.

Without question working with the rest of the 'CDF gang' - Jay Damask, Juan Ferrera and Tom Murphy - has been one of the most rewarding aspects of my stay here at MIT. I thank them for being not only colleagues, but also friends. Together we have reveled in the successes we've achieved as well as pondered the puzzles we've encountered. Jay, who has almost single-handedly developed all of the theory for these devices, has provided us all with a good intuitive understanding of device operation as well as a good laugh. Juan has contributed tremendously in the development of the spatial-phase-locked e-beam lithography, without which none of this work would have been possible. His easy-going nature has made working with him that much more enjoyable. Tom, with his wit and wisdom, has in the short period of time he has been in the group made significant contributions on both experimental (RIE processing) and theoretical (waveguide modeling) fronts. The work presented on the Bragg-grating-based optical filters is not so much my work as it is *our* work. It has truly been a 'team effort'. Thanx, guys!

I can truly attest (as can any student working in the NSL) that none of the work in this thesis would have been possible without the help of our fearless leader, Jimmy Carter. His methods of subtle (and sometimes not-so-subtle) manipulation and brute force have kept the lab running smoothly for many generations of students and undoubtedly will do so for many more. Jimmy also performed the numerous holographic exposures which were required in this work. The patience and care with which he performed these exposures are acknowledged with my deepest appreciation.

I thank Mark Mondol for doing many hundreds of evaporations for me. I also thank him for passing the time in the clean room with many lively discussions on topics (among many) ranging from David Letterman to David Letterman to David Letterman.

Thanks go to Professor Hermann Haus and Professor Clifton Fonstad for their comments and suggestions to the manuscript. I also thank Professor Haus for his consistent verve and vitality with regards to our work. His god-like insight is only rivaled by his genuine enthusiasm.

Many thanks go to my fellow graduate students, some of whom have moved on to 'bigger-and-better things' and others who are working diligently to strive for the same. I thank Dr. Martin Burkhardt for providing both technical and moral support. There was a great deal of overlap in our work in the lab. I thank him for sharing his problems with me as well as listening to my problems. I also thank him for acting as a 'watchtower', as I have avoided many pitfalls because of his 'watchful eye'! I am indebted to Dr. Scott Hector, who I first met my sophomore year at MIT Lincoln Lab, for always showing wholehearted interest in both my work and well-being. The theoretical tools which Scott developed have helped provide both understanding and insight on many an occasion. I thank Dr. Yao-Ching Ku, Dr. William Chu and Dr. Ray Ghanbari for bringing me up-to-speed on the learning curve as an undergraduate UROP as well as an incoming graduate student. Their patience and enthusiasm served as examples for me when I was in their position. Dr. Woo-Young Choi must also be thanked for sharing his excitement and expertise with me. Many other NSL students and staff have provided aid along the way: Euclid Moon, Isabel Yang, David Carter, Kenneth Yee, Nitin Gupta, Timothy Savas, Scott Silverman and Anto Yasaka. I also thank Jerry Chen for assistance with the beam-propagation software and Paul Martin for getting me started on the RIE of InP.

I have also benefited from working with members of the Center of Space Research. I thank Rich Aucoin for many useful discussions on fabrication technology, Jeannie Porter for spending much of her time training me as well as for always offering a cheery 'Hi Vince!' to me, Bob 'Seinfeld' Sisson for his expert assistance in mask-making and his sense of humor (Junior Mint, anyone?); Bob Fleming for his sociability; and Dr. Mark Schattenburg for always providing suggestions and a flurry of ideas on a moment's notice.

I am also grateful for support and assistance from several sources in industry: Dr. Zheng Wang, Dr. John Wasserbauer and Dr. Dale Flanders of Lasertron for the ridge waveguide samples used in the lateral grating fabrication experiments; Dr. Nobi Tokoro, Dr. Takao Sakase and Peter Maciejowski of Genus, Inc. and Dr. Ted MacIntyre and Kurt Whaley of Eaton, Corp. for performing implants, oftentimes on very short notice; and Dr. Stephen Rishton of IBM for providing expert assistance in e-beam technology.

I thank Paul Tierney and Tim Tyson of the Integrated Circuits Laboratory staff for fabricating optical masks for me in a timely fashion.

I'd also like to thank Monica Bell in the EECS graduate office for her assistance and approachability and Donna Martinez and Michael Weinberg for guiding me around the office over the years.

It is often said that 'your years in college will be the best years of your life'. Years from now when I look back at this period of time in my life, I may very well confirm this statement. My memories will be of the many friendships I made and the good times I enjoyed. I must thank my friends for keeping me sane and smiling for the past nine years: the members of the 'dinner gang' - Dr. Lisa Su, Isabel Yang and Dr. Hang Hu - for being there...not only at dinner, but at all times; Dr. Joseph Kung for his unparalleled excitability and enthusiasm...calm down, Joe!; Kathy Chen always listening, for all the favors and also for the VCR!; Drs. Julie and Curtis Tsai for their hospitality and Julie for the many lunches we never had. It's the thought that counts!; Dr. Albert Young for his carefree outlook and his goodwill; Melanie Sherony for sharing many of her thoughts and experiences with a smile; Ken Yee for bringing me good karma; Dr. Jarvis Jacobs for his optimism; and Roxann Blanchard for the tennis fixes. Good luck against Hank!

I am forever grateful to my very special friend and other-half, Daphne Shih. She wasn't physically in the lab with me; however, she was always with me in her own special way. She has made this thesis possible in more ways than she can know and that I can describe. I thank her for her understanding, her patience, her always-uplifting smile, her trust and her love, especially during the hectic months towards the end of this work. MWOH!

Finally, credit must go to my family for giving me a caring and loving atmosphere to go home to. I thank my sis, Karen, and my bro-in-law, Steve, who I can always turn to in times of need. It seemed not long ago that Karen and I were toddlers preoccupied with sibling rivalry! I also thank my grandparents for their prayers and well-wishes. They, perhaps unaware of the fact, have also contributed to this thesis. An enormous heartfelt thanks go to my parents for their unwavering belief in me, for providing me opportunities that many children can only wish for, and for fostering in me the ideals and virtues which I can always fall back on. Their unconditional love and support has been a mainstay which has both kept me afloat during turbulent times and inspired me further during sunnier times. All that I have ever achieved has been made possible by their upbringing and their sacrifices, and for this I am eternally grateful. Finally, I thank them for always reminding me to 'have some fun'!...I did!

Contents

List of Figures

List of Tables

Chapter 1

Introduction

In this age of the 'information superhighway' optical communications systems are emerging as the most likely candidate for handling the enormous data capacities which are required in applications such as high definition television, interactive video and massively-parallel computing architectures. Figure 1-1 plots propagation loss as a function of wavelength for a conventional optical fiber. As shown, there is a large low-loss window centered about 1.55 μm.

One possible means of utilizing the available optical bandwidth is with a technique called wavelength division multiplexing/demultiplexing (WDM/WDdM). In this scheme, shown schematically in the inset of Figure 1-1, the available optical bandwidth, which measures appoximately 30 nm (given by the gain bandwidth of erbium-doped fiber amplifiers), is filled with many closely-spaced channels. In such a scheme the information capacity increases linearly with the number of channels transmitted in the fiber. The basic idea is to pack these channels as close together as possible. A typical channel spacing (i.e. $\Delta\nu$) is 50 GHz, corresponding to an equivalent channel spacing (i.e. $\Delta\lambda$) of 0.4 nm (at $\lambda = 1.55$ μm). Therefore, approximately 75 channels can be multiplexed within a 30 nm bandwidth. Each of these channels can be modulated electronically at approximately 10 GHz, providing a total information capacity of 750 GHz. This capacity far exceeds that which is possible in systems

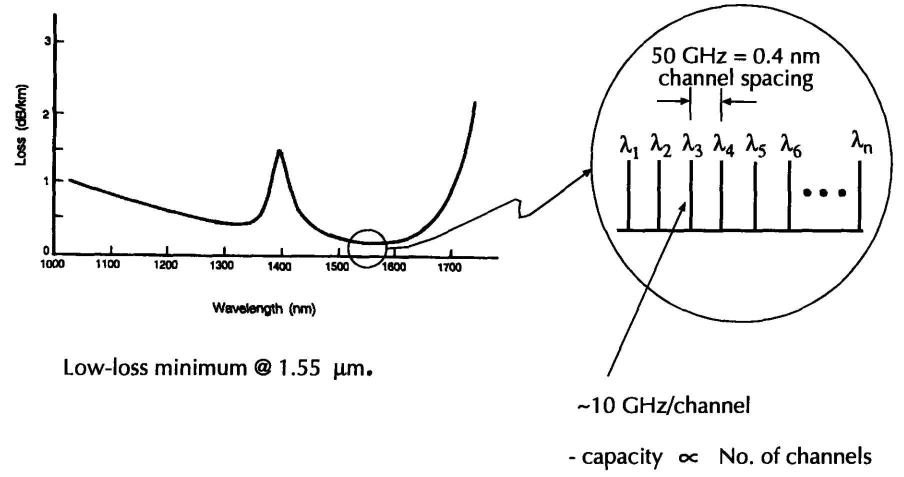

Figure 1-1: Loss versus wavelength for a conventional optical fiber.

operating solely via electronic means.

A schematic of a WDM/WDdM system is shown in Figure 1-2. The basic components are the transmitters, multiplexer, optical fiber, demultiplexer and detectors. There are many technological issues involved in the construction of a WDM/WDdM system. We consider the laser transmitter and the demultiplexing components in more detail. The signals from each of the laser transmitters, when multiplexed together, form a multi-frequency 'bit stream' which propagates along the optical fiber. The lasers must operate in a single longitudinal mode with a narrow linewidth to minimize the effects of mode partition noise and pulse-spreading due to fiber dispersion, and also to minimize the channel spacing of the WDM bit stream. They should also have 3 dB-bandwidths of least 10 GHz, offer tunability for system flexibility and be monolithically-integrable with other devices such as external modulators and detectors for low-cost optoelectronic circuits.

The most promising candidate for high-performance laser transmitters for WDM/WDdM systems is the distributed feedback (DFB) laser. DFB lasers have demonstrated single longitudinal mode oscillation with side-mode suppression ratios of greater than 50 dB [1], with sub-MHz linewidths [2] and with frequency modulation bandwidths

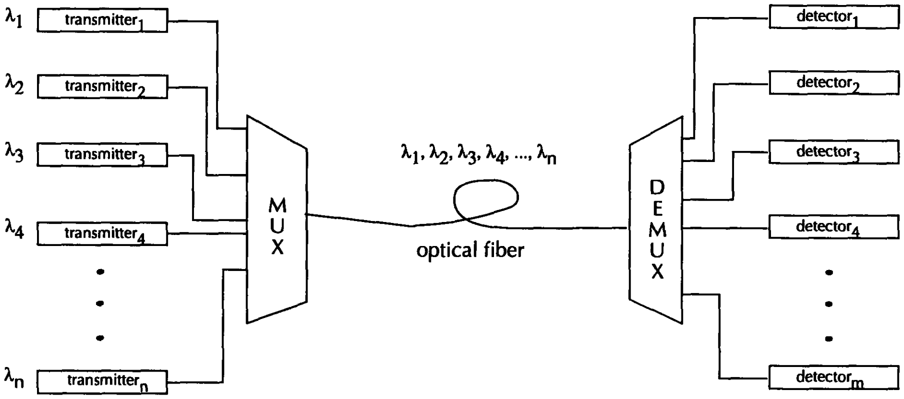

Figure 1-2: Schematic of a WDM system.

(3 dB) exceeding 10 GHz [3]. Continuous tuning over several nanometers has also been demonstrated with multiple-section DFB lasers [4]. These lasers have also been monolithically integrated with electroabsorption modulators [5,6] and detectors [7]. Arrays of DFB lasers have also been demonstrated which can be used to multiplex up to 20 signals together to form a WDM bit stream [8].

At the fiber output, demultiplexers serve to resolve the 'bit stream' for further processing or detection. Demultiplexers can be classified into two forms: full spectral resolvers [9,10] and channel-dropping filters (CDFs) [11–15]. Full-spectral resolvers terminate the entire bit stream, while channel-dropping filters tap a single channel from the bit stream without disturbing the remaining signals. Full-spectral resolvers demultiplex the bit stream in parallel and are relatively easy to fabricate. Because of their parallel nature, however, they limit the system architecture. Channel-dropping filters, on the other hand, offer much more flexibility in architecture design. Within this class of devices the integrated resonant channel-dropping filter proposed by Haus, *et al.* [13] promises to offer the highest performance, and it is this type of filter that this thesis work focuses on.

The integrated resonant CDF, like the DFB laser, is a grating-based device. These devices rely on the phenomenon of distributed feedback. The two basic grating structures of interest are the uniform and the quarter-wave-shifted (QWS) grating. The QWS grating is formed by joining two uniform grating sections (period, $\Lambda = \lambda/2$ for 1st-order gratings) together separated by a $\Lambda/2$-shift, corresponding to a $\lambda/4$-shift. These two grating structures form the basis for more complicated devices which rely on multiple QWS gratings [13,16–19] and provide the necessary frequency-selectivity for defining the laser wavelength in the case of the DFB laser and for filtering the appropriate signal out of the WDM bit stream in the case of the integrated resonant CDF.

A key point in understanding the operation of grating-based devices is that the nanostructures one fabricates must interact with coherent optical waves. These waves have the property of long range phase coherence. Because of this fact, the nanostructures one fabricates must preserve the phase coherence of the waves for optimal device operation. That is, the gratings must be spatially-coherent. In this way the frequency-selectivity and spectral properties of the nanostructures can be tailored and engineered.

This thesis focuses on the development of nanolithographic techniques for the fabrication of grating-based optical devices. The DFB laser and the integrated resonant CDF are technology drivers to demonstrate these nanofabrication techniques. As will be described, a combination of holographic lithography, spatial-phase-locked electron-beam lithography and x-ray lithography is used to fabricate the necessary device grating patterns. The grating patterns are first patterned onto silicon nitride x-ray masks [20] by either holographic or spatial-phase-locked electron-beam lithography, both of which have demonstrated the capability of defining gratings with long range phase coherence [21,22]. X-ray lithography (XRL) [23] is then used to pattern transfer these gratings onto device substrates. XRL is used for the pattern transfer as opposed to performing holographic or electron-beam lithography directly on the device substrates for several reasons.

XRL offers superior process latitude over other competing lithography technologies. The physical mechanism which gives rise to this advantage is that in all materials the real part of the refractive index is ≈ 1 (e.g. 0.999). Consequently, in the x-ray regime the impedance mismatch and, therefore, the reflection at interfaces is negligible. This property makes the pattern transfer process independent of substrate topography and substrate material, which is not the case for either holographic lithography or electron-beam lithography. XRL also offers a large depth-of-focus which allows good linewidth control in thick resists layers. Finally, XRL is inherently a parallel process which is compatible with the throughput requirements in a manufacturing environment. Much of the work in this thesis involves the patterning of x-ray masks and the subsequent pattern transfer processes using these masks for the fabrication of grating-based devices.

Chapter 2 describes the means of fabricating the necessary grating patterns onto silicon nitride mesa-style x-ray masks by holographic lithography and gold electroplating. These techniques are applied to the fabrication of large-area uniform gratings for direct pattern transfer onto device substrates and "segmented" fiducial gratings for spatial-phase-locked electron-beam lithography. Uniform-grating x-ray masks of 6 different grating periods ranging from 200 nm to 511 nm have been made as well as segmented fiducial grating masks of period 230 nm and 511 nm. Two-dimensional gratings, that is, grids, of period 230 nm have also been fabricated onto x-ray masks. Finally, a process is proposed which combines both holographic and x-ray lithography for patterning $\lambda/4$-shifted gratings on an x-ray mask.

Chapter 3 discusses a laterally-coupled (LC) DFB laser structure. This structure avoids the epitaxial overgrowth process with which conventional DFB lasers are fabricated and, therefore, can potentially offer higher device yields and reliability. Computer simulations for 1st-order and 2nd-order lasers show that such a device structure offers sufficient coupling for laser action. The simulations also show that the grating duty cycle can be used to improve device performance. A technique to 'fine-tune' the grating duty cycle on x-ray masks is described and demonstrated. One of the more challenging aspects of the LC-DFB is the fabrication of the lateral gratings which involves both lithography and reactive-ion-etching (RIE). Processes are described for fabricating lateral gratings on ridge waveguides. For deeper ridges (i.e. $\geq 1\mu$m-high) a novel application of ion implantation is proposed and demonstrated.

Chapter 4 describes the fabrication of high-quality QWS Bragg resonators, so-called single-pole filters, which are the primary building blocks for the integrated resonant CDF, in a silica-based materials system. The QWS Bragg resonators are defined on an x-ray mask using spatial-phase-locked electron-beam lithography and pattern transferred onto rib waveguides using a self-aligned process along with XRL and RIE. A step-and-repeat procedure, which demonstrates the feasibility of large-scale production with XRL, was utilized in conjunction with ESCAP, a chemically-amplified positive resist. Finally, initial results for the fabrication of higher-order multiple-pole filters are presented and discussed. To obtain accurate control of the etch depth for these higher-order filters, a two-step RIE process is described. Finally, Chapter 5 summarizes the results of the thesis project and suggests some directions for future research.

Chapter 2

Phase-Coherent Grating Fabrication

Our fabrication approach for grating-based devices uses x-ray lithography (XRL) to pattern transfer the Bragg gratings onto the device substrates. As described in the previous section, the Bragg gratings must be spatially-coherent to preserve the coherence of the waves with which they interact. Holographic lithography is well-suited for defining such spatially-coherent gratings. In this chapter the techniques for patterning large-area and segmented spatially-coherent gratings or grids with holographic lithography, RIE and gold electroplating on silicon-nitride mesa x-ray masks are described.

2.1 Background

Holographic lithography in its simplist form involves the formation of a periodic intensity pattern in space by the interference of two coherent beams. This periodic intensity pattern is usually imaged in a resist layer and subsequently pattern transferred onto a substrate material by either liftoff, electroplating or RIE. The substrate material of interest in our lab is typically an x-ray mask.

Both holographic lithography technology and the x-ray mask fabrication technology have undergone significant advances in the NanoStructures Lab at MIT. One of the earliest demonstrations of a grating x-ray mask was by Flanders *et al.* [24,25] in 1978. A 320 nm-period grating was defined in a 100 nm-thick layer of gold on a 0.9 μm-thick layer of polyimide on a silicon substrate by holographic lithography and ion-beam etching. A polyimide membrane was formed by chemically etching the underlying silicon substrate.

Hawryluk *et al.* in 1981 [26] fabricated similar polyimide-membrane grating masks of periods 0.2 and 0.3 μm for x-ray spectroscopy and spatial-period-division. The imaging resist thickness in these earlier works was constrained to be very thin, ~50 - 100 nm, to reduce the effects of orthogonal standing waves on line edge raggedness and processing complexity and reproducibility. Anderson *et al.* [27] in 1983 introduced a technique for producing grating patterns in thick resist layers (~0.5 μm-thick). A grating is formed in the top 100 nm of the resist, then an angled evaporation of chromium (or any alternative masking material) is performed such that only the tops of the resist and part of the sidewalls are coated or 'shadowed'. RIE is then used to etch through the remaining resist layer down to the substrate, after which process steps such as liftoff or electroplating can be performed.

For the sub-μm-period gratings described above, the reproducibility of holographic exposure becomes very sensitive to acoustic noise, mechanical vibrations and air turbulence. Anderson, around 1985, developed an active feedback stabilization technique to 'lock' the standing-wave pattern formed by the two-beam interference [28]. In this way high-contrast interference fringes and consequently high-contrast resist profiles were reliably and routinely achieved. The active feedback system marked a major step forward in the holographic lithography system and to this day remains an essential component of the system. As with the holographic lithography, x-ray mask technology has undergone various stages of development in our lab.

In the earlier work polyimide membranes were used. These membranes, however, suffered from distortion with repeated use. Wrinkling and breakage of the membranes were common. Membranes made from silicon-rich silicon nitride (SiN_x), however, are dimensionally-stable over time and satisfy the requirements of multi-level lithography processes [29]. Consequently, such membranes replaced the polyimide ones.

Initially, SiN_x membranes were formed by depositing a SiN_x film on a silicon wafer and then selectively removing the silicon to define the membrane region. Presently, we are working with mesa-style SiN_x membranes [20] where the membrane is supported by a thin circular silicon rim which itself is bonded to a pyrex© ring for ease of handling. These mesa-style membranes are ideally suited for microgap XRL where the mask and substrate are in close proximity ($\sim 3-5\mu$m) to each other [30–32]. In the present work we describe the techniques for patterning gratings on these mesa-style SiN_x x-ray masks.

2.2 Grating Mask Fabrication

The SiN_x x-ray mask technology was developed by previous graduate students and staff and is described in detail in references [29,33,34]. A schematic of the current SiN_x x-ray mask standard is shown in Figure 2-1. It consists of a 31 mm SiN_x membrane approximately 1 μm-thick supported on a 400 μm-high silicon 'mesa' which itself is anodically-bonded to a 75 mm-diameter pyrex© ring. Techniques have been developed that result in mesas and membranes which are flat to better than 0.1 μm [35] (see Figure 2-2 [36]). The virtue of this mask structure is that the mask and substrate can be brought into close proximity during alignment and lithography where gap setting is crucial.

The processing steps for performing holographic lithography [37] on these x-ray masks are shown schematically in Figure 2-3. A plating base is first evaporated on the membrane. For holographic lithography a plating base of 5 nm NiCr and 20 nm Au is used. This is thicker than the plating base (5 nm NiCr and 10 nm Au) used for

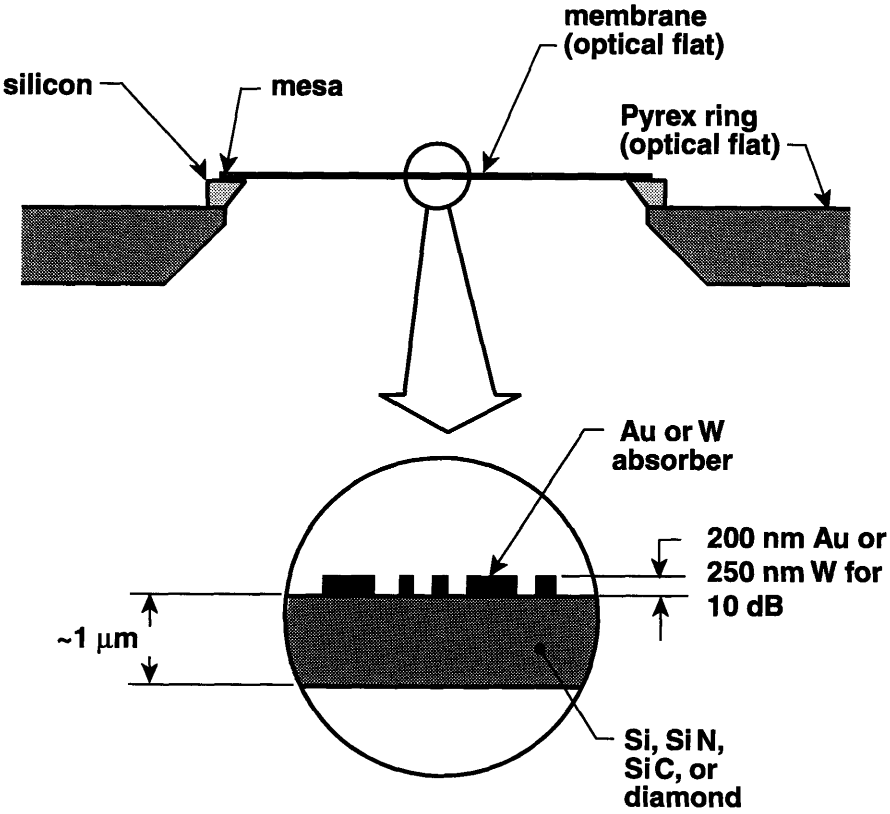

Figure 2-1: Schematic of a mesa-etched x-ray mask.

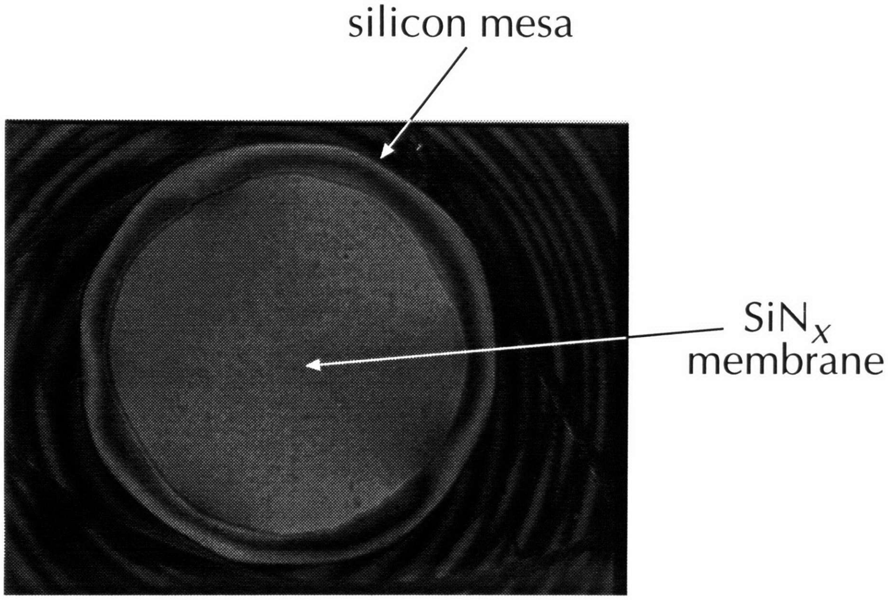

Figure 2-2: Interferogram (λ = 632.8 nm) of a SiN_x x-ray mask. The mesa and membrane area shows a flatness of less than 0.1 μm.

patterns exposed using electron-beam lithography (EBL) or XRL. A thicker layer of Au is used to account for any sputtering of the Au which occurs during the RIE step shown in Figure 2-3.

Following the plating base evaporation, a 350 nm-thick layer of antireflection coating (ARC) is spun-on. This layer serves to eliminate the orthogonal standing waves in the resist which occur due to the high reflectivity of the Au layer. A layer of Shipley 1800 series resist is then spun on to a thickness of $\frac{p}{200}(170)$ nm, where p is the desired grating period. The thickness of the resist scales with the grating period to keep the shadowing angles shown in Figure 2-3 at reasonable values (i.e. between 40 to 60 degrees).

Typically, silicon 'monitor' wafers are prepared along with the membranes for process characterization (i.e. to determine the proper exposure, development and RIE etch times). These 'monitors' are prepared in the same way and at the same time as the membranes. To ensure that the spinning characteristics of the two types

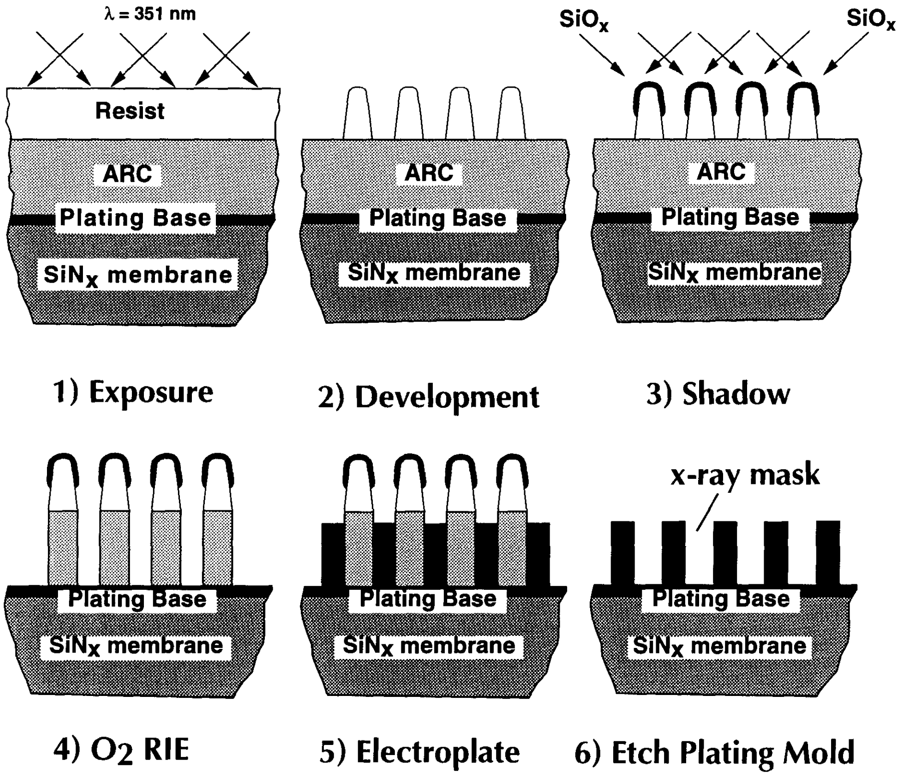

Figure 2-3: Fabrication process for production of holographically-defined gratings.

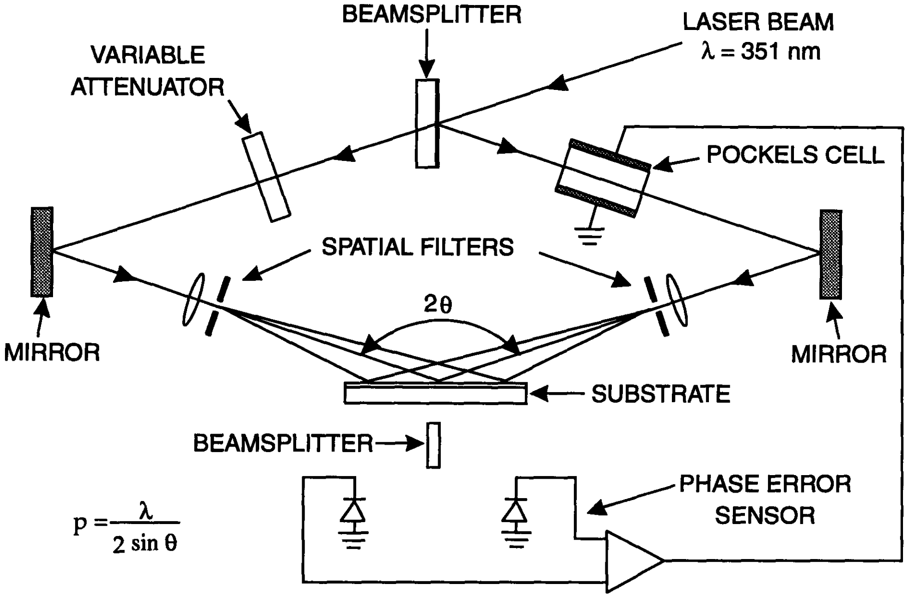

Figure 2-4: Schematic of holographic lithography system. The Pockels cell provides active feedback to keep the path length difference between the two interfering arms constant. This feedback stabilizes the periodic intensity pattern in space which allows high contrast resist profiles to be obtained reproducibly.

of samples are identical, the following experiment was performed.

A silicon wafer and a SiN_x membrane were coated with 700 Å-thick films of aluminum. ARC films were spun-on each of the samples and baked at 180°C for 30 min. The ARC thickness was then measured on both of these samples by ellipsometry at a wavelength of 632.8 nm. At this wavelength, the extinction coefficient in aluminum is 7.65 [38], which translates into an absorption length of 130 Å. Therefore, the underlying layer of aluminum serves to eliminate any thin film effects that occur due to the SiN_x membrane. The measured depths on the silicon wafer and SiN_x membrane were 3239 Å and 3210 Å, respectively, which indicates that there is no significant difference between the spinning characteristics of silicon wafers and mesa-style SiN_x masks.

At this point the holography samples are ready to be exposed. Figure 2-4 is a schematic of our holographic lithography system which incorporates the active feedback system described in the previous section. This system consists of a Pockels cell in one of the arms. This Pockels cell receives a difference signal obtained from two photodiodes located in the plane of the substrate. This signal drives the Pockel cell to keep the phase difference between the two arms forming the standing wave interference pattern constant, thereby stabilizing the standing wave pattern in space.

An argon laser ($\lambda = 351.1$ nm) is used to expose the resist. The grating period, p, is given by the well-known relation

$$p = \frac{\lambda}{2sin\theta} \tag{2.1}$$

where 2θ is the angle of intersection between the two interfering beams. Care was taken to ensure that both the monitors and the mask were exposed in the same plane. If the substrate stage were placed in the same position for both the silicon 'monitor' wafers and the x-ray masks, the planes at which they are exposed are different because of the additional thickness of the pyrex© ring, 4.32 mm. The consequence of exposing the mask at a different plane would be to change the grating period printed onto the mask.

For grating-based devices such as DFB lasers which typically lase efficiently over a wavelength range of several nm's, it is necessary to keep the grating period to within a few tenths of a nanometer. As shown below, the grating period can be controlled to a high degree of accuracy by adjusting the plane at which the sample is exposed. To calculate the dependence of the grating period on the sample location, consider Figure 2-5.

Let the 'monitor' wafer sit at the plane $z = z_w$ and the membrane at $z = z_m$. The pinholes from which the two interfering beams (which we assume to have spherical wavefronts) emerge are located in the plane $z = 0$ at $x = \pm x_o$. From this information the angles of incidence of the two interfering beams, θ_w and θ_m, on the wafer and membrane, respectively, can be calculated. These angles are given by

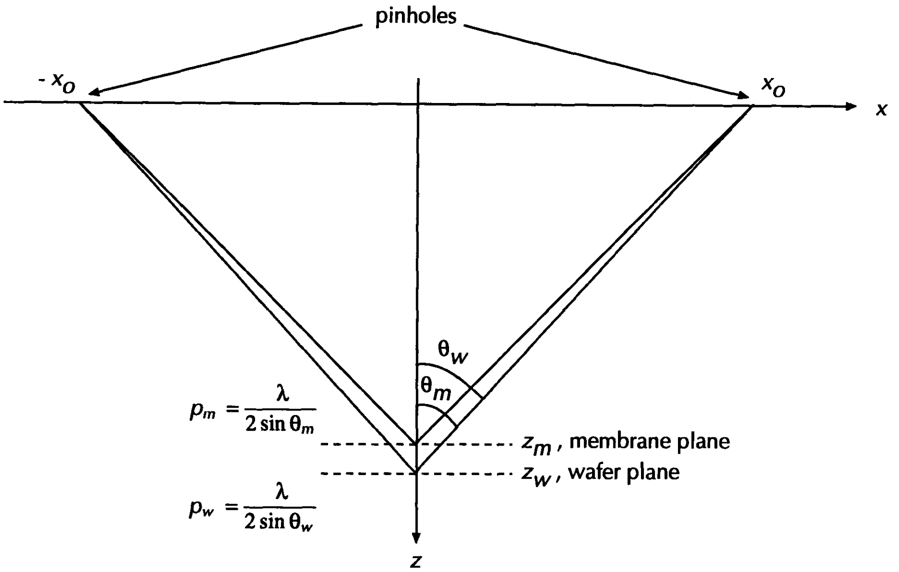

Figure 2-5: Diagram showing the effect of holographic exposures at two different planes.

$$\theta_w = \arctan x_o/z_w \tag{2.2}$$

and

$$\theta_m = \arctan x_o/z_m. \tag{2.3}$$

We first calculate the difference in period that would arise due to the additional thickness of the pyrex© ring. Recall that the grating period, p, is given by Eq. (2.1). In practice the holographic system is set up at a specified angle at the wafer plane to achieve a given grating period. For a typical grating period of 230 nm, this angle is 49.733°. For our holographic system x_o is $\sim$1 m, giving a value of z_w = 0.847072 m and z_m = 0.842754 m. The angle of incidence, θ_m, is 49.877 degrees. The corresponding grating period, therefore, is not 230 nm but 229.5 nm, a difference which could detune the Bragg wavelength away from the desired location.

One can also use the z-dependence of the grating period for fine-tuning the grating period. As shown by the above calculation, very small changes in period can be effected by small changes in z_m. For the distances and periods used above, if we move the plane of the membrane just 10 μm away from the wafer plane, we can change the grating period by 3 parts in 10^4!

After the holographic exposure, the resist is spray-developed in a 1:5 mixture of MF351 developer and DI water. Silicon dioxide (SiO_2) is then shadow-evaporated at the appropriate angle to achieve the desired duty cycle. RIE is then performed to etch through the ARC to expose the plating base. In this work two RIE systems were used. A modified Perkin Elmer 3140-8J model RIE system was used for the initial work and a Plasma Therm 790 model RIE system was used for the more recent work. Currently, all of the RIE work on membranes is performed on the Plasma Therm system.

For the Perkin-Elmer RIE an intermittent etch cycle was used, where each cycle consisted of a 10 s etch in O_2 (15 sccm, 400V, 10 mT) followed by a 90 s latent period. Because of the small thermal mass of the membrane, it can heat up significantly during etching. Such heating causes the resist patterns to flow which degrades linewidth control and, in the worst case, can planarize the resist completely. The intermittent cycle described above maintained the resist profiles during etching. Unlike previous work on the RIE of membranes, diffusion pump oil was not used to coat the backside of the membrane when etching grating patterns.

For the Plasma Therm RIE a continuous etching cycle in an mixture of O_2 and He gases (O_2/He = 2.5/10.0 sccm, 200 V, 7 mT) was used since the system provided for helium backside cooling of the membrane. Helium is introduced between the back surface of the membrane and an Al heat sink at 20°C. (The heat sink was set at 20°C for convenience.) Such cooling has been used in other RIE systems for cooling [39,40] as well as for temperature control during film deposition [41]. It was found for the various etching conditions we were using that lowering the heat sink temperature

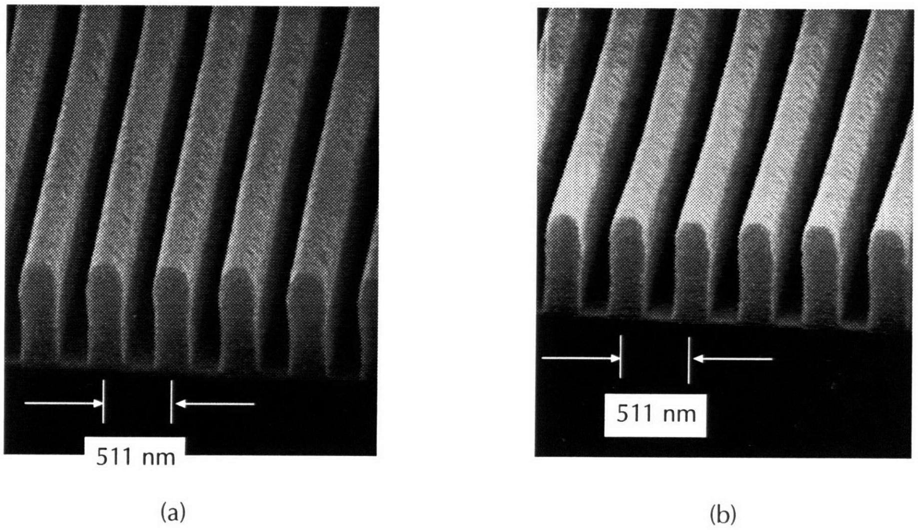

(a) (b)

Figure 2-6: Scanning electron micrographs of resist/ARC profiles of a 511 nm-period grating after O_2/He RIE: (*a*) O_2/He = 2.5/10.0 sccm, 50 V, 7 mT, 20°C and (*b*) O_2/He = 2.5/10.0 sccm, 50 V, 7 mT, -20°C .

below 20°C did not significantly improve the anisotropy of the etch. As an example, Figure 2-6 compares the profiles obtained for two 511 nm-period gratings etched in a mixture of O_2 and He gases (Plasma Therm RIE system, O_2/He = 2.5/10.0 sccm, 50 V, 7 mT). The heat sink temperature for Figure 2-6(*a*) was 20°C and that for Figure 2-6(*b*) was -20°C. As shown, the profiles are essentially the same indicating that the lateral etching due to neutral thermally-activated reactions is nearly the same for the two cases [40]. The results also indicate that very vertical profiles are possible even with 50 V DC bias voltages.

As mentioned above, a 20 nm-thick Au layer (as opposed to the 10 nm-thick layer used for 'mother' and 'daughter' masks) was used as the plating base to allow for the sputtering which occurs for a slight overetch of the ARC. In practice, an overetch of up to 20% was tolerable, after which the plating quality was noticeably degraded. Although the above process worked well, in the future an alternative approach could be taken. One could etch through most of the ARC using a set of parameters which gave a 'fast etch' leaving a thin layer, say 50 nm. Then etch the remaining thin layer with a 'slow etch' where the parameters are chosen to reduce the sputtering rate of the Au. An experiment was performed to determine the relative sputtering rates for the two sets of RIE conditions above: (*i*) O_2/He = 2.5/10.0 sccm, 200 V, 7 mT and (*ii*) O_2/He = 2.5/10.0 sccm, 50 V, 7 mT.

A plating base of 5 nm NiCr and 10 nm Au was evaporated on two silicon wafers. One wafer was reactive-ion-etched for 1 min under the conditions in (*i*) above and the other under the conditions in (*ii*). The basic idea of this experiment is to extract a sputtering rate based on the change in the resistance of a film with thickness. The resistance R of a conductor of length l, width w, thickness δ and resistivity ρ is given by

$$R = \frac{\rho l}{w\delta}. \tag{2.4}$$

As the gold sputters during the RIE, δ decreases which increases the resistance R. ρ can be determined by measuring the resistance of a NiCr/Au stripe on a sample which has not been reactive-ion-etched where we assume a Au thickness of 100 $\mathring{A}$. This assumption is a good one since the film thicknesses are very accurately controlled in the e-beam evaporator. We also assume here that the resistance of the NiCr layer is high enough that measured resistance of NiCr/Au multi-layer can be well-approximated by the resistance of the Au layer alone (since the NiCr and Au layers can be thought of as two resistors in parallel). This approximation is also a good one as the measured resistances of NiCr stripes were $\sim$ 5 kΩ.

After RIE both wafers were processed as follows. Photoresist was spun-on, baked and patterned into stripes approximately 5 mm-wide on each wafer. After resist development, the exposed Au and NiCr regions were removed by wet chemical etching. The resist was removed in acetone and methanol and another layer of resist was spun-on and baked. A masked exposure was then performed to expose one of the Au/NiCr stripes after development. The Au on these exposed stripes was then removed once

material	w (mm)	l (cm)	R_{meas} (Ω)	δ ($\mathring{A}$)
NiCr	6	5	4800	50
NiCr/Au	6	5	65	100

Table 2.1: Measured resistances for NiCr and NiCr/Au lines without RIE.

material	w (mm)	l (cm)	R_{meas} (Ω)	δ ($\mathring{A}$)
NiCr	4.5	5	5500	50
NiCr/Au	4.5	5	225	39

Table 2.2: Measured resistances for NiCr and NiCr/Au lines after 1 min RIE in O_2/He (O_2/He = 2.5/10.0 sccm, 200 V, 7 mT).

again by wet chemical etching leaving a NiCr stripe on the silicon substrate. At this point the resistance of the Au/NiCr and NiCr stripes on each wafer were measured. As a control the resistance of the silicon wafer was measured to be 'infinite' and the resistance of Au/NiCr and NiCr stripes which had not undergone RIE was also measured. The measured results are shown in Tables 2.1, 2.2 and 2.3.

From the above tables we can extract a sputtering rate of 61 $\mathring{A}$/min and 7.8 $\mathring{A}$/min for RIE conditions (*i*) and (*ii*), respectively. Therefore, by utilizing a 'fast etch' and 'slow etch' approach to the RIE of the ARC, one can significantly reduce the sputtering of the Au during a slight overetch. This allows the use of a thinner Au layer, which has the impact of reduced x-ray exposure times.

For both RIE systems it was found experimentally that it took shorter etch times to etch through the ARC on the 'monitor' wafers compared to the membranes. In general, the SiN_x masks took 10-15% longer to etch than the silicon wafer monitors. After the RIE of the ARC, gold electroplating is used to define the gold absorber patterns. Typically, a target plating thickness of 200 nm is used which provides a

material	w (mm)	l (cm)	R_{meas} (Ω)	δ ($\mathring{A}$)
NiCr	4.5	5	5600	50
NiCr/Au	4.5	5	381	22

Table 2.3: Measured resistances for NiCr and NiCr/Au lines after 10 min RIE in O_2/He (O_2/He = 2.5/10.0 sccm, 50 V, 7 mT).

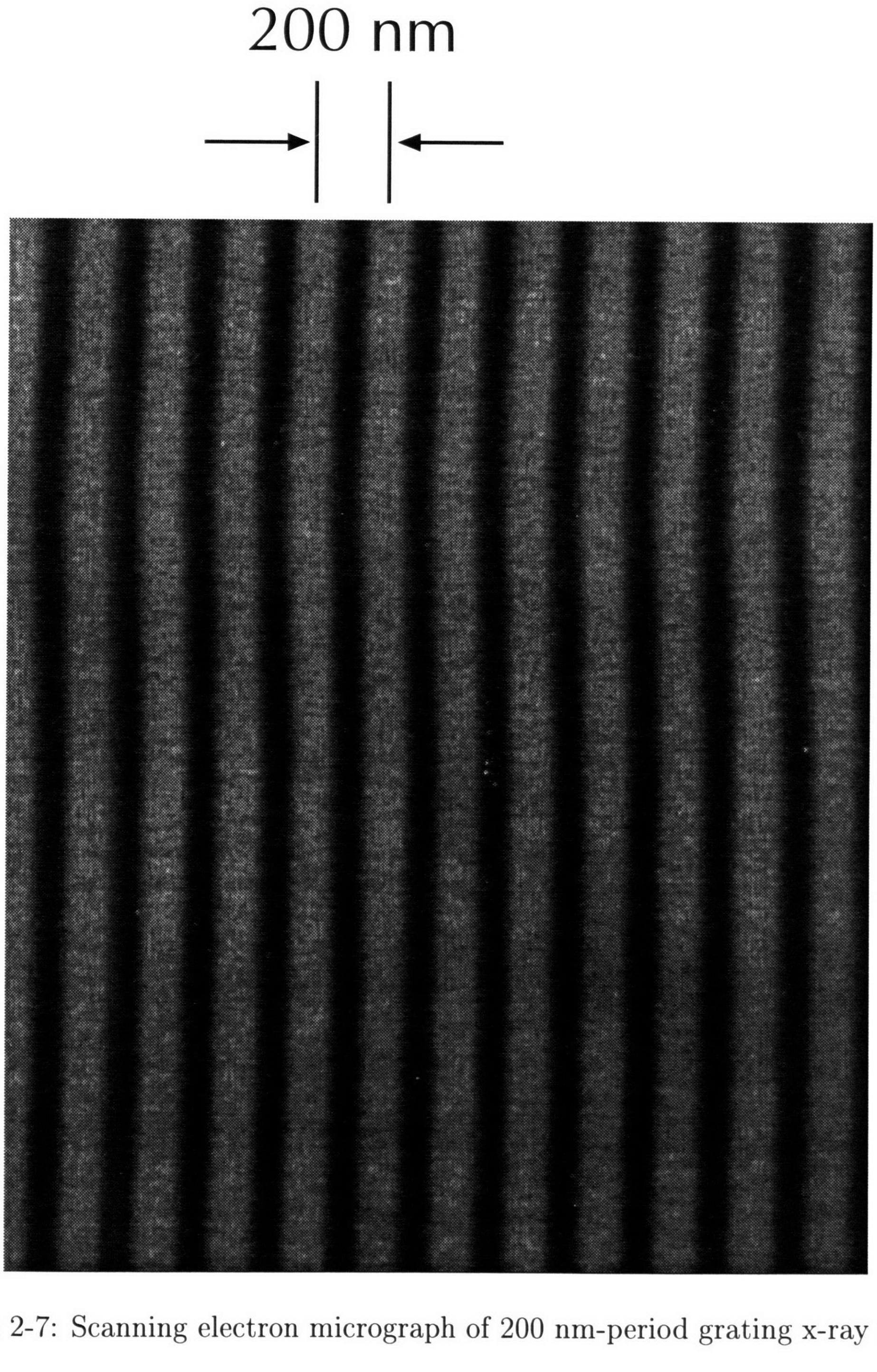

Figure 2-7: Scanning electron micrograph of 200 nm-period grating x-ray mask.

10 dB attenuation at the Cu_L wavelength ($\lambda = 1.32$ nm). A commercially-available plating solution, SEL-REX BDT-510 [42], was used. The plating current density was 0.4 mA/cm^2 and plating bath temperature was held constant at 33^{o}C. The quality of the plating is monitored using a variety of metrics such as the bath pH, bath conductivity and current-voltage measurements, as described in reference [43]. After plating, the SiO_2 is stripped in hydrofluoric acid and the resist and ARC are stripped in an oxygen plasma. Aluminum studs ranging from 3 to 5 μm-tall are evaporated on the mesa of the mask for subsequent 'daughter' mask replication [29]. Grating masks of period 200, 230, 240, 380, 406 and 511 nm were fabricated as described above. Figure 2-7, which shows the electroplated gold patterns on a 200 nm-period SiN_x x-ray mask, is a representative result of the grating fabrication .

2.3 Grid Mask Fabrication

By performing a second holographic exposure oriented at 90^o with respect to the first one in Figure 2-3, two-dimensional grid patterns are generated. Figure 2-8(a) and (b) shows such a 230 nm-period grid pattern. As for a grating after resist development, SiO_2 must be shadowed on the tops of the resist prior to the RIE through the ARC layer. For the desired pattern transfer into the ARC, no SiO_2 should be evaporated in the regions between each of the resist pillars and, as such, the shadow evaporation process is not as straightforward as in the case of grating patterns.

To determine the correct shadowing configuration, a computer model was developed [44]. Figure 2-9 shows the various parameters that are considered in the model. Let the resist grid have a period, p and be aligned to the $x-$ and $y-$axes and the resist pillars have a width, w, and height, h. Given these parameters one needs to specify two angles, θ and ϕ, to determine the shadowing configuration. We define a vector, $\vec{k_{inc}}$, which runs from the effective evaporation source to the substrate and defines the angle of incidence of the SiO_2 onto the substrate. θ is defined as the angle

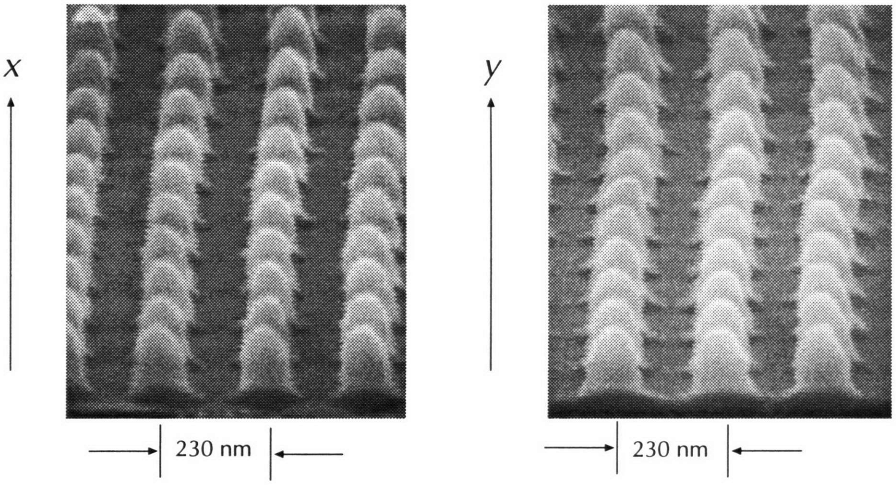

(a) (b)

Figure 2-8: Scanning electron micrograph of 230 nm-period grid pattern in resist along the two perpendicular directions.

between $\vec{k_{inc}}$ and the surface normal of the substrate, $\hat{n}$. ϕ is defined as the angle formed between the $x-$axis and the projection of $\vec{k_{inc}}$ onto the $x-y$ plane.

Note that when SiO_2 is incident on a resist pillar, there will be a region directly behind the pillar which will be 'shadowed' (i.e. not be exposed to the SiO_2). The optimization, therefore, involves the choice of θ and ϕ such that all of the regions between resist pillars are shadowed (i.e. are not exposed to the incident SiO_2 flux). For a given set of parameters, p, w and h, a range of values for θ and ϕ satisfy this requirement. Once acceptable values of θ and ϕ are determined, a double shadow, at ($+\theta$, ϕ) and ($-\theta$, ϕ) is carried out prior to the RIE step.

Figure 2-10 shows a result for the parameters corresponding to the resist profiles in Figure 2-8 (p = 230 nm, w = 0.12 μm, h = 0.17 μm). For this configuration, θ is 75^o and ϕ is 60^o. The grey circles correspond to the resist pillars and the black regions correspond to the regions shadowed by the resist pillars. It was found that θ values larger than 70^o and ϕ values between 55^o and 69^o would provide sufficient shadowing. Note that the model assumes that the resist pillars are perfectly vertical,

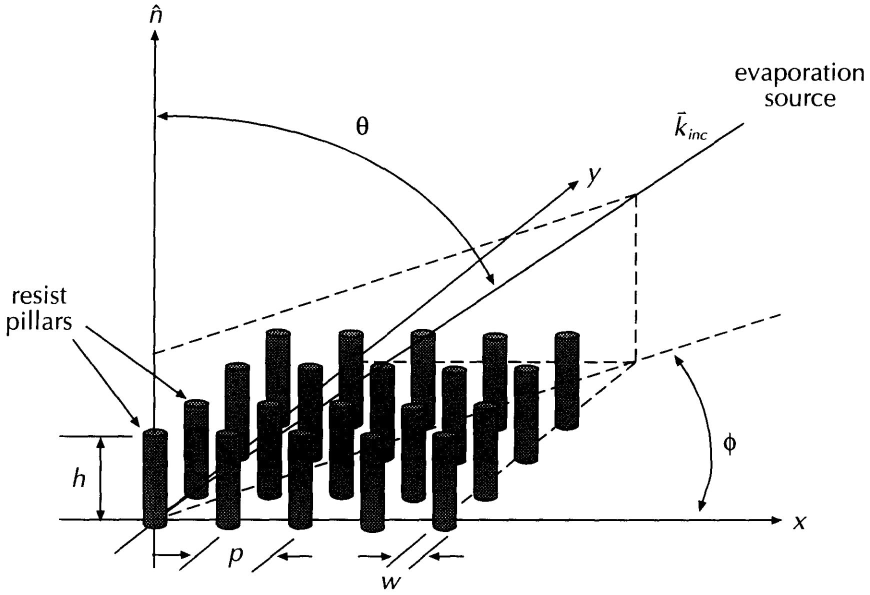

Figure 2-9: Diagram showing the parameters which are considered in computer model of shadowing process for grid patterns.

as depicted in Figure 2-9. However, in reality these pillars are non-vertical as shown in Figure 2-8. Therefore, in practice one should choose a θ value slightly above the minimum acceptable value and a ϕ value near the middle of the acceptable range of values determined from the model. Of course, effort should be made to obtain optimal resist profiles as well.

Figure 2-11(*a*) and (*b*) show the result after an O_2 RIE (Perkin Elmer system, 15 sccm, 400 V, 10 mT, intermittent etch: 10 s on/90 s off, total etch time of 4 m 30 s) through the ARC for the resist profiles in Figure 2-8(*a*) and (*b*). In this example, θ and ϕ were 75^o and 60^o, respectively. Figure 2-12(*a*) shows a top view of the grid pattern of Figure 2-11 after gold electroplating and removal of the SiO_2, resist and ARC. Figure 2-12(*b*) shows a top view of a SiN_x x-ray mask fabricated in the same manner. The grid pattern is evident, although the gold is slightly overplated.

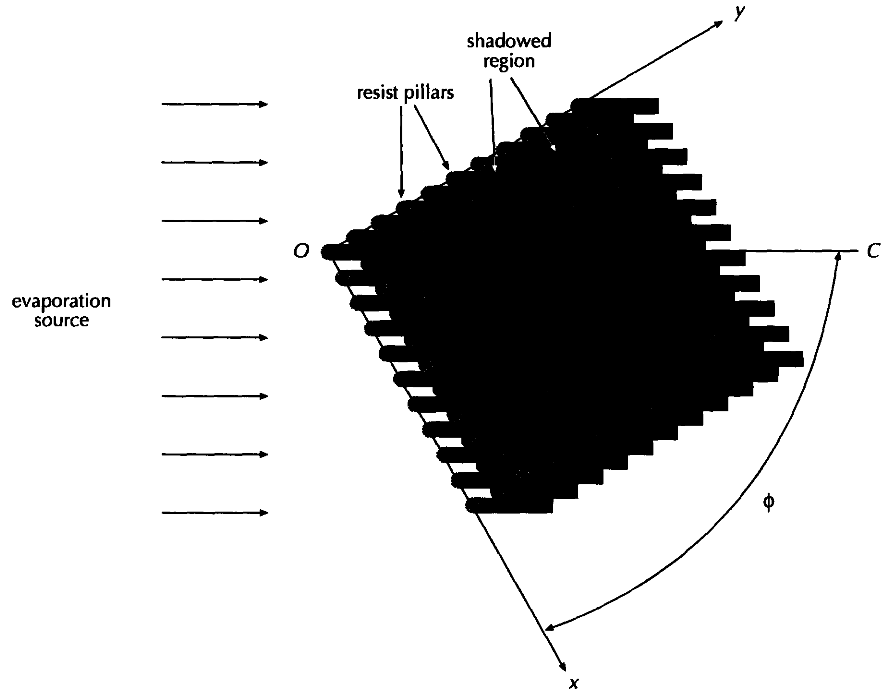

Figure 2-10: Plot showing an acceptable shadowing configuration for the resist profiles in Figure 2-8. The resist height, resist width, θ and ϕ are 0.17 μm and 0.12 μm, 75^o and 60^o, respectively. θ lies in the plane determined by the segment OC and the z-axis.

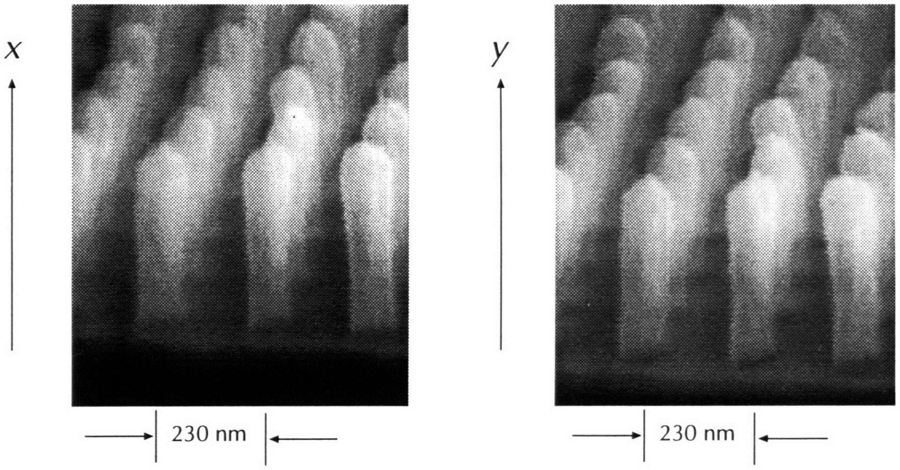

(a) (b)

Figure 2-11: Scanning electron micrograph showing resist and ARC profiles after the RIE of the profiles in Figure 2-8.

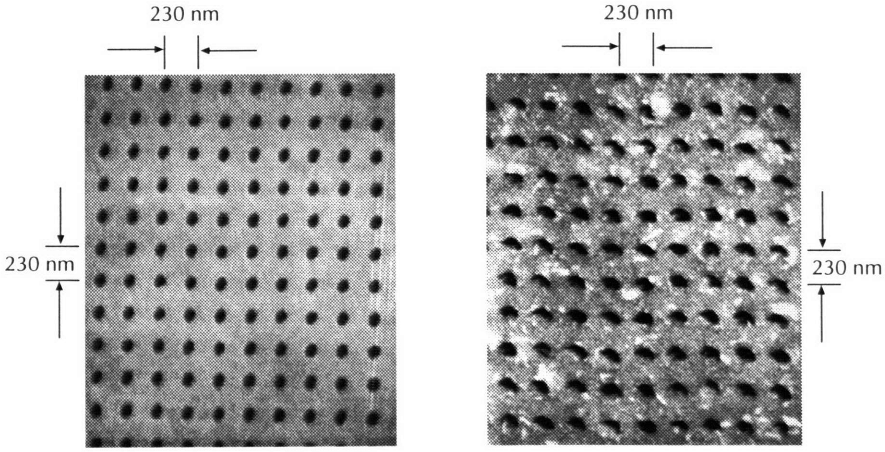

(a) (b)

Figure 2-12: Scanning electron micrograph of grid patterns after gold electroplating and removal of SiO_2, resist and ARC: (*a*) patterned on the 'monitor' wafer of Figure 2-11 and (*b*) patterned on a SiN_x membrane.

2.4 Segmented Fiducial Grating Fabrication

The processes described in the previous section are used to pattern continuous spatially-coherent gratings or grids over large-areas. The spatial coherence of these gratings can be utilized in a new paradigm of EBL called spatial-phase-locked (SPL) EBL [22,45–47]. The essential point of the technique is that all of the e-beam patterning is referenced to a spatially-coherent pattern, either a grating or a grid, residing *directly* on the substrate. This technique provides direct information about the sample-to-beam displacement and does not rely on secondary referencing techniques which measure the position of the stage on which the sample sits e.g., with an interferometer. Furthermore, because periodic structures are used as the reference marks, well-established Fourier-domain methods can be used for the signal processing.

In our initial implementation of SPLEBL, we chose to use a so-called "segmented fiducial grating" scheme. That is, a segmented holographically-defined fiducial reference grating is patterned on the x-ray mask, shown schematically in the upper part of Figure 2-13. The "segments" refer to the fact that the grating does not span the entire membrane area. Rather, it is restricted to reside at designated locations over the membrane area. The segments of the fiducial reference grating are called fiducial rectangles. Over the course of the project, three methods, which are described below, were developed to define the fiducial rectangles and segmented fiducial gratings. SPLEBL was used to define the appropriate device gratings, shown schematically in the lower part of Figure 2-13, on masks prepared using each of these three segmented fiducial grating fabrication techniques. The last method described below is the one presently being used.

The first method begins with the fabrication of a large-area uniform grating 'mother' mask using the methods described in section 2.2. The 'mother' mask is replicated into a 'daughter' mask by XRL and gold electroplating. Optical photoresist is then spun-on the daughter mask, and an optical UV exposure performed. The optical mask that is used contains the rectangles that will define the regions of

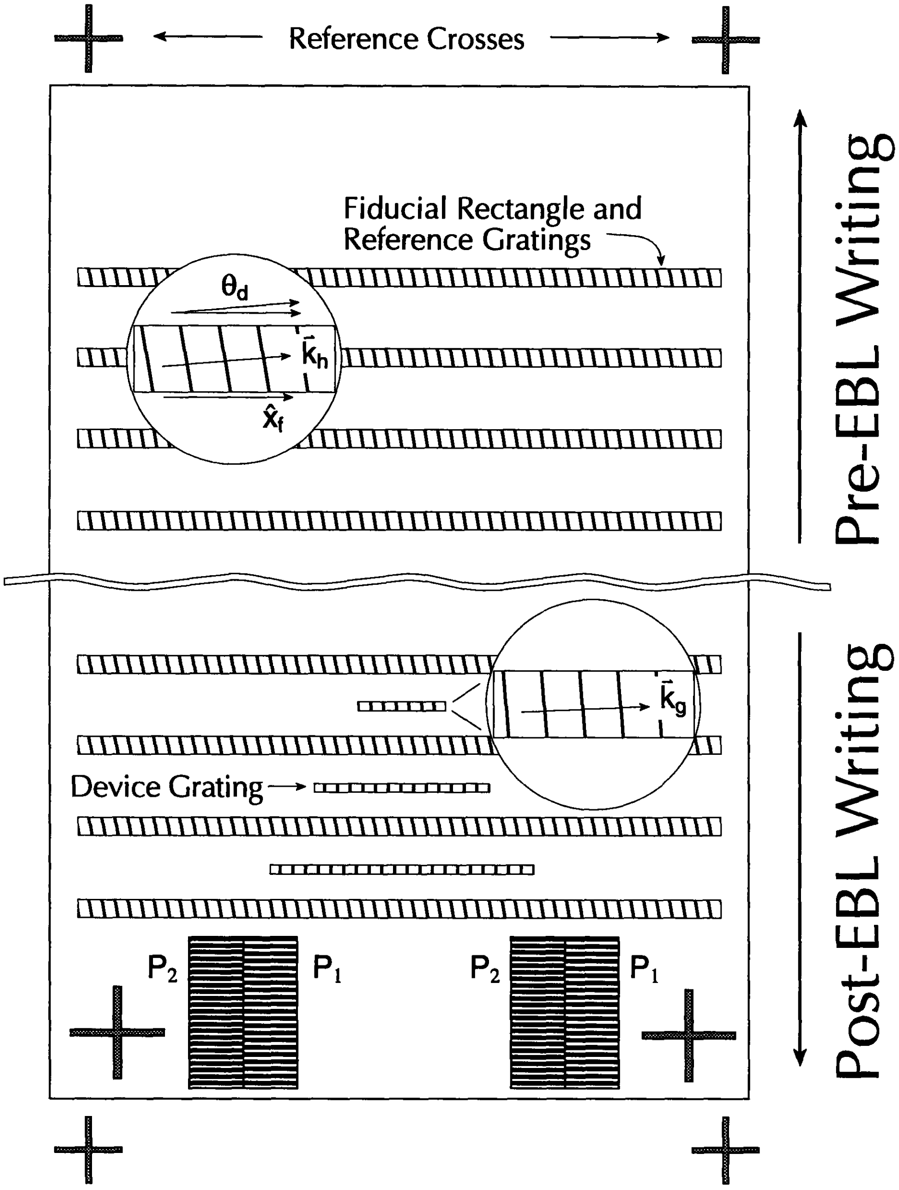

Figure 2-13: Schematic of fiducial rectangles and reference gratings.

the segmented fiducial grating. After resist development, the exposed Au and NiCr regions are removed by wet chemical etching. The resist is then stripped with an acetone and methanol rinse. Finally, another plating base of 5 nm NiCr and 10 nm Au is evaporated onto the entire mask and PMMA spun-on and baked. The resultant segmented fiducial grating mask is now ready for SPLEBL.

In the second method the fiducial rectangles are defined simultaneously along with the gratings, thereby saving the post-holography etching steps described above. First, the entire x-ray mask is exposed holographically as described in the previous section. Then, prior to resist development a second optical UV exposure is performed to define the fiducial grating rectangles [48]. It is important to control the dose of the optical UV exposure such that the regions exposed by the UV develop out in the period of time it takes to develop the holographic exposure.

The remaining process steps are identical to those described in section 2.2 and shown in Figure 2-3. SiO_2 is shadow-evaporated and RIE of the ARC is performed. Gold electroplating is then used to pattern gold absorbers in the fiducial grating regions to a thickness of at least 200 nm, a thickness which provides an acceptable signal-to-noise ratio for data acquisition during SPLEBL. Finally, the SiO_2 etch mask is stripped in hydrofluoric acid and the resist and ARC are removed in an oxygen plasma. The resultant mask is ready for SPLEBL. Note that the required gold thickness of the fiducial grating is dictated by the imaging scheme used; that is, whether the detected signal primarily consists of secondary, backscattered or transmitted electrons. In our present approach we are imaging the backscattered electrons from the segmented fiducial grating x-ray mask. The number of backscattered electrons increases with the gold thickness. For our e-beam operating voltage of 50 kV, we find that a gold thickness of 200 nm provides a good signal-to-noise ratio. Another promising approach utilizes secondary electrons for imaging the fiducial reference [45]. In this approach a resist grating (or grid) can be patterned on top of a thin, conducting layer of a low atomic-number material (e.g. 10 nm of aluminum or titanium) which itself resides on top of the e-beam resist to be patterned. The signal contrast arises from the very large difference in secondary electron yield between the conducting material and the patterned resist. This approach also allows the full area of the substrate to be utilized for e-beam patterning since the e-beam writing process is not disturbed by the presence of the fiducial reference (as is the case for the segmented grating approach currently being used).

The third method involves making a 'grand-daughter' of the 'mother' mask made as described in section 2.2. That is, first a 'daughter' mask was made by an XRL exposure of the 'mother' mask into PMMA followed by gold electroplating. Next, a 'grand-daughter' mask was made by a second XRL exposure of this 'daughter' mask into PMMA followed by gold electroplating. The main advantage of this approach is that it saves a large amount of time in preparing masks for and performing holography as well as all of the post-holography processing, which would be necessary for each 'mother' mask. Using the three techniques described above, fiducial grating x-ray masks of period 230 nm and 513 nm were fabricated. The center-to-center spacing, height and length of the fiducial rectangles were 400 μm, 50 μm and 5 mm, respectively, for the 230 nm-period gratings and 50 μm, 10 μm and 4 mm, respectively, for the 511 nm-period gratings. Note that the area of fiducial grating provided is much larger than necessary; for the purpose of phase-locking a "window" only about 1-2 μm-square is sufficient.

Figure 2-14 shows a portion of a 230 nm-period fiducial grating mask along with a DFB grating defined using SPLEBL. The fiducial gratings are scanned in the alignment windows (four in each e-beam field) and a spatial phase is extracted from each of these four windows. The e-beam field is then adjusted in rotation, magnification and translation such that the spatial phases in each of the four windows is identical. This condition is the so-called *spatial-phase-locked* condition. After the field is 'locked', the e-beam grating is written. Then, to write the next grating segment, the stage is moved and the field is 'locked' again. In this way one can construct a long grating by

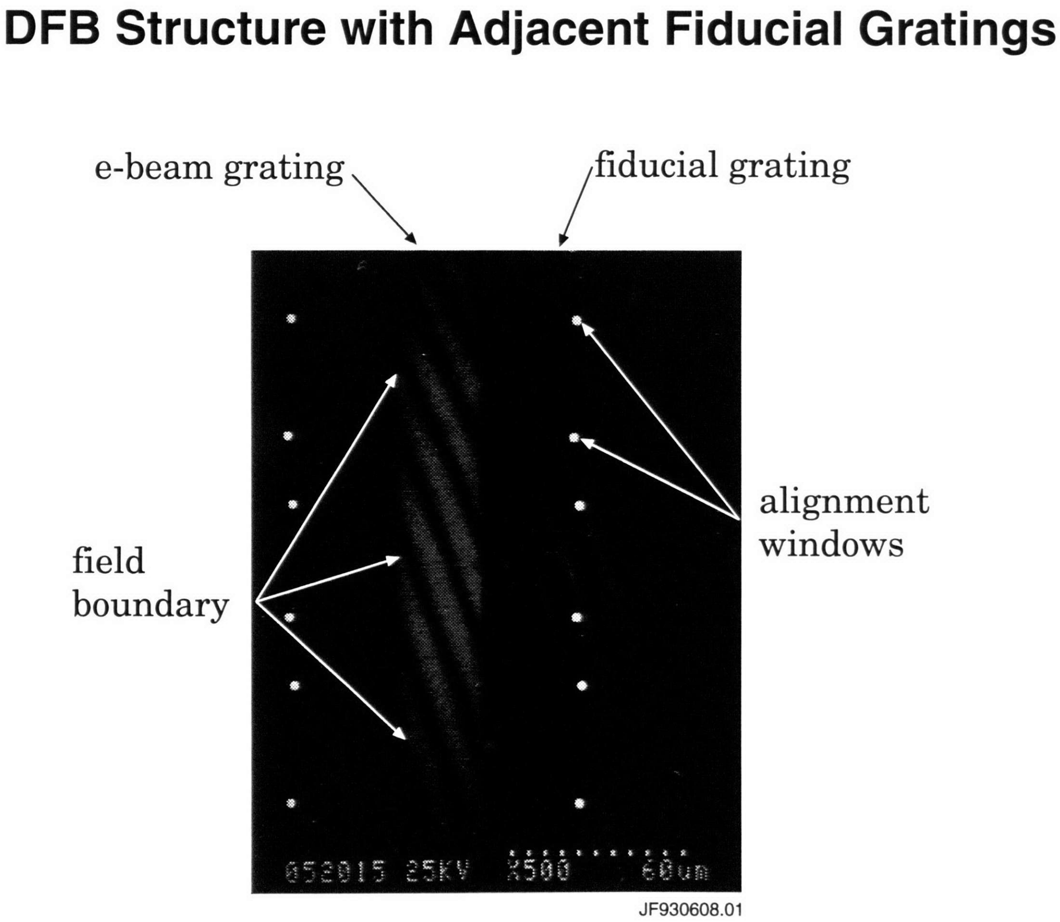

Figure 2-14: Scanning electron micrograph of a portion of a 230 nm-period fiducial grating mask patterned with a DFB grating using SPLEBL.

'stitching' together many smaller single-e-beam-field segments.

The tilted grating shown in Figure 2-14 is not the actual e-beam-written grating itself. Rather, it is a beat or moiré pattern formed by the beating between the e-beam grating and the raster scan of the scanning electron microscope. This moiré pattern is very sensitive to phase errors along the grating. The key point to note is that at each field boundary the moiré pattern is continuous, which indicates no significant phase errors, so-called 'stitching' errors, at the field boundaries.

Figure 2-15(*a*) shows a portion of a fiducial grating ($\Lambda = 513$ nm) x-ray mask containing e-beam-defined Bragg gratings. Figure 2-15(*b*) shows a $\lambda/4$-shift section of a Bragg grating. Using this mask, high-quality $\lambda/4$-shifted Bragg resonators were fabricated and tested. These are described in more detail in Chapter 4.

When defining the fiducial rectangles using any of the above three methods, it is important to minimize the angle, θ_d, between the $\vec{k}$-vector of the fiducial grating, $\vec{k}_h$, and the axis of the fiducial rectangle mask, $\hat{\mathrm{x}}_f$ (see inset in Figure 2-13). Doing so minimizes the angle between the $\vec{k}$-vector of the e-beam-defined Bragg grating and the axis of the rib waveguide on which these Bragg gratings will be pattern transferred.

A "flat" on the edge of the pyrex© frame of the x-ray mask was used as the angular alignment reference for both the holographic exposure and the UV exposure. Using this common reference, θ_d (which is subsequently measured in the EBL system) could be reduced to less than 0.1^o. Furthermore, it is important to ensure that both the substrate and e-beam system coordinate systems are scaled identically. In each approach four 'reference crosses', which are used to calibrate the two coordinate systems, at the edges of the device die were also defined in the same UV exposure which defined the fiducial rectangles .

It is important to note that the gratings in each of the fiducial rectangles of the 'mother', although segmented, are spatially-coherent to one another since they were defined from the same holographic exposure. It is this long range phase coherence that is utilized during SPLEBL. The upper part of Figure 2-13 depicts the fiducial

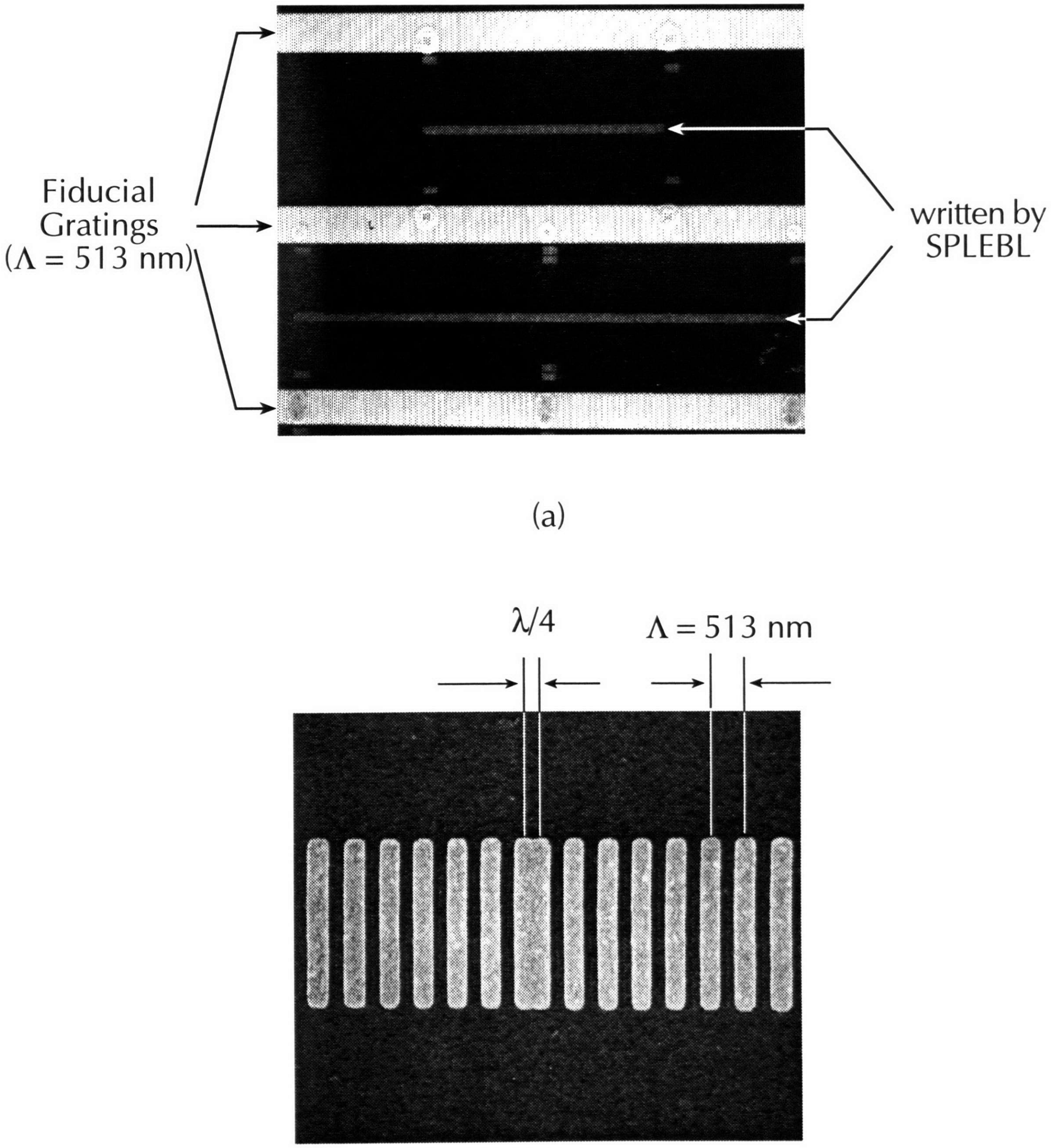

(a)

(b)

Figure 2-15: Scanning electron micrograph of a 513 nm-period fiducial grating mask: (*a*) Portion showing fiducial gratings and Bragg gratings written using SPLEBL and (*b*) $\lambda/4$-shift section of a Bragg grating.

gratings on the x-ray mask prior to e-beam patterning. The fiducial gratings span the length of the chip and are separated by no more than one EBL field so that two reference gratings can be viewed within one EBL field. The width of the fiducial rectangles is chosen such that a suitably large area remains for e-beam patterning and also to avoid any interaction between the optical mode and the fiducial gratings.

2.5 $\lambda/4$-Shifted Grating X-ray Masks

As described earlier, it is often desirable to pattern $\lambda/4$-shifted gratings. Typically, such gratings are patterned using EBL since holographic lithography is only practical for patterning uniform gratings. In this section we propose a technique that utilizes both holographic and XRL for obtaining $\lambda/4$-shifted grating patterns on an x-ray mask. The process is summarized in Figure 2-16 which shows the case for a grating containing two $\lambda/4$-shifts. First, an x-ray mask with a uniform grating is generated using holographic lithography and gold electroplating as described in section 2.2. Next, photoresist is spun-on and patterned. This pattern defines the grating region between the two $\lambda/4$-shifts, typically a few 10's to 100's of μm's. Next, a liftoff of an x-ray absorptive material is performed. This layer should be thick enough to provide $\sim$10 dB of attenuation and it should be possible to selectively remove this material without attacking the underlying gold grating pattern. Nickel is a good choice since it provides $\sim$44 dB attenuation per μm (at the Cu_L x-ray wavelength of 1.32 nm we are using) and can be selectively-removed in acid-based solutions which do not react with gold.

Next, plating base is evaporated on and PMMA spun-on the backside of the membrane. An x-ray exposure is performed through the mask (i.e. from front side through to back side) followed by gold electroplating, which transfers the grating pattern to the back side of the membrane. If desired, the front side of the mask can be 'protected' with a thin layer of resist while plating the back side. Note that

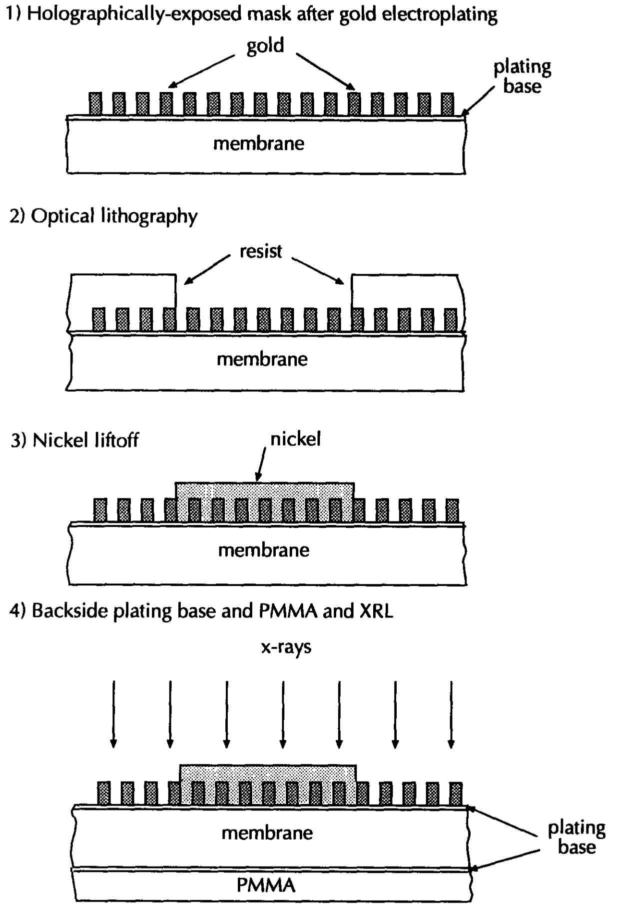

1) Holographically-exposed mask after gold electroplating

2) Optical lithography

3) Nickel liftoff

4) Backside plating base and PMMA and XRL

5) PMMA develop

6) Gold electroplating

7) Frontside gold and nickel strip

8) Daughter mask replication

Figure 2-16: Schematic of fabrication process for producing $\lambda/4$-shifted grating patterns on an x-ray mask. In this example two $\lambda/4$-shifts are shown. However, the process can be adapted to any number of $\lambda/4$-shifts.

the regions underneath the nickel layer will not develop out and therefore will not plate. Also, the gratings that do get transferred to the back side of the membrane are 180^o out-of-phase with those on the front side of the membrane as a consequence of the polarity reversal. It is these 180^o phase-shifts that provide the $\lambda/4$-shifts. The remaining steps are to remove the PMMA and resist from the back and front sides of the membrane, respectively. Then another resist layer is spun-on the back side of the membrane and the exposed gold gratings on the front side are selectively-removed in a wet chemical etch. Then, the nickel layer is selectively removed from the front side of the membrane and the resist stripped from the back side. At this point, a 'daughter' exposure can be performed using this mask followed by development and gold electroplating. The resultant mask will contain a gold grating with two $\lambda/4$-shifts, as shown in Figure 2-16.

Because of the possibilities of non-vertical sidewalls after the nickel liftoff (step 3 in Figure 2-16) and lateral etching during the removal of the gold and nickel (step 7 in Figure 2-16) the $\lambda/4$-shifts may not be as abrupt as those defined using EBL. However, for devices such as DFB lasers, good operation can be obtained as long as the grating sections are 'globally' shifted by a $\lambda/4$ [49–53]. With proper design of the optical mask this technique also allows grating patterns containing an arbitrary number of $\lambda/4$-shifts to be included on the same x-ray mask. Because of the increased process complexity compared to the e-beam patterning of an x-ray mask, this process was never implemented. In particular, it is difficult to obtain a uniform resist film on the back side of the x-ray mask as well as make electrical contact to the back side of the x-ray mask for gold electroplating. Recently, however, a similar approach has been used to obtain high-aspect ratio patterns for phase shift fresnel zone plates [54].

Chapter 3

Distributed Feedback Lasers

In the previous chapter the techniques for fabricating phase-coherent periodic structures were described. Such periodic structures find widespread use in applications ranging from spectroscopy, to pulse compression, to optical information processing. In these applications use is made of the dispersive or frequency-selective property of the periodic structure. In this chapter we consider another application of such frequency-selective grating structures, in particular, for so-called distributed feedback (DFB) lasers. A brief introduction to the phenomenon of distributed feedback and its application to lasers is given. The concept of lateral coupling is then introduced and the results of computer simulations are presented which show the feasibility of the concept for DFB lasers. Finally, the techniques which have been developed for fabricating the requisite grating patterns are described and the experimental results discussed.

3.1 Background

A simplified view of a laser is an oscillator with gain. Therefore, in order to construct a laser, one must have both optical gain and optical feedback. For semiconductor lasers the optical gain is typically achieved by tailoring the epitaxial layers (in combination with either optical excitation with a 'pump' source or electrical excitation with a current drive). In particular, by adjusting the bandgaps (and, therefore, the indices of refraction) of the epitaxial layers, electron/hole (as well as optical) confinement can be achieved. Such confinement facilitates the stimulated recombination processes which result in lasing. Several technologies can be used for the epitaxial growth of laser substrates: liquid-phase epitaxy (LPE), metal-organic chemical vapor deposition (MOCVD), metal-organic vapor-phase epitaxy (MOVPE), molecular-beam epitaxy (MBE) and chemical-beam epitaxy (CBE). The maturation of these technologies has been instrumental to the vast improvements of semiconductor laser diodes in the recent past. In this work, however, we focus more on the feedback mechanism which is necessary for laser action.

Laser oscillation occurs when the gains of the system are greater than the losses. Traditionally, the necessary feedback has been provided by reflections from cleaved end-faces. Such resonators are the well-known Fabry-Perot type, and have many equivalent longitudinal resonances equally-spaced over the gain bandwidth. Since the profile of gain versus wavelength of semiconductors is generally broad, many longitudinal modes satisfy the lasing threshold condition. Such a situation results in the laser operating simultaneously in several longitudinal modes, which is undesirable for fiber optic communications. To operate such Fabry-Perot lasers in a single longitudinal mode, external cavity mirrors and gratings, cleaved-coupled cavity structures, injection-locking and ultra-short microcavities have been used [55].

An alternate method, first proposed by Kogelnik and Shank [56], incorporates a spatial modulation of the refractive index (index-coupling) and/or the gain/loss (gain-coupling) over the entire length of the resonator. For example, Figure 3-1 shows a case for index-coupling, which is typically achieved by patterning periodic surface corrugations in the laser media (with index n_{sub}), as described in Section 3.3. The consequence of the spatial modulation is that it provides a frequency-selective mechanism for feedback through the phenomenon of Bragg reflection which occurs *along*

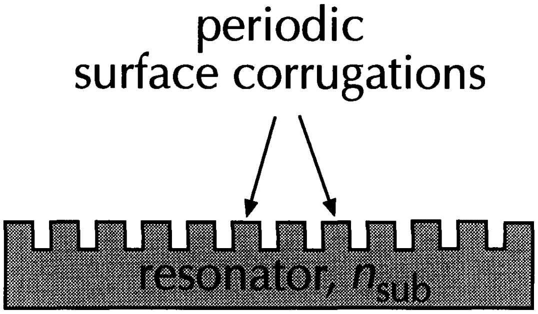

Figure 3-1: Schematic of resonator where the optical feedback is achieved through index-coupling.

the length (hence the term '*distributed* feedback') of the resonator. This mechanism, in turn, provides sufficient longitudinal mode discrimination for single-longitudinal mode operation. Physically, the Bragg reflection occurs due to an interference between the forward and backward traveling waves which forms a standing wave within the waveguide structure. This interaction, provided by the periodic structure, is described formally by the coupled-mode equations (CME).

Consider a medium with refractive index, n, and gain, α. We are ultimately interested in the coupling between forward and backward-running waves. Therefore, denote the wave with positive group velocity, the "forward" wave, in the guiding structure by a, and the wave with negative group velocity, the "backward" wave, by b. In a uniform waveguide, the differential equations obeyed by a and b are [57]

$$\frac{da}{dz} = (\alpha - j\beta)a \tag{3.1}$$

$$\frac{db}{dz} = (-\alpha + j\beta)b \tag{3.2}$$

These are two independent differential equations. Suppose, however, that a periodic perturbation is introduced in the refractive index

$$n(z) = n + n_1 \cos 2\beta_o z. \tag{3.3}$$

The effect of coupling of a to b can be included in (3.1) and (3.2) by introducing a coupling term, κ, produced by the scattered radiation

$$\frac{da}{dz} = (\alpha - j\beta)a + \kappa_{ab} b \exp -2j\beta_o z \tag{3.4}$$

$$\frac{db}{dz} = (-\alpha + j\beta)b + \kappa_{ba} a \exp +2j\beta_o z. \tag{3.5}$$

Introducing the new variables $a = A(z)\exp -j\beta_o z$ and $b = B(z)\exp j\beta_o z$ we obtain the CME for waves due to a periodic perturbation in refractive index:

$$\frac{dA}{dz} = (\alpha - j(\beta - \beta_o))A + \kappa_{ab}B = (\alpha - j\delta)A + \kappa_{ab}B \tag{3.6}$$

$$\frac{dB}{dz} = (-\alpha + j(\beta - \beta_o))B + \kappa_{ba}A = (-\alpha + j\delta)B + \kappa_{ba}A \tag{3.7}$$

where δ is defined as $\frac{(\omega-\omega_o)}{v_g}$ and describes the deviation of the mode from the Bragg frequency.

In the above equations the coupling terms, κ_{ab} and κ_{ba}, are given by [58]

$$\kappa_{ab} = \frac{k_o^2}{2\beta}\frac{\int_{-\infty}^{+\infty}\int_{-\infty}^{+\infty} \phi_a(x,y)A_m(x,y)\phi_b(x,y)\,dx\,dy}{\int_{-\infty}^{+\infty}\int_{-\infty}^{+\infty} \phi_a(x,y)\phi_b(x,y)\,dx\,dy} \tag{3.8}$$

$$\kappa_{ba} = \frac{k_o^2}{2\beta}\frac{\int_{-\infty}^{+\infty}\int_{-\infty}^{+\infty} \phi_b(x,y)A_{-m}(x,y)\phi_a(x,y)\,dx\,dy}{\int_{-\infty}^{+\infty}\int_{-\infty}^{+\infty} \phi_b(x,y)\phi_a(x,y)\,dx\,dy} \tag{3.9}$$

where k_o is the free-space wavelength, β is the propagation constant, ϕ_a and ϕ_b are the fields of the unperturbed waveguide and A_m and A_{-m} are the appropriate coefficients in the Fourier expansion of the index modulation for which the Bragg condition (i.e. $\beta \approx \beta_0$) is satisfied. That is, for a grating of order m the appropriate have $\kappa_{ab} = \kappa^*_{ba}$, which yields a purely real coupling coefficient. If, on the other hand, the modulation were in the gain profile, then $A_m(x) = -A^*_{-m}(x)$. From this it follows that $\kappa_{ab} = -\kappa^*_{ba}$ and the coupling coefficient is purely imaginary.

We consider the two limiting cases where (*i*) κ is purely real and (*ii*) κ is purely imaginary. The former case is often referred to as index-coupling and the latter case gain-coupling. We also assume a symmetric grating structure as well as perfect AR-coated facets.

As shown in Kogelnik and Shank's classic paper [56], for index-coupling the mode spectrum is symmetric with respect to the Bragg frequency ($\delta = 0$) and a 'forbidden gap' appears in the dispersion relation centered about $\delta = 0$. In particular, frequencies which lie within this gap are attenuated (i.e. evanescent waves) and no resonance occurs at the Bragg frequency. The bandgap in the dispersion diagram effectively acts as a reflection filter. The center frequency of the filter is at $\delta = 0$ (e.g. no detuning), or $\omega = \omega_o$, and the stopband width is $2 \mid \kappa \mid$.

At these resonant frequencies, standing-waves are formed. However, they have superimposed on them a beat wavelength which arises from the interference between the closely-related periodicity of the standing waves and the corrugations. As a result of this effect, any particular length of corrugated waveguide exhibits a natural resonance at the optical frequency that creates a beat wavelength to match the total length of the perturbed section, or some submultiple of that length.

Figure 3-2 plots the reflection spectrum of a typical index-coupled DFB structure as a function of normalized frequency, δ/κ. The resonances of the DFB laser are symmetrically placed outside of the stopband (indicated in the figure) and will occur at values of δ/κ where the reflectivity is zero. The finesse of the 'resonances' decreases as the detuning increases. For this reason the threshold gain increases as the detuning away from the Bragg frequency increases. In this way the periodic structure results in improved mode discrimination. However, a consequence of a symmetric mode spectrum is that a mode degeneracy exists for the index-coupled DFB laser which is

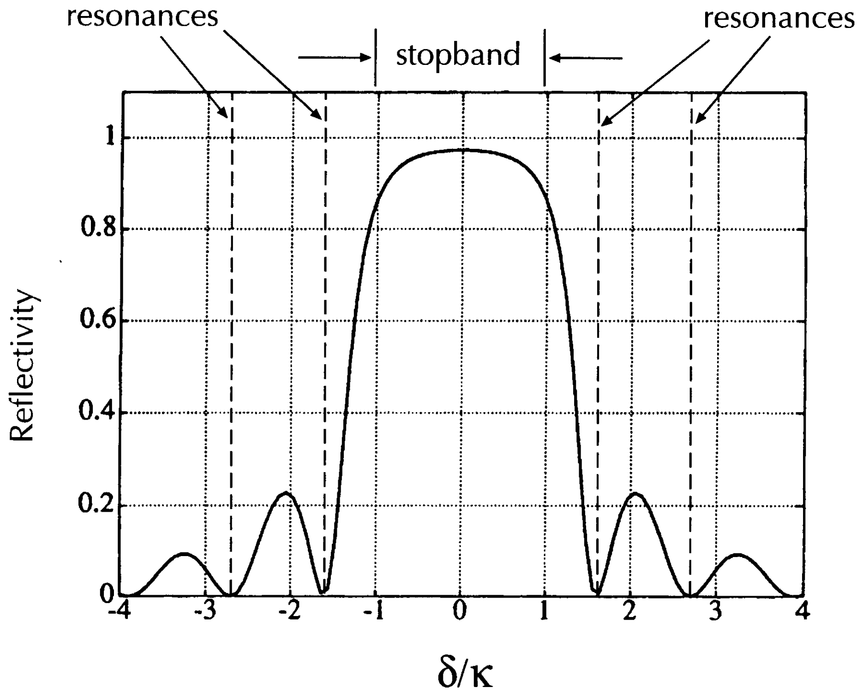

Figure 3-2: Reflectivity as a function of normalized frequency, δ/κ, for a typical index-coupled DFB structure.

incompatible with single-longitudinal mode operation.

Several methods have been proposed to remove this degeneracy: (*i*) inclusion of a quarter-wave-shift (QWS) in the DFB grating [59]; (*ii*) introduction of a linear chirp in the DFB grating [60]; (*iii*) modulation of the stripe width [61–63]; (*iv*) introduction of a tuning section [64]; (*v*) tailoring the magnitude of the end cavity reflectors [65,66] and (*vi*) promoting radiation loss in a second-order grating [67–69]. Of all the proposed methods, the asymmetric facet reflectivity configuration and the incorporation of the quarter-wave-shift are the most popular.

3.1.2 Gain coupling

For perfect gain-coupling, we find that no degeneracy exists in the mode spectrum [56]. The resonant frequency with the lowest threshold gain lies exactly at the Bragg frequency and the higher-order modes of the DFB laser lie symmetrically about the Bragg frequency. Again, as for the index-coupled case, the threshold gain increases with increasing deviation from the Bragg frequency. This is unlike the case in Fabry-Perot lasers where the threshold gain is identical for each longitudinal mode of the cavity. In this way the DFB laser provides superior mode discrimination than conventional cleaved-cavity lasers, making it highly desirable for fiber optic communication applications.

In practice, index-coupling is much easier to realize than gain-coupling. Typically, index-coupling is achieved by forming a periodic surface-relief profile by lithographic and etching techniques onto a laser substrate. Such a surface-relief profile induces a periodic modulation of the effective index. Gain-coupled DFB lasers, being much harder to fabricate, have only recently been demonstrated. Gain-coupling has typically been achieved by forming a grating on an absorptive layer attached to the active layer [70] or by forming a grating directly on the active layer [71]. Physically, the gain modulation is achieved by modulating the optical confinement factor. Note that gain-coupling can be achieved by a modulation of either the gain or the loss. In either case, however, this gain/loss grating should be located very near the optical mode for maximum coupling. To achieve this condition, the epitaxial growth of the laser structure must be interrupted to pattern the grating. After the grating fabrication, the epitaxial growth is resumed. This process of interrupted growth is often referred to as epitaxial overgrowth.

Gain-coupled DFB lasers, although much harder to fabricate, offer several advantages over index-coupled DFB lasers. Some of these advantages are a decreased sensitivity to facet reflections [72], reduced spatial hole burning [73], improved FM response as well as improved mode discrimination all of which result in higher single-mode yields (i.e. the percentage of fabricated devices which operate in a single longitudinal mode under certain operating conditions). Experimental single-mode yields as high as 95% have been demonstrated [3]. This value is compared with yields typically below 50% for index-coupled DFB lasers [74]. It has been shown that even a small degree of gain coupling results in improved device performance [73,75,76]. Therefore, if possible DFB lasers should be designed with some degree of gain-coupling at minimal expense to their fabrication complexity.

Recently, it has been shown that second-order index-coupled DFB lasers are physically as well as mathematically equivalent to partly gain-coupled DFB lasers [74]. The additional gain-coupling, which is introduced by the second-order grating, as mentioned above should result in improved device performance.

A second-order grating provides reflection by means of second-order diffraction and also exhibits 90^o radiation by first-order diffraction. This radiation is a superposition of contributions from the two oppositely traveling waves which form the resonator mode. As in the case for a first-order grating, a gap or stopband appears in the dispersion relation. However, the phase relationship of the two contributions to the 90^o first-order diffraction is such that at one edge of the gap the two contributions are out-of-phase and at the other edge the two contributions are in-phase. This is shown schematically in Figure 3-3. Consequently, the favored mode (i.e. with the lower

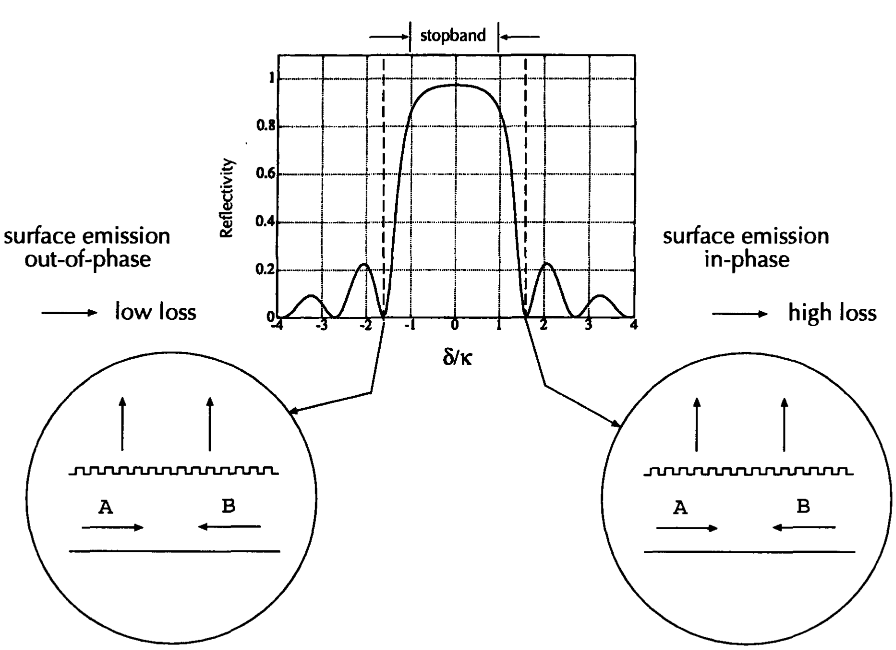

Figure 3-3: Schematic showing physical principle of mode discrimination in second-order index-coupled DFB lasers.

threshold gain) occurs at the edge where the radiation cancels (i.e. lower loss). In this way a second-order grating breaks the degeneracy and improves single-longitudinal mode operation [68].

Physically, one can think of the excitation of the radiation modes in a second-order grating as equivalent to losses that can also be described by a periodically-varying loss coefficient [67]. Mathematically, it has been shown that DFB lasers utilizing higher-order Bragg reflection have a complex coupling coefficient [67]. As such, one can think of the imaginary component to the coupling coefficient effectively as a gain-coupling term although there is *no physical variation in gain/loss* within the device. The two contradirectional guided waves combining to produce the radiating waves cause an overall gain/loss coupling in addition to the periodic index variation.

Streifer *et al.* [67] modified the coupled-mode equations (3.6) and (3.7) to include the effects of radiation and showed that the higher-order Bragg diffraction results in an asymmetric longitudinal mode structure about the Bragg frequency. In addition, unlike the case in first-order DFB lasers where two modes have the same gain threshold (i.e. a degeneracy), the mode with the lowest gain threshold is non-degenerate in DFB lasers based on higher-order Bragg diffraction. Kazarinov and Henry [68] analyzed 1.5 μm second-order DFB lasers and showed that a selectivity provided by radiation loss against the competing mode of order 10 cm^{-1} could be obtained. Baets *et al.* [74] determined that a value of κ_{gain} of 1.25 cm^{-1} for second-order gratings should be sufficient to ensure stable single mode behavior.

In the next section we describe a new type of DFB laser structure, a laterally-coupled DFB structure, and show through computer simulations that both 1st- and 2nd-order lasers based on this structure compare favorably with more conventional DFB laser structures. We also investigate the possibility of implementing the lateral coupling concept on a recently-proposed reverse-mesa ridge-waveguide laser [77] which has demonstrated improved performance over conventional vertical-mesa ridge-waveguide lasers.

3.2 Laterally-Coupled DFB Lasers: Simulations

Typically, in the fabrication of an index-coupled DFB laser the formation of the grating interrupts the epitaxial growth of the layer structure, thereby requiring an overgrowth step. Figure 3-4 is a schematic of an index-coupled DFB laser structure fabricated by such a process. As shown, the DFB grating is buried within the layer structure, which was overgrown after the grating fabrication. Epitaxial overgrowth results in increased process complexity and consequently decreased device yield. Recently, Miller *et al.* [78] proposed a laser structure in which lateral gratings, patterned with EBL, are reactive-ion-etched into the top cladding layer of the laser on either side of the contact stripe. The gratings serve to provide both optical feedback and lateral optical confinement, which are dependent on grating depth. This process,

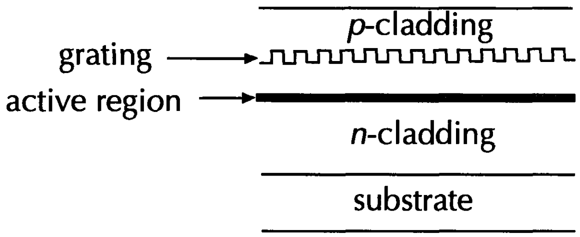

Figure 3-4: Schematic showing the layer structure of a 'conventional' DFB laser. As shown, the DFB grating is buried within the layer structure. The fabrication of such a buried grating requires an overgrowth step, which results in increased process complexity and decreased device yield.

while requiring only one epitaxial growth step, is complicated by the fact that extremely deep (0.7 μm-1.0 μm) gratings are required. Korn *et al.* [79] fabricated a DFB laser structure in which the grating is patterned on top of the ridge by EBL followed by RIE and lasing action was obtained by optical pumping (as opposed to current injection).

Figure 3-5 is a schematic of a laterally-coupled (LC) DFB laser. As shown, the grating is patterned in the channels on either side of the ridge, or 'lateral' to the ridge. In this way the lateral gratings can be patterned after the completion of both the epitaxial growth of the laser material and the formation of a ridge-waveguide, and the grating fabrication can be decoupled from the epitaxy step. Furthermore, the degree of lateral confinement as well as the grating coupling coefficient can be independently adjusted by varying the ridge height and grating depth, respectively. Feedback occurs due to the interaction of the lateral evanescent fields and the index modulation introduced by the grating. Since the mode profile falls off rapidly with distance, it is desirable to pattern the grating as close to the sidewall as possible. Gratings are not patterned on top of the ridge to allow for a metal contact for current injection. Recently, Martin *et al.* [80] and Tiberio *et al.* [81] fabricated LC-DFB lasers in InGaAs-GaAs-AlGaAs by EBL.

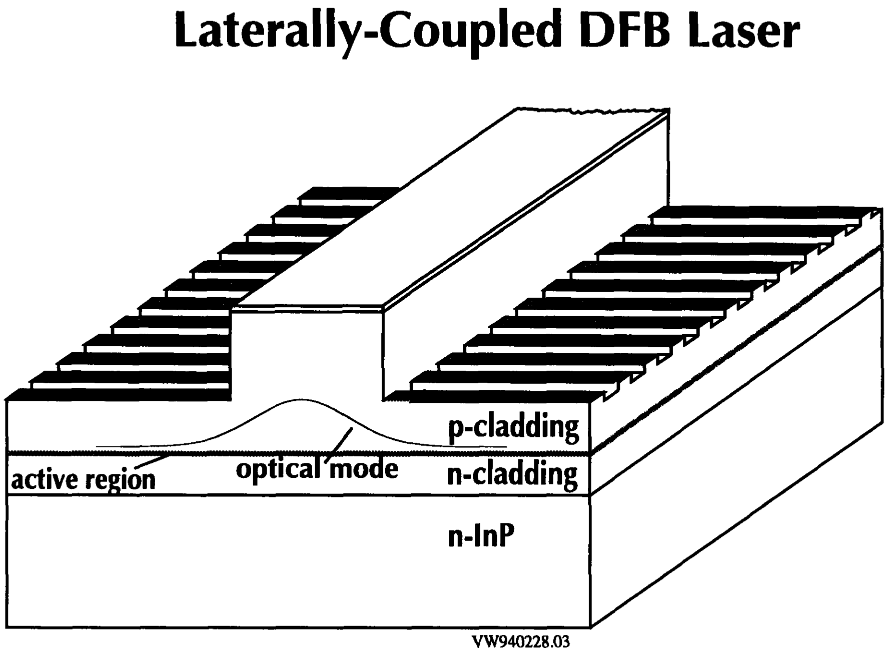

Figure 3-5: Schematic of a laterally-coupled distributed feedback laser.

3.2.1 Vertical-Mesa RWG LC-DFB

Computer simulations of LC-DFB structures have been performed to calculate the coupling coefficient, κ, as a function of various waveguide and grating parameters. In particular, the results show that for 1st- and 2nd-order LC-DFB lasers, κ-values up to ~50 cm^{-1}, which are comparable to those reported in the literature [82–84], can be obtained. The optimum κ-value for a particular device is dependent on the desired device behavior. One of the most common designs calls for a QWS grating with a κL-product of ~1.25, which serves to minimize the effects of spatial-hole burning [85]. If reduced sensitivity to facet reflections is desired, higher κL-products can be used (at the expense of increased spatial-hole-burning) [1]. For more complicated multiple-phase-shifted DFB lasers, the κL-value is determined based on considerations such as linewidth narrowing [86,87] and also the reduction of spatial-hole-burning [19,88].

Figure 3-6 shows the various parameters which were investigated. These param-

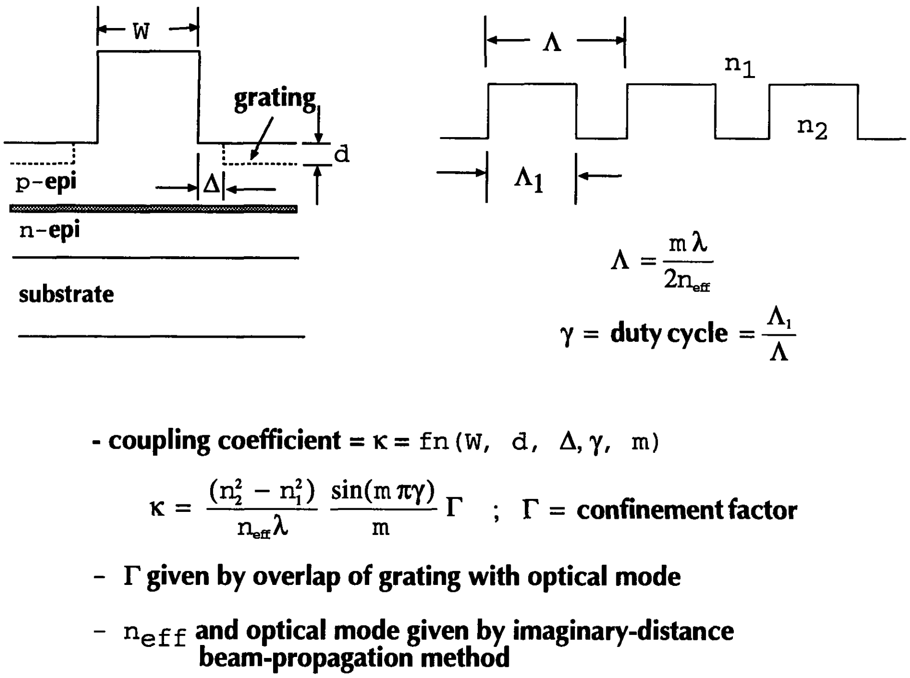

Figure 3-6: Schematic showing the various waveguide and grating parameters investigated in the κ-simulations.

eters are the ridge width, W, the grating depth, d, the grating duty cycle, γ, the grating order, m, and the distance between the lateral grating and the ridge sidewall, Δ. For 1st-order LC-DFB structures a lasing wavelength, λ, of 1.55 μm is assumed, whereas for 2nd-order LC-DFB structures $\lambda = 1.3$ μm is assumed. These choices are based on the available materials which we obtained from Lasertron, Inc., a commercial semiconductor-laser vendor we are collaborating with. The grating region is modeled as a single homogeneous layer whose index, n_g is given by [89]

$$n_g^2 = \frac{\Lambda - \Lambda_1}{\Lambda} n_1^2 + \frac{\Lambda_1}{\Lambda} n_2^2. \tag{3.14}$$

Recall that the coupling coefficient, κ, is given by either Eqn. (3.8) or Eqn. (3.9) ($\kappa_{ab} = \kappa_{ba}$ for index-coupling). For rectangular-shaped gratings, these equations can be simplified to [58]

$$\kappa = \frac{(n_2^2 - n_1^2)}{n_{eff}\lambda} \frac{\sin m\pi\gamma}{m} \Gamma \tag{3.15}$$

where n_2 and n_1 are the indices of the grating and surrounding medium, respectively, n_{eff} is the effective index of the optical mode and Γ is the confinement factor, which is given by the overlap of the optical mode with the grating. The imaginary distance beam propagation method [90] (IDBPM) was used to calculate the fundamental optical mode of the ridge-waveguide as well as the effective index of the mode (for a given waveguide geometry). Figure 3-7 shows the laser layer structure used for the simulations of the 1st-order LC-DFB structures. It consists of n- and p-InP cladding layers, a highly-doped InGaAs cap layer for ohmic contact, graded-index separate-confinement heterostructures (GRINSCHs) and strained InGaAlAs-based quantum wells. It also contains an InGaAsP etch stop layer which serves to constrain the ridge height at 1.115 μm. Note that the simulation results presented below, although specific to the layer structure shown in Figure 3-7, illustrate the general dependencies of the coupling coefficient on the various waveguide and grating parameters considered.

An $\mathrm{In}_{1-x-y}\mathrm{Ga}_y\mathrm{Al}_x\mathrm{As}/\mathrm{InP}$ materials system is utilized instead of the more conventional $\mathrm{In}_{1-x}\mathrm{Ga}_x\mathrm{P}_{1-y}\mathrm{As}_y/\mathrm{InP}$ material system. This decision is based on the stronger electron confinement of InGaAlAs-based quantum wells, because of their larger conduction band offset, as opposed to InGaAsP-based quantum wells. The stronger electron confinement allows lasers to be operated at higher output powers as well as operate uncooled [91,92].

Figure 3-8 shows the dependence of κ on the grating etch depth of a 70% duty cycle 1st-order grating for ridge widths of 2.0, 3.0 and 4.0 μm and a Δ-value of 0 (i.e. the lateral gratings run right up to the ridge sidewall). Clearly, κ is higher for a narrower ridge. Qualitatively, this is because the narrower ridge guides the lateral mode more weakly. Consequently, more of the mode resides within the region of the grating, resulting in a larger field overlap.

Figure 3-9 shows the dependence of κ on the grating etch depth of a 50% duty

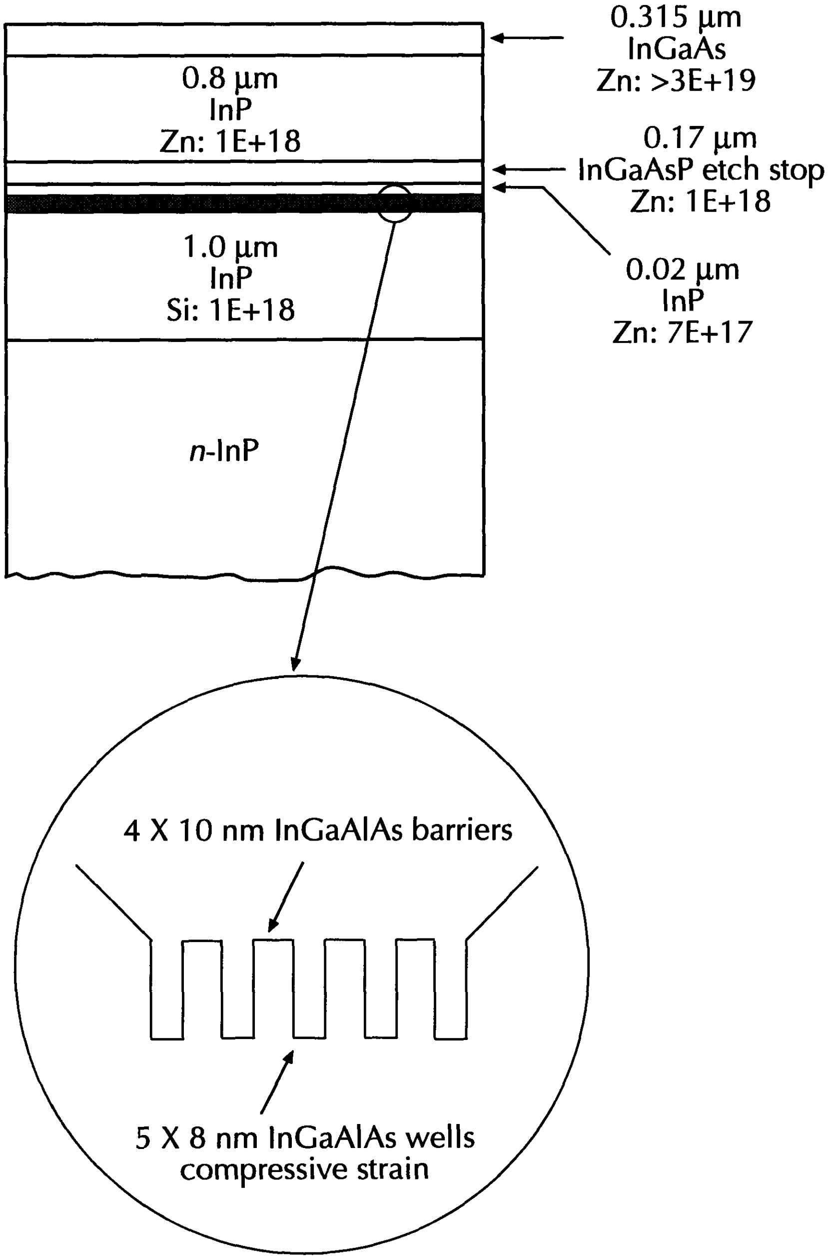

Figure 3-7: Diagram of laser layer structure used for κ-simulations for 1st-order LC-DFB structures.

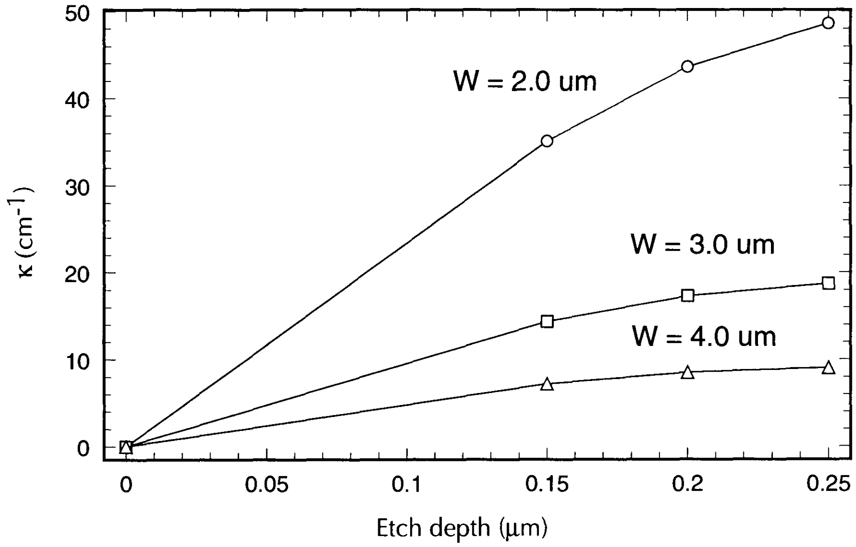

Figure 3-8: κ vs. grating etch depth for a 70% duty cycle 1st-order grating, ridge widths of 2.0, 2.5 and 3.0 μm and a Δ-value of 0.

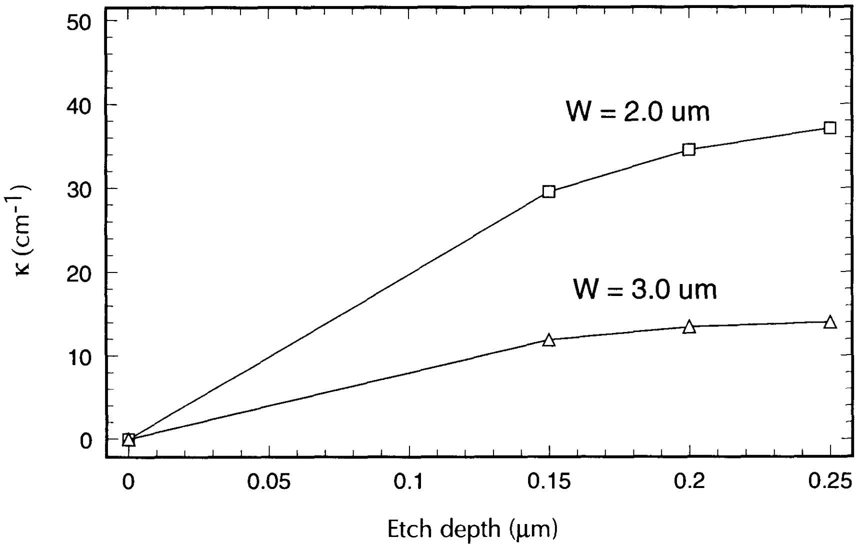

Figure 3-9: κ vs. grating etch depth for a 50% duty cycle 1st-order grating, ridge widths of 2.0 and 3.0 μm and a Δ-value of 0.

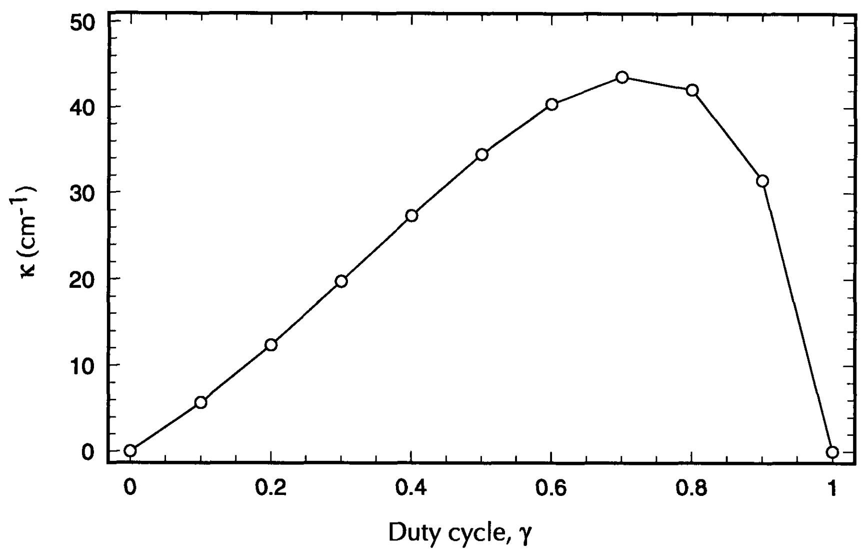

Figure 3-10: κ vs. duty cycle, γ, for a 1st-order grating, a ridge width of 2.0 μm, a grating etch depth of 0.2 μm and a Δ-value of 0.

cycle 1st-order grating for ridge widths of 2.0 and 3.0 μm and a Δ-value of 0. Clearly, the achievable κ's are lower than for a 70% duty cycle grating. Figure 3-10 shows the dependence of κ on the duty cycle of a 1st-order grating, a ridge width of 2.0 μm, an etch depth of 0.2 μm and a Δ-value of 0. The maximum κ occurs at a duty cycle of ~70%, although κ is fairly insensitive to changes in the duty cycle between 65% and 80%. The asymmetry (about the 50% duty cycle point) in the figure is due to the increasing contribution of Γ to κ (see Eqn. (3.15)) for increasing duty cycles. As the duty cycle increases, the effective index of the grating region also increases. The optical mode, 'seeing' a higher index, spreads further out laterally, thereby increasing Γ. Eventually, κ decreases again due to the $\frac{\sin m\pi\gamma}{m}$-term.

Figure 3-11 shows the dependence of κ on Δ, the distance between the lateral grating and the ridge sidewall for a ridge width of 2.0 μm, a grating etch depth of 0.2 μm and 1st-order grating duty cycles of 50%, 60% and 70%. As expected, the coupling decreases as the lateral gratings move away from the sidewall due to the decreased confinement factor. Clearly, it is desirable to pattern the lateral gratings

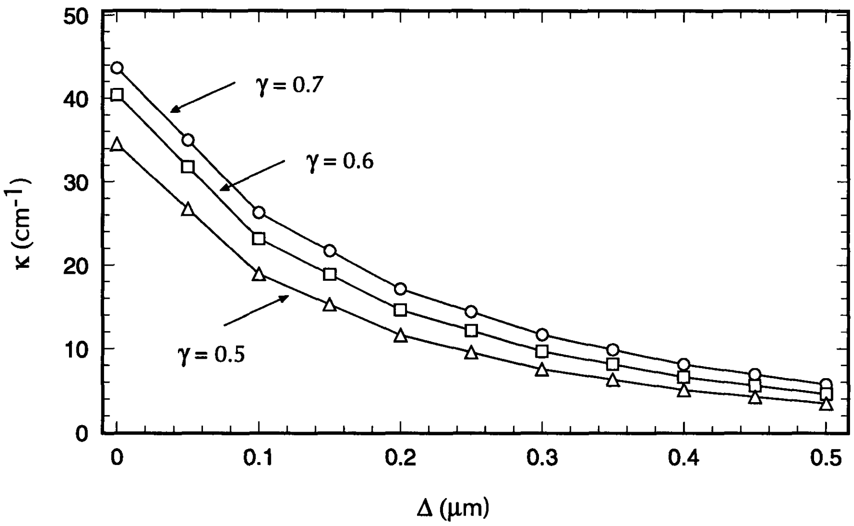

Figure 3-11: κ vs. Δ for a 1st-order grating of duty cycles 50%, 60% and 70%, a ridge width of 2.0 μm and a grating etch depth of 0.2 μm.

as close to the ridge sidewall as possible. Figure 3-12 schematically illustrates this fact. In particular, the lateral gratings should be within 0.1 μm of the ridge sidewall to obtain a reasonable degree of coupling.

The simulation results for 2nd-order gratings show similar trends to those presented above for 1st-order gratings. The achievable κ values, however, are lower than those for 1st-order gratings. Mathematically, this is because of the $\frac{1}{m}$-dependence in the $\frac{\sin m\pi\gamma}{m}$-term. Physically, this is because the grating now couples not only the forward/backward propagating waves to backward/forward propagating waves, but also to radiated waves. This additional coupling mechanism, however, as explained in section 3.1 can result in improved mode discrimination, and it is for this reason that there has been growing interest in 2nd-order index-coupled DFB lasers. For 2nd-order LC-DFB structures, we modeled the layer structure in Figure 3-13, whose target wavelength is in the 1.3 μm-region. As noted previously, the simulation results presented below, although specific to the layer structure shown in Figure 3-13, illustrate the general dependencies of the coupling coefficient on the various waveguide

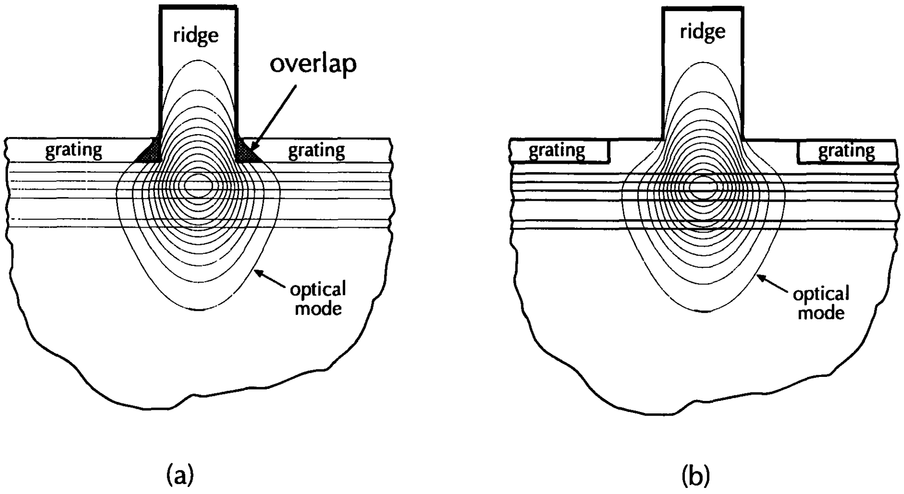

Figure 3-12: Dependence of overlap of optical mode with lateral grating on coupling: (*a*) Large overlap results in good coupling and (*b*) Small overlap results in poor coupling.

and grating parameters considered.

Figure 3-14 shows the dependence of κ on the grating etch depth of a 70% duty cycle 2nd-order grating, ridge widths of 2.0, 2.5 and 3.0 μm and a Δ-value of 0.

Figure 3-15 shows the dependence of κ on the duty cycle, γ, of a 2nd-order grating for a ridge width of 2.0 μm, a grating etch depth of 0.2 μm and a Δ-value of 0. As in Figure 3-10, the asymmetry is due to the increase of the confinement factor for increasing duty cycles. The maximum κ occurs at a duty cycle of ~80%, although κ is fairly insensitive to changes in the duty cycle between 80% and 90%.

Figure 3-16 shows the dependence of κ on Δ for a 2nd-order grating of duty cycles 70%, 80% and 90%, a ridge width of 2.0 μm and a grating etch depth of 0.2 μm. Once again, the results indicate that gratings should be within 0.1 μm of the ridge sidewall to obtain a reasonable degree of coupling.

The results of the above simulations can be summarized as follows. The guide widths should be no wider than 2 μm. Guides wider than 2 μm guide the optical mode more tightly which decreases the mode overlap with the lateral grating. Etch depths should range between 0.1 and 0.2 μm, and the lateral gratings should reside

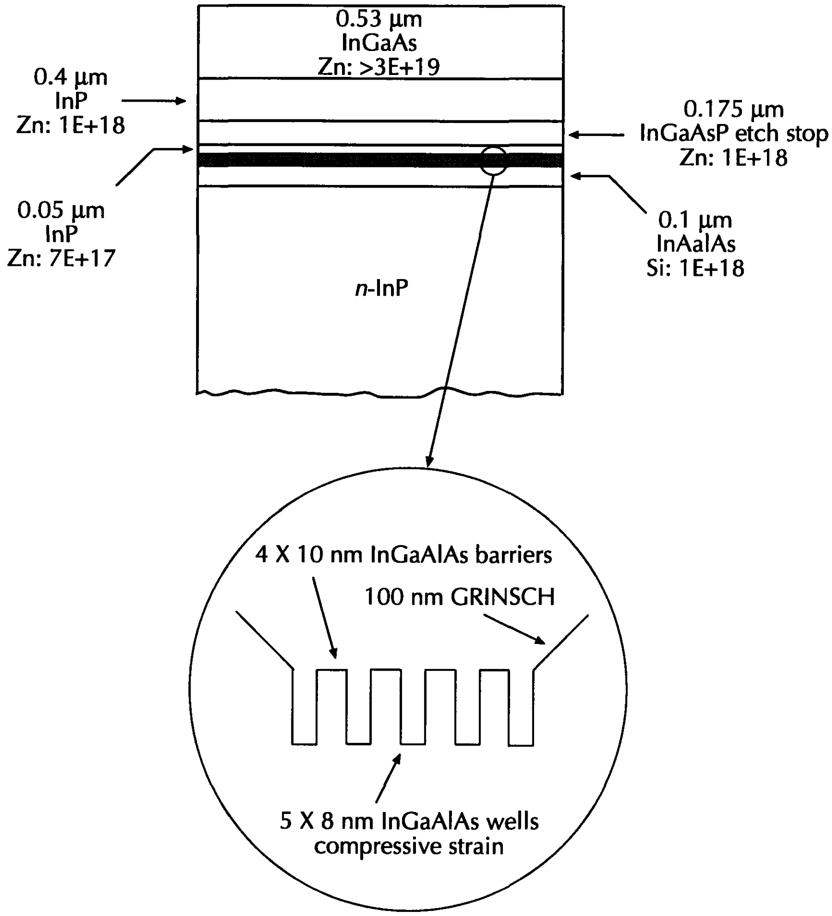

Figure 3-13: Diagram of laser layer structure used for κ-simulations of 2nd-order LC-DFB structures.

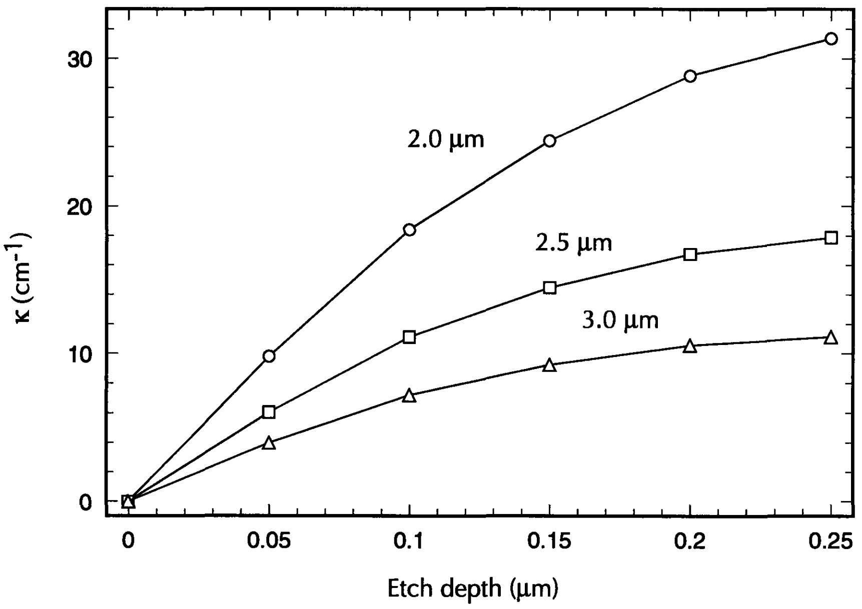

Figure 3-14: κ vs. grating etch depth for a 70% duty cycle 2nd-order grating, ridge widths of 2.0, 2.5 and 3.0 μm and a Δ-value of 0.

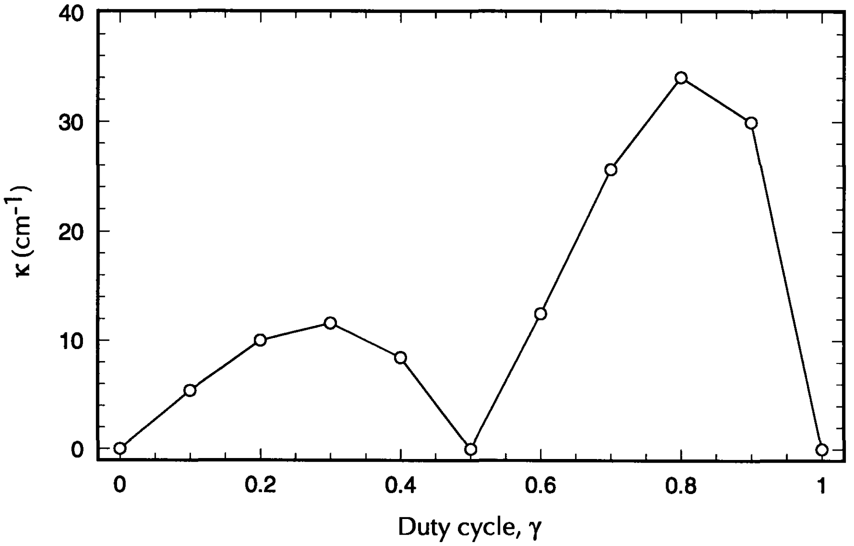

Figure 3-15: κ vs. duty cycle, γ, of a 2nd-order grating for a ridge width of 2.0 μm, a grating etch depth of 0.2 μm and a Δ-value of 0.

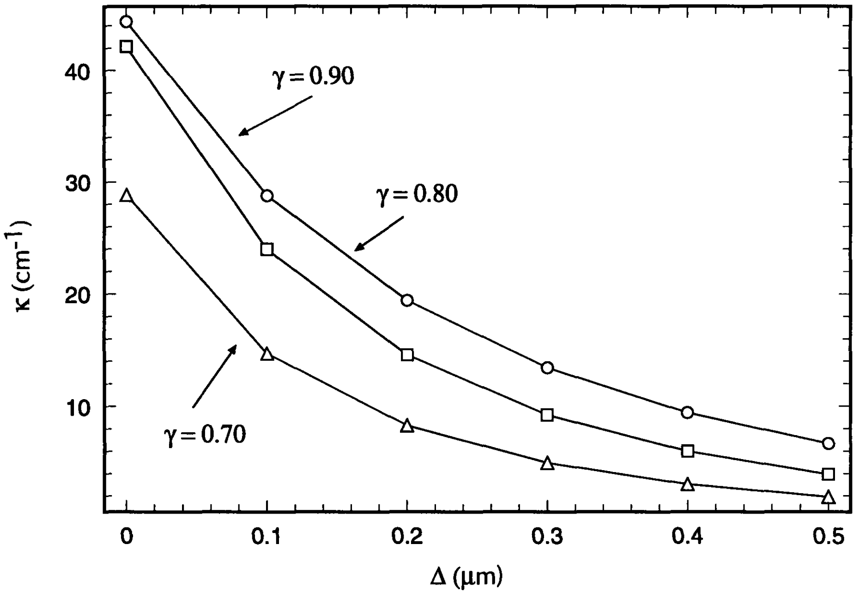

Figure 3-16: κ vs. Δ for a 2nd-order grating of duty cycles 70%, 80% and 90%, a ridge width of 2.0 μm and a grating etch depth of 0.2 μm.

within 0.1 μm of the ridge sidewall. Furthermore, the grating duty cycles for 1st- and 2nd-order gratings should be targeted around 70% and 80%, respectively, resulting in sub-100 nm feature sizes for typical grating periods. Finally, the effective index, as determined by the IDBPM formalism, for the waveguide geometries considered above was 3.27. Given this value and the optical properties of the laser material such as its photoluminescence spectrum, a target Bragg period can be determined. In summary we have shown that by proper design of the waveguide and grating parameters, LC-DFB structures provide the necessary coupling for laser operation.

3.2.2 Reverse-Mesa RWG LC-DFB

The laser mesa structures which we are working with have vertical sidewalls, as depicted in Figure 3-5. Recently, a reverse-mesa ridge-waveguide (RM-RWG) laser structure, shown schematically in Figure 3-17 along with the more conventional vertical-mesa ridge-waveguide (VM-RWG) laser structure, has been demonstrated

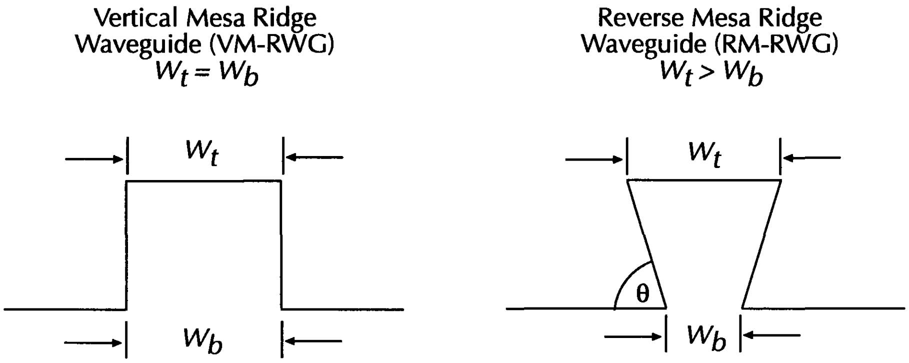

Figure 3-17: Schematic of a vertical-mesa (VM) and reverse-mesa (RM) ridge-waveguide (RWG) structures.

which has a reduced threshold current and reduced series resistance compared to similar VM-RWG lasers [77]. These reductions offer improved high-power and wide-temperature-range operation. Next, we investigate the degree of coupling obtainable with lateral gratings on RM-RWG laser structures.

Referring to Figure 3-17, given the guide widths at the top of the ridge, W_t, the guide width at the bottom of the ridge, W_b, can be determined once the sidewall angle and ridge height are known. The sidewalls of the RM-RWG structure are the (111)A plane of the InP top cladding layer and are formed by a Br-based InP-InGaAs(P) selective wet etchant. Therefore, the sidewall angle, θ, is 54.7^o. Because of the sidewall taper, the top of the ridge overhangs or shadows the bottom of the ridge. Consequently, lateral gratings will not be patterned in these shadowed regions. We consider the case where W_t is 2.0 μm and compare it to a VM-RWG structure of width 2.0 μm as well. For the layer structure in Figure 3-7 the ridge height is 1.115 μm, resulting in a W_b of 0.44 μm. Simulations were also performed in which W_t and W_b were 3.56 μm and 2.0 μm, respectively. However, it was found that negligible coupling ($\sim$1-2 cm^{-1}) occurs for this waveguide geometry.

Figure 3-18 plots κ as a function of grating etch depth for both RM-RWG and VM-RWG laser structures for a 1st-order grating with a 70% duty cycle. Clearly, the

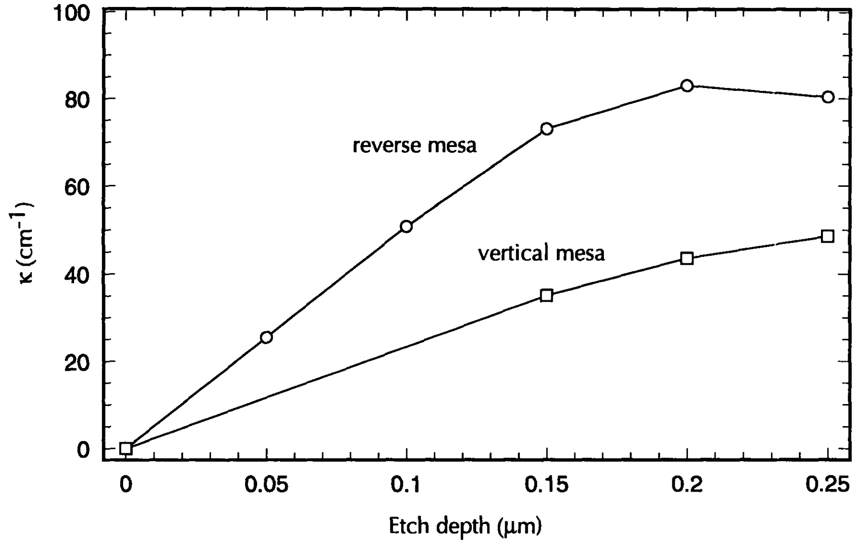

Figure 3-18: Comparison of VM-RWG and RM-RWG laser structures: κ vs. grating etch depth for a 70% duty cycle 1st-order grating. The VM-RWG width is 2.0 μm. The top width and bottom width of the RM-RWG are 2.0 μm and 0.44 μm, respectively.

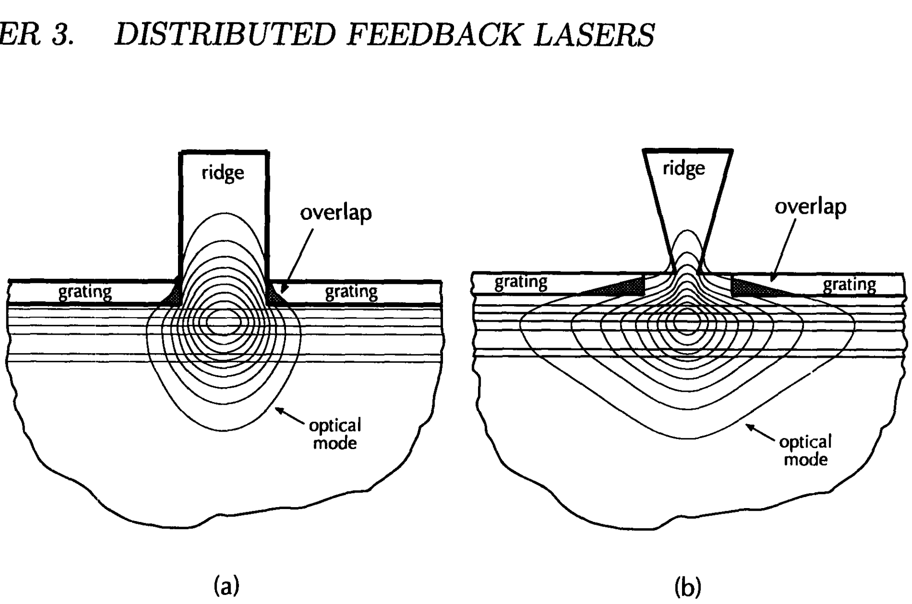

Figure 3-19: Comparison of optical mode overlap with lateral gratings: (*a*) VM-RWG structure and (*b*) RM-RWG structure.

degree of coupling for the RM-RWG is much higher, by approximately a factor of 2. Qualitatively, this fact can be understood as follows.

Since W_b for the RM-RWG is less than W_b for the VM-RWG, the degree of lateral confinement is less for the RM-RWG. Consequently, the mode extends further out in the lateral dimension which increases the mode overlap with the grating. This fact is illustrated in Figure 3-19 which compares the overlap of the optical mode with the lateral grating for the VM-RWG and RM-RWG structures considered above.

Using a similar argument, one can explain why a laterally-coupled RM-RWG structure with a W_b of 2.0 μm provides negligible coupling. The degree of lateral confinement is essentially the same as that for a VM-RWG structure of width 2.0 μm. However, the lateral gratings for this RM-RWG structure are located approximately 0.8 μm away from the optical mode due to the shadowing which occurs during the pattern transfer of the lateral gratings. Therefore, one can think of the laterally-coupled RM-RWG structure with a W_b of 2.0 μm as a laterally-coupled VM-RWG structure with a W_b of 2.0 μm and a Δ-value of 0.8 μm.

Figure 3-20 plots κ as a function of Δ for both RM-RWG and VM-RWG laser

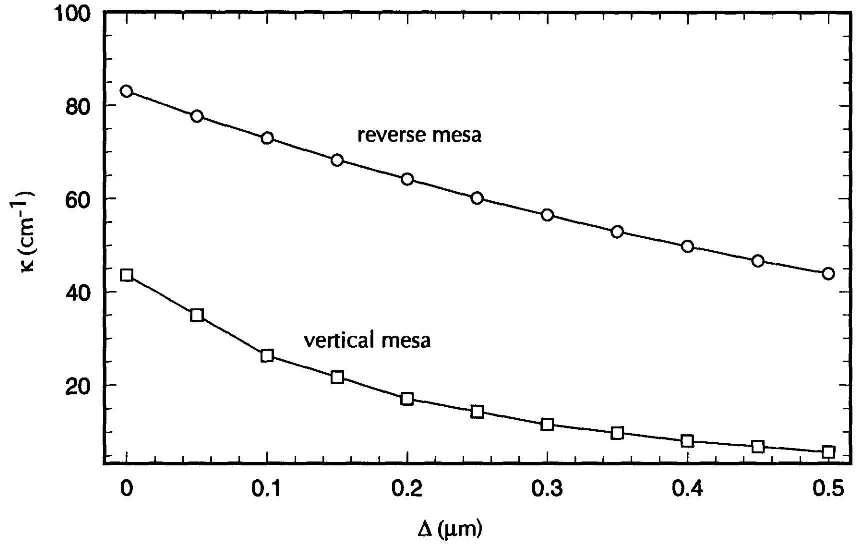

Figure 3-20: Comparison of VM-RWG and RM-RWG laser structures: κ vs. Δ for a 70% duty cycle 1st-order grating and a grating etch depth of 0.2 μm. The VM-RWG width is 2.0 μm. The top width and bottom width of the RM-RWG are 2.0 μm and 0.44 μm, respectively.

structures for a 1st-order grating with a 70% duty cycle and a grating etch depth of 0.2 μm. As expected, the coupling for both structures decreases for increasing Δ. However, as in Figure 3-18, much larger values of κ are obtainable with the RM-RWG structure. Even at a Δ-value of 0.5 μm, the κ for the RM-RWG structure is higher than that for the VM-RWG structure at a Δ-value of 0. Therefore, for a given target κ the RM-RWG LC-DFB structure offers increased tolerance on the lateral grating fabrication as opposed to the VM-RWG LC-DFB structure.

In summary, a RM-RWG LC-DFB laser can provide both improved device performance and relaxed fabrication tolerances over a VM-RWG LC-DFB laser, which itself offers advantages over more conventional DFB lasers. From the standpoint of the lateral grating fabrication, the processing involved for both structures are identical. Therefore, the nanofabrication technology developed in this work is directly applicable to the fabrication of RM-RWG, as well as VM-RWG, LC-DFB lasers.

3.3 Lateral Grating Fabrication

In the previous section we introduced the concept of lateral coupling for DFB lasers. The major challenge of the LC-DFB device fabrication is the patterning of the lateral gratings. To achieve the necessary coupling for laser action, as well as reliable control of coupling from device-to-device, these gratings should run right up to the ridge sidewall, as shown in Figure 3-11. One can also conclude that lateral gratings which reside closer to the ridge sidewall also relax the tolerance on the grating duty cycle. Because of the fine linewidths required (i.e. sub-100 nm) as well as the topography of the ridge-waveguide substrates, the fabrication of the lateral gratings is a non-trivial task. In this section we present the techniques we have developed for patterning such gratings.

3.3.1 Lithography

To achieve good optical mode confinement, typical ridge heights are 1 μm or greater. Because of this significant topography, spun-on resist tends to build up right next to the ridge sidewall. Therefore, while the resist thickness may be uniform and thin in regions away from the ridge, it can be thicker than the ridge height near the sidewall. A resist layer of such uneven thickness leads to problems in the subsequent exposure and development stages, especially since the feature sizes of interest for DFB lasers are of the order of 100 nm. In addition, even if one succeeds in exposing and developing uniform 100 nm linewidths, experience indicates that they will not be self-supporting and will partially collapse in regions where the resist thickness exceeds about 500 nm (for an aspect ratio of 5), as it does immediately adjacent to the ridge.

Figure 3-21 shows a 230 nm-period PMMA grating patterned over a 1 μm-high InP ridge-waveguide with x-ray lithography. As shown, the PMMA thickness varies considerably over the topography, ranging from about 150 nm far away from the ridge sidewall to approximately 600 nm right next to the ridge sidewall. Figure 3-22

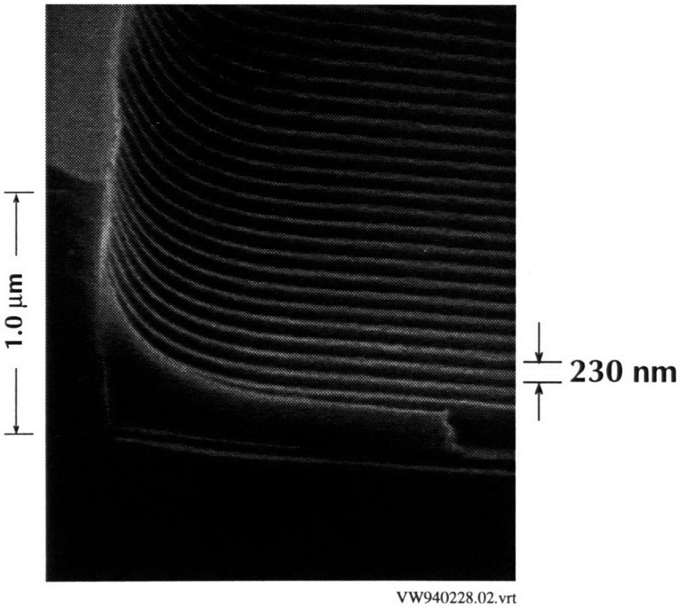

Figure 3-21: PMMA grating ($\Lambda = 230$ nm) exposed using x-ray lithography onto a 1 μm-high InP ridge-waveguide.

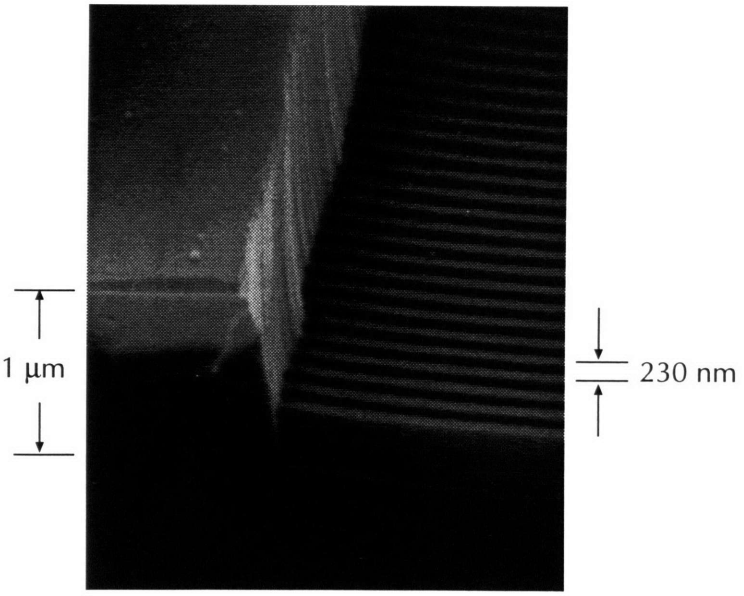

Figure 3-22: Pattern transfer of 230 nm-period grating into the channels of a 1 μm-high InP ridge-waveguide using CH_4/H_2 RIE (see Section 3.3.2). The etch depth is 250 nm.

shows the pattern transfer of this 230 nm-period grating into the channels of the InP ridge-waveguide with CH_4/H_2 RIE ($CH_4/H_2 = 10/40$ sccm, 20 mT, 400V) to an etch depth of 250 nm.

In Figure 3-21 the spinning conditions and viscosity of the PMMA were chosen such that the PMMA next to the sidewall did not exceed ~600 nm, above which the patterned resist lines would be mechanically unstable. This restriction resulted in a 150 nm-thick PMMA film, which was effectively 'overdeveloped', further away from the sidewall. Such thin films are often not suitable as liftoff or RIE masks. Therefore, a means of reducing the non-uniformity of spun-on resist which occurs over

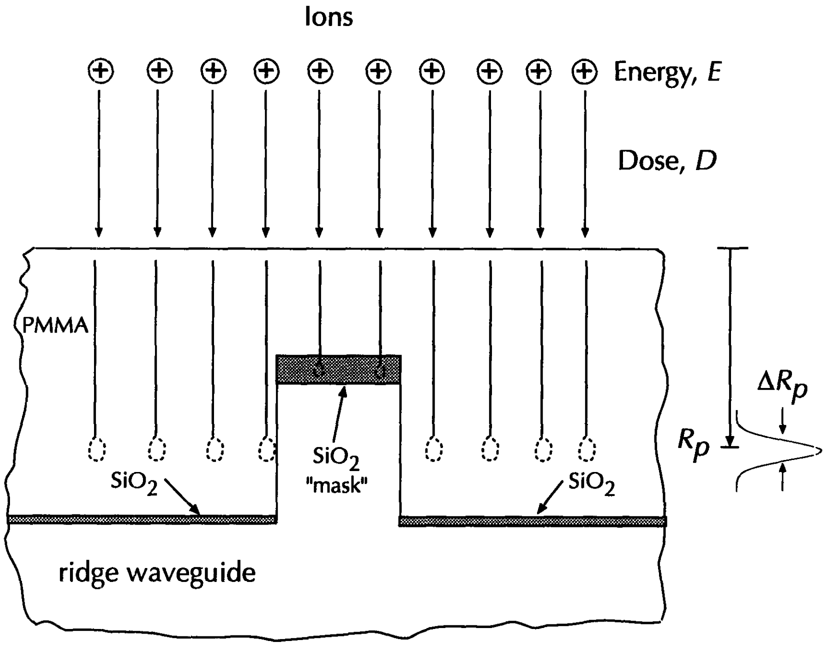

Figure 3-23: Schematic illustrating the basic concept of the fabrication process.

substrate topography would allow the use of thicker PMMA films as well as increase the process latitude during resist development. We demonstrate here a method of making the resist uniform and of moderate thickness up to the very edge of the ridge sidewall. Our approach represents a novel application of ion implantation. Under the proper implantation conditions a layer of resist can be 'thinned down' to a uniform thickness. The process is used in conjunction with x-ray lithography, although it is also applicable to electron-beam [81] or ion-beam lithography.

We utilize the well-developed technology of ion implantation to reduce the thickness variations of spun-on resist, which in our case is PMMA, on ridge-waveguides with heights exceeding 1 μm. Figure 3-23 illustrates the basic concept of the process. A thick planarizing layer of PMMA is first spun onto the substrate containing the ridge-waveguides. For typical ridge heights of $\sim 1\mu$m, planarizing resist layers need to be $\sim 2\mu$m-thick. The substrate is then implanted. The accelerating voltage and ion species are chosen to penetrate a given depth into the PMMA layer, and the dose is chosen so that the implanted layer of PMMA can be developed away, leaving a thinner layer of PMMA behind. This layer will have uniform thickness up to the edge of the ridge sidewall. At this point, a second implant can be performed to 'fine-tune' the resist thickness if desired. Following the implants, either x-ray, electron-beam or ion-beam lithography can be performed to pattern the lateral grating immediately adjacent to the ridge sidewall.

Figure 3-24 plots the calculated range, R_p, as a function of ion energy using TRIM Monte Carlo software [93] of Boron and Phosphorous ions in PMMA and silicon dioxide (SiO_2). Figure 3-24 shows that if damage is not an issue, this planarizing layer can be 'thinned down' by the above process in a single implant/development step. On the other hand, if damage is an issue, one can utilize multiple implant-develop steps. In particular, in a first step one can implant the resist layer down to a masking material (such as the SiO_2 layer in Figure 3-23) followed by development and subsequent implants with energies dictated by the projected range and longitudinal straggle in the masking material. In this way one can 'thin down' the remaining resist without producing damage.

A silicon substrate was spin-coated with PMMA to a thickness of 1.5 μm. Figure 3-25 plots the depth developed away versus development time from three separate phosphorous ion implants at energies of 500, 600 and 700 keV and a dose of 10^{13} cm^{-2}. The PMMA was developed in a 1:2 mixture of methyl-iso-butyl-ketone:isopropyl alcohol (MIBK:IPA) at 21°C. As shown, the depth developed saturates at approximately 20 sec, after which negligible development occurs.Thus the depth of resist developed away can be accurately controlled by adjusting the ion energy. It was found that ion energies above $\sim$ 1.2 MeV resulted in PMMA films that were rough after development; therefore, the ion energies were kept below this level. Previously, Adesida *et al.* [94] performed an extensive study on the range of light ions (i.e. H^+, H_2^+, He^+, Li^+, Be^+, B^+, and C^+) in polymeric resists such as PMMA, for energies ranging between 50 and 300 keV. They also observed the saturated depth behavior shown in

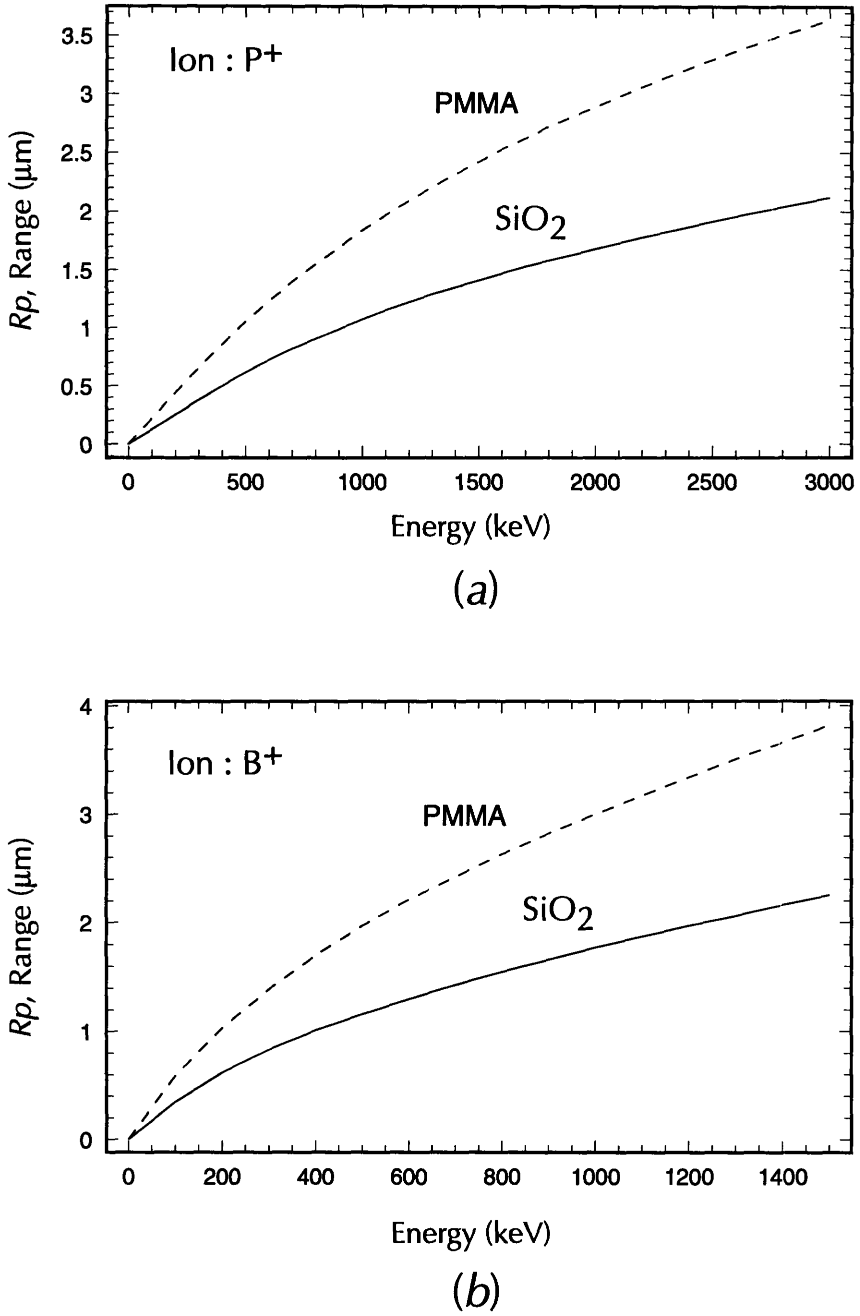

Figure 3-24: Calculated range, R_p, in PMMA and SiO_2: (*a*) boron ions and (*b*) phosphorous ions.

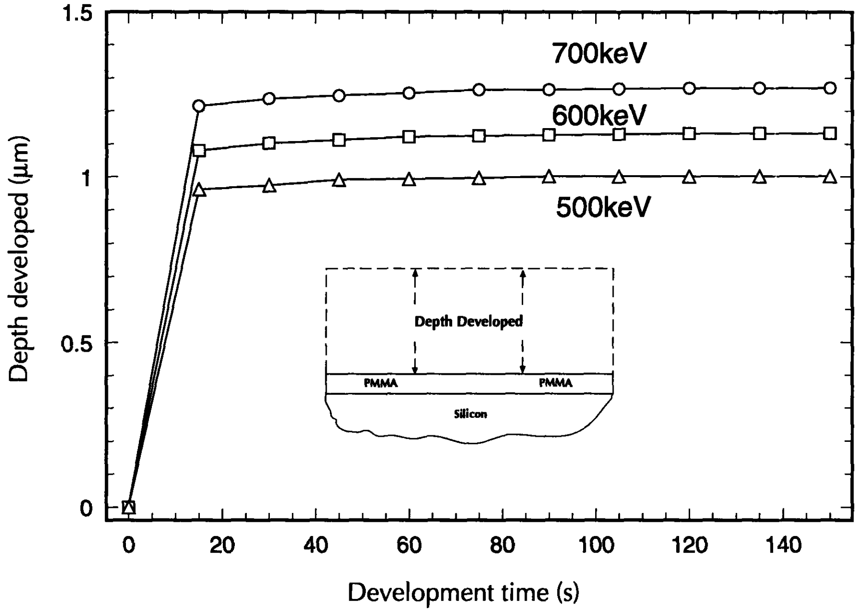

Figure 3-25: Plot of the depth of PMMA developed away versus development time for three phosphorous ion implants at energies of 500, 600 and 700 keV. The ion dose was 1 X 10^{13} cm^{-2}. The PMMA was developed in a 1:2 mixture of MIBK:IPA at 21°C.

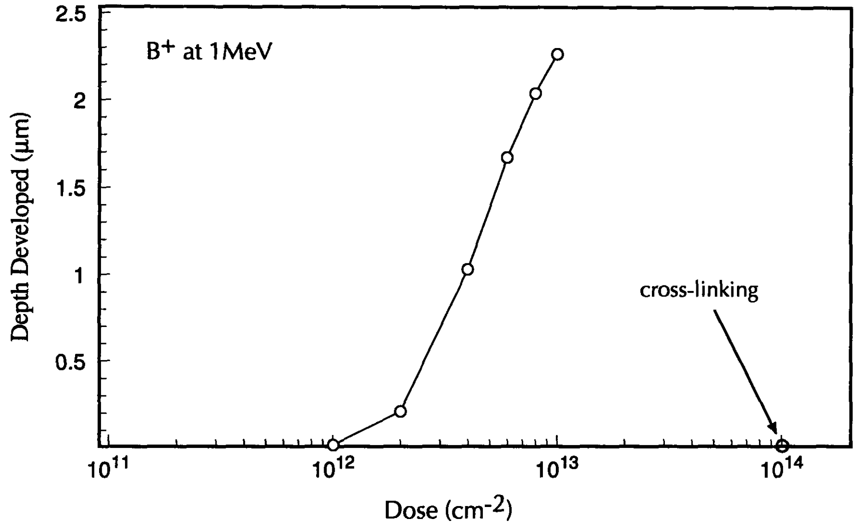

Figure 3-26: Plot of the depth of PMMA developed away versus development time for boron ion implants at an energy of 1 MeV and doses of 1 X 10^{12}, 2 X 10^{12}, 4 X 10^{12}, 6 X 10^{12}, 8 X 10^{12}, 1 X 10^{13} cm^{-2}. The PMMA was developed in a 1:2 mixture of MIBK:IPA at 21°C.

Figure 3-25.

Figure 3-26 plots the depth of PMMA developed away, starting with a PMMA thickness of 4.0-μm, versus development time for boron ion implants at an energy of 1 MeV and doses between 10^{12} and 10^{13} cm^{-2}. Negligible development occurs at a dose of 10^{12} cm^{-2}. In all other cases, as in Figure 3-25, the depth of PMMA developed away saturates. Figure 4 plots depth developed versus dose, illustrating a threshold at 10^{12} cm^{-2}. At a dose of 10^{14} cm^{-2}, carbonization and cross-linking of the resist occurs which inhibits development.

Figures 3-25 and 3-26 also show that the depth developed in PMMA can be adjusted by varying either the ion energy or the ion dose. Subsequent implants were performed at a dose of 1 X 10^{13} cm^{-2}, well above the threshold clearing dose for PMMA shown in Figure 3-27, while the ion energy was adjusted to tailor the developed depth.

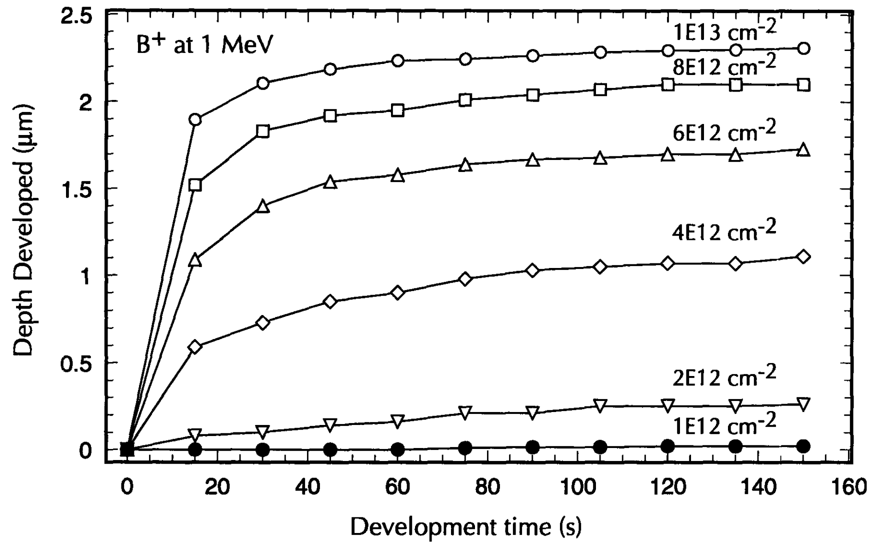

Figure 3-27: Plot of the depth of PMMA developed away versus ion dose for boron implants at an energy of 1 MeV. The PMMA was developed in a 1:2 mixture of MIBK:IPA at 21°C for 150 sec. As shown, the threshold for development occurs at a dose of 10^{12} cm^{-2}. At a dose of 10^{14} cm^{-2} carbonization and cross-linking of the PMMA occurs which inhibits development.

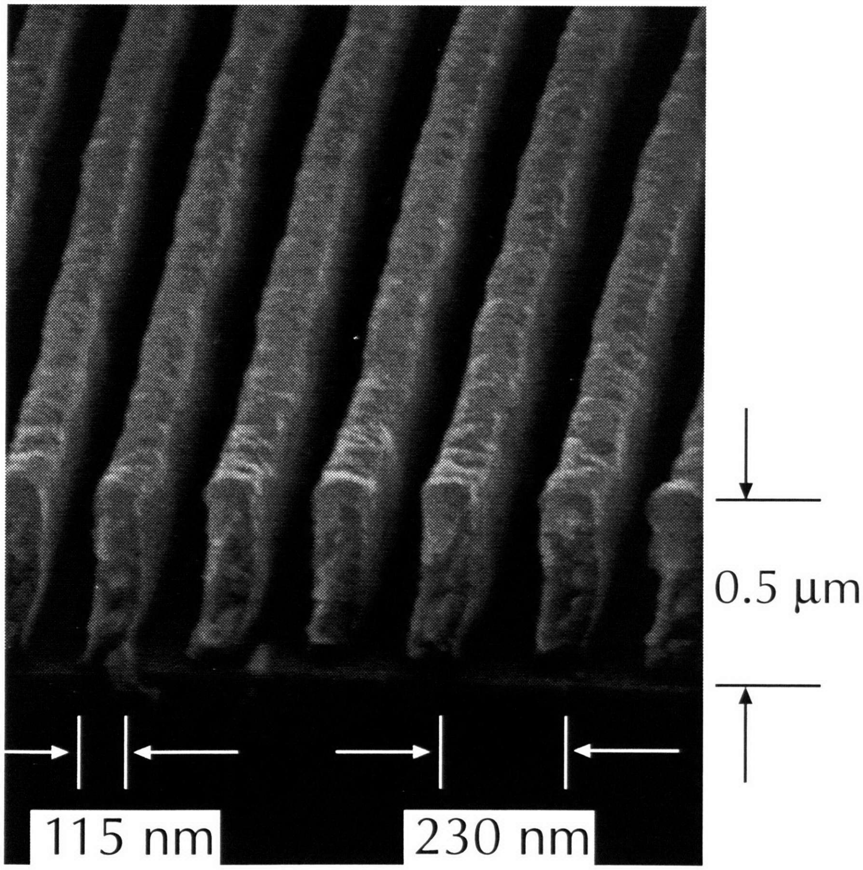

Figure 3-28: Scanning electron micrograph is a 230 nm-period grating exposed in PMMA by x-ray lithography. Prior to the x-ray exposure, the PMMA had gone through two ion implantation/development steps: (*a*) a boron ion implant at an energy of 1.2 MeV and develop in 1:2 MIBK:IPA at 21°C for 150 sec and (*b*) a boron ion implant at an energy of 70 keV and develop in 1:2 MIBK:IPA at 21°C for 150 sec. The grating lines have vertical sidewalls and demonstrate that the boron implants have not compromised the characteristics of the PMMA.

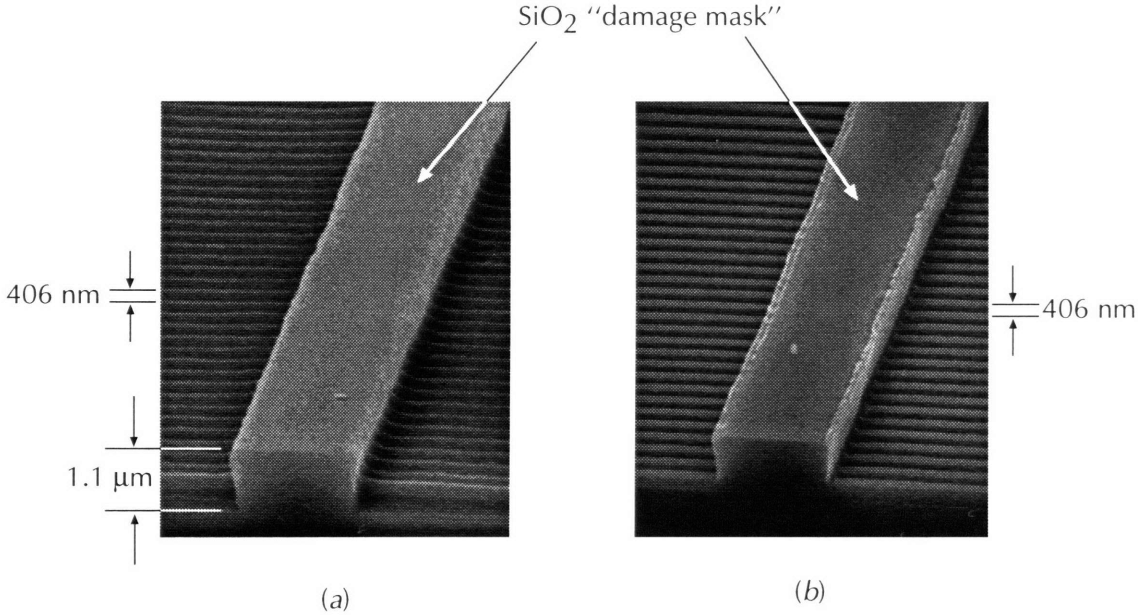

(*a*) (*b*)

Figure 3-29: Lateral gratings defined on a 1.1 μm-high InP/InGaAlAs/InGaAsP ridge-waveguide. The grating has a period of 406 nm which is appropriate for a 2nd-order DFB laser at 1.3 μm. The silicon dioxide damage mask serves both as an RIE etch mask as well as an ion implantation damage mask. (*a*) Scanning electron micrograph of a 406 nm-period lateral grating exposed in PMMA by x-ray lithography, (*b*) Scanning electron micrograph of lateral gratings defined by CH_4/H_2 RIE.

The ion implantation process does not appear to compromise the resolution of the PMMA film that remains after multiple implant/development steps. For example, Figure 3-28 shows a high resolution pattern developed in 0.5 μm-thick PMMA. The starting film was 4 μm-thick and was implanted with boron ions at 1.2 MeV and 10^{13} cm^{-2}. Development in 1:2 MIBK:IPA at 21^{o}C for 150 s thinned this down to 0.9 μm. A second boron implant at 70 keV and 10^{13} cm^{-2}, plus development at 21^{o}C for 150 s left the 0.5 μm of PMMA remaining in which the result of Figure 3-28 was obtained.

The ion implantation process was used to fabricate lateral gratings adjacent to 1.1 μm-high ridge-waveguides. The ridge-waveguides were defined in InP/InGaAlAs/InGaAsP by reactive-ion-etching (RIE) using a 275 nm-thick layer of SiO_2 as the mask. This SiO_2 mask is left in place during ion implantation to prevent damage of the ridge material. The RIE etch mask for the pattern transfer of the lateral gratings into the InP was 50 nm of SiO_2, which is deposited after the RIE of the ridge-waveguides. PMMA was used as the etch mask for patterning this SiO_2 layer. An intermittent etch (10 s etch followed by a 90 s latent period) in CHF_3 (Perkin Elmer 3140-8J model RIE, 15 sccm, 10 mT, 600 V, total etch time of 70 s) using the PMMA grating as an etch mask was used to pattern this SiO_2 layer. A continuous etch cycle severely eroded the PMMA and resulted in unacceptable isotropy.

Once the ridge-waveguides were defined, a 4.3 μm-thick planarizing layer of PMMA was spun on and baked at 180°C for 1 hour. Following this, three ion implantation/development steps were performed: (*i*) boron; 700 keV; 10^{13} cm^{-2}; 1:2 MIBK:IPA at 21°C for 150 s; (*ii*) boron; 120 keV; 10^{13} cm^{-2}; 1:2 MIBK:IPA at 21°C for 150 s, and (*iii*) boron; 80 keV; 10^{13} cm^{-2}; 1:2 MIBK:IPA at 21°C for 150 s. After these steps 0.6 μm of PMMA remained. A 406 nm-period lateral grating, corresponding to a 2nd-order DFB laser at 1.3 μm, was defined by x-ray lithography, as shown in Fig 3-29(*a*), and transferred into the InP-cladding layer by CH_4/H_2 RIE (CH_4/H_2 = 10/40 sccm, 20 mtorr, 400V). The total etch time was 9 minutes. However, after every 3 minutes an oxygen RIE step was performed to prevent polymer buildup which compromises the anisotropy of the etched profiles. The resultant lateral gratings which run right up to the ridge sidewall are shown in Fig 3-29(*b*).

In this work boron ions (B^+) and phosphorous ions (P^+) were used because they are readily available. Lighter ions, such as hydrogen (H^+) and helium (He^+), have much larger ranges in resist (e.g. at an energy of 100 keV, H^+ has a range of ~1.5 μm compared to ~0.59 μm for B^+). Consequently, lower energies (and simpler implanters) can be used. In addition, since the lighter H^+ and He^+ ions give up most of their energy to electrons, the longitudinal straggle (for a given ion range) is much reduced (e.g. for an ion range of 1.5 μm, H^+ has a longitudinal straggle of ~84 nm compared to ~113 nm for B^+).

Attempts were made at fabricating LC-DFB lasers. However, we were not able to observe any lasing due to the Bragg gratings. We attribute this to errors in the determination of the effective index, n_{eff}. The IDBPM simulations determined an effective index of 3.27 for the layer structures and waveguide geometries we were working with. However, the extracted n_{eff}'s from recent experimental measurements for DFB lasers fabricated on similar materials at Lasertron, Inc. was 3.22. Consequently, the grating periods we used were lower than required which detuned the Bragg frequency from the gain peak of the material. We believe this detuning extinguished the DFB modes in the lasers. A standard Fabry-Perot spectrum was observed in the measured devices. We used holographically-defined gratings for these experiments. In the future a more practical approach would be to pattern the DFB grating by EBL and include a range of grating periods on the x-ray mask. In this way one can ensure that the range of grating periods patterned overlaps with the gain peak of the laser material.

3.3.2 Reactive-Ion-Etching

The RIE of the InP-based material is done with a CH_4/H_2 gas chemistry on a Plasma Therm 7000 model RIE. As is well-known, polymer buildup occurs during etching in CH_4/H_2 [95–98]. The polymer deposits on top of the masking material which tends to result in a widening of the masking material as well as increased scattering off of the masking material. Both of these effects compromise the etched sidewall profile.

Figure 3-30 shows an InP grating etched continuously in CH_4/H_2 for 10 minutes (CH_4/H_2 = 10/40 sccm, 20 mT, 400V). As shown the sidewalls are sloped. Figure 3-31 shows an InP grating etched for a total of 10 minutes with an oxygen clean step after every 3 min of etching in CH_4/H_2 with the same parameters as in Figure 3-30. A similar process has been used for etching InP-based material in a CAIBE system [96]. As shown, the sidewalls are vertical and smooth.

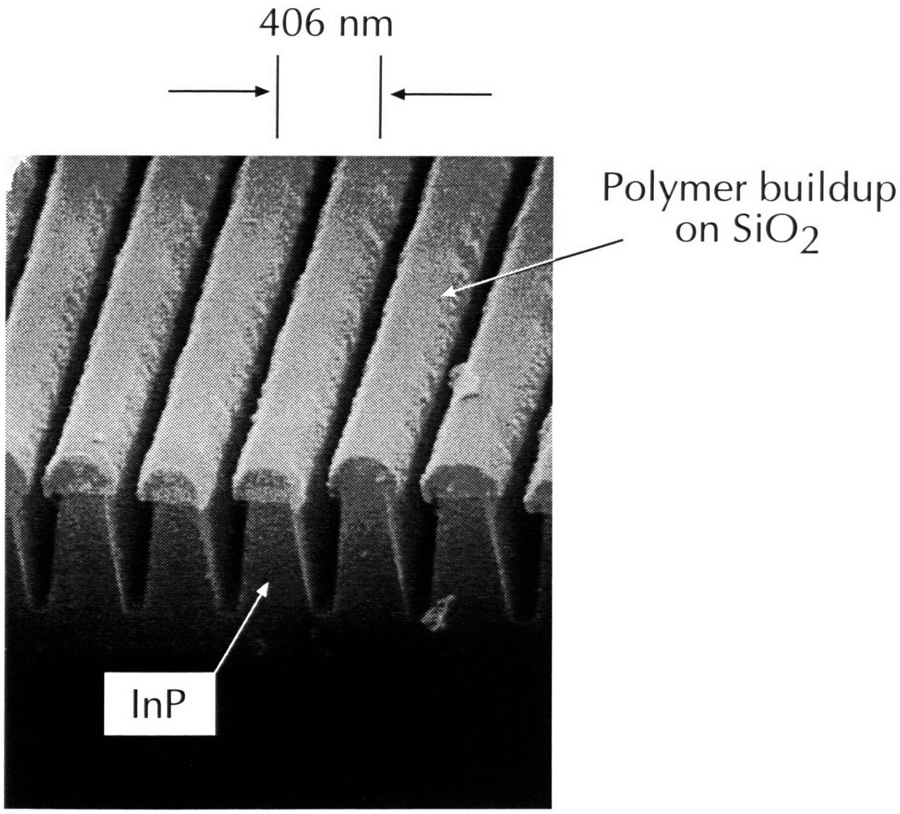

Figure 3-30: Pattern transfer of a 406 nm-period grating into InP with a continuous RIE step in CH_4/H_2.

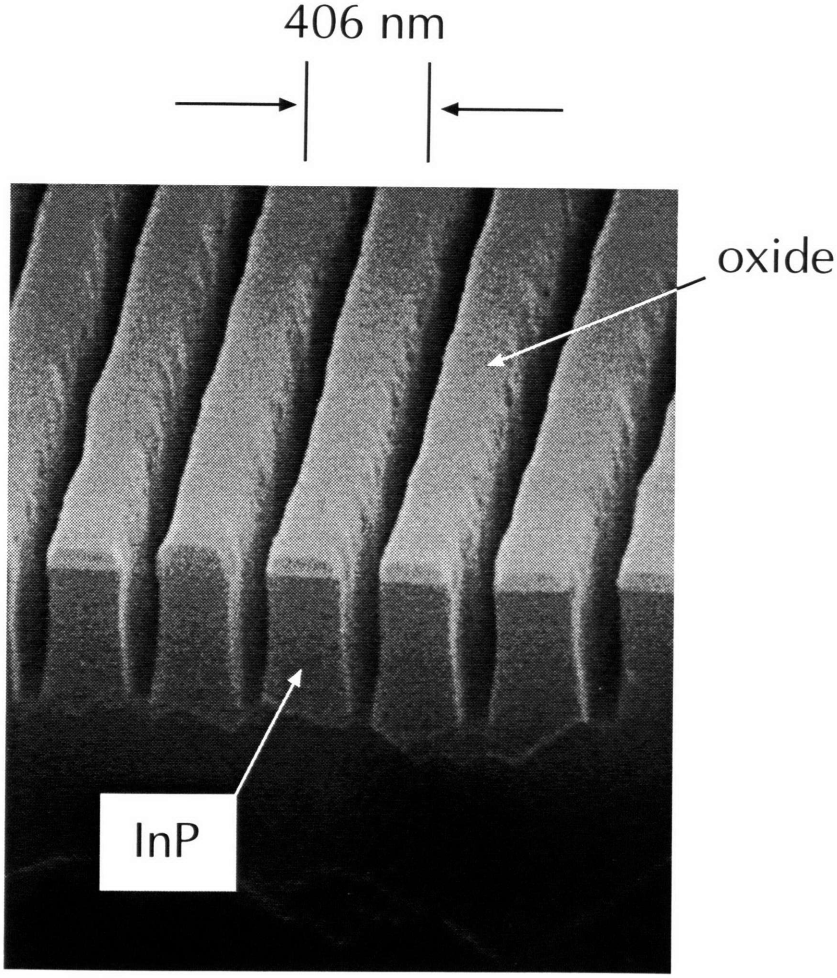

Figure 3-31: Pattern transfer of a 406 nm-period grating into InP with intermittent O_2 and CH_4/H_2 RIE steps. The improved sidewalls compared to those in Figure 3-30 are due to the removal of the polymer buildup over the course of a CH_4/H_2 RIE step.

3.3.3 Duty cycle control

As shown in Figures 3-10 and 3-15, the duty cycle has a significant effect on the coupling in LC-DFB structures. For the device geometries considered in Figures 3-10 and 3-15, the optimum duty cycles range from 70% to 80%. Since one typically uses a 'daughter' mask for exposing the grating-based devices, duty cycles between 20% to 30% on the 'mother' mask are required. In our holography process the duty cycle of the 'mother' mask is controlled primarily by the angle at which the SiO_2 etch mask is shadow-evaporated. In practice, it is difficult to achieve duty cycles much below 40%. By accounting for diffraction and lateral development effects [99] in the mask replication, one can realize the required duty cycles. However, the relatively low process latitude of this approach limits its usefulness. We present here a process that can be used (in conjunction with the above approach as well), to accurately obtain grating masks with the required duty cycles. Gratings with duty cycles up to 90% have been fabricated using this technique.

First, as described above, an x-ray exposure is performed to replicate a holography 'mother' mask. Resist development and gold electroplating are used to define the grating 'daughter' mask. Figure 3-32(a) shows a 406 nm-period grating mask with a 75% duty cycle fabricated in this manner. After plating, the resist is removed. The mask now consists of regions containing either the gold absorbers defined by plating or a plating base of 5 nm NiCr and 10 nm Au. The mask is now plated again. Because all of the surfaces will plate, the gold absorbers can be widened and therefore the duty cycle increased. Figure 3-32(b) shows a 406 nm-period, 90% duty cycle grating generated in this way. This grating was obtained by plating an additional 30 nm on the mask shown in Figure 3-32(a). Note that the transmissivity of the mask in Figure 3-32(b) is lower than the mask in Figure 3-32(a) with the difference being due to the additional 30 nm of plated gold.

Figure 3-33 shows PMMA resist contours (original thickness = 630 nm) for various development times, 5, 10, 15, 30, 45 and 60 sec, for a contact x-ray exposure ($\lambda =$

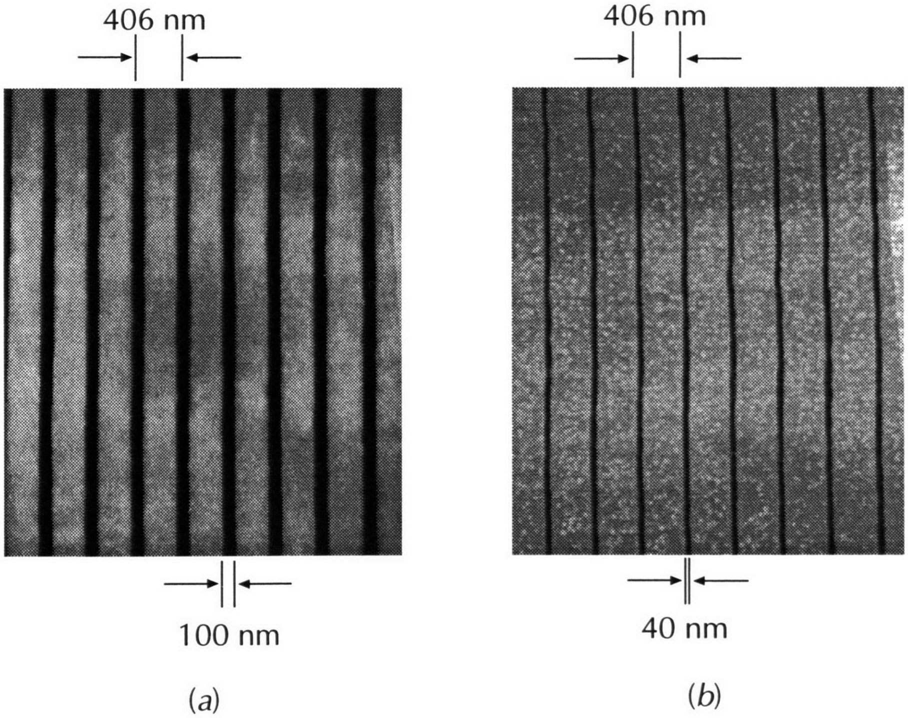

Figure 3-32: Scanning electron micrographs of 406 nm-period gratings: (*a*) 75% duty cycle and (*b*) mask in (*a*) after plating an additional 30 nm of gold. As shown, the gold absorbers have widened. The duty cycle is 90%.

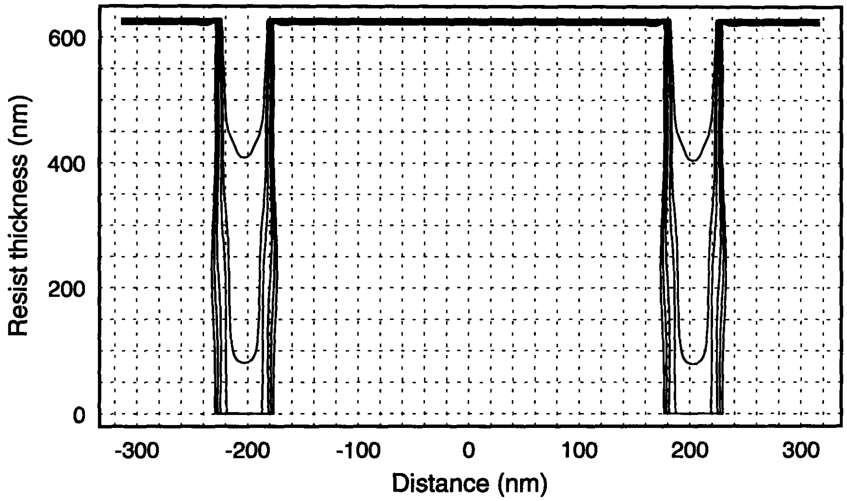

Figure 3-33: PMMA resist contours (original thickness = 630 nm) for various development times, 5, 10, 15, 30, 45 and 60 sec, for a contact x-ray exposure (λ = 1.32 nm) of a 406 nm-period grating (~90% duty cycle) mask at a dose of 1100 J/cm^3 (using the computer model described in reference [99]).

1.32 nm) of a 406 nm-period grating mask of duty cycle 90% at a dose of 1100 J/cm^3. The computer model used is described in detail in reference [99]. As shown, the resist profiles are essentially vertical, although there is a slight widening of the trench towards the bottom of the resist layer. This widening is due to a combination of diffraction and lateral development effects.

Figure 3-34 shows the pattern transfer of the 406 nm-period grating shown in Figure 3-32(*b*) into PMMA (630 nm). As one can see, the resist profile is essentially vertical. The effects of diffraction and lateral development shown in Figure 3-33 are also evident towards the bottom of the resist layer where the spacewidth widens to 50 nm. Figure 3-35 shows the pattern transfer of this grating into an InP substrate with CH_4/H_2 RIE with an oxide etch mask (as decribed in Section 3.3.2).

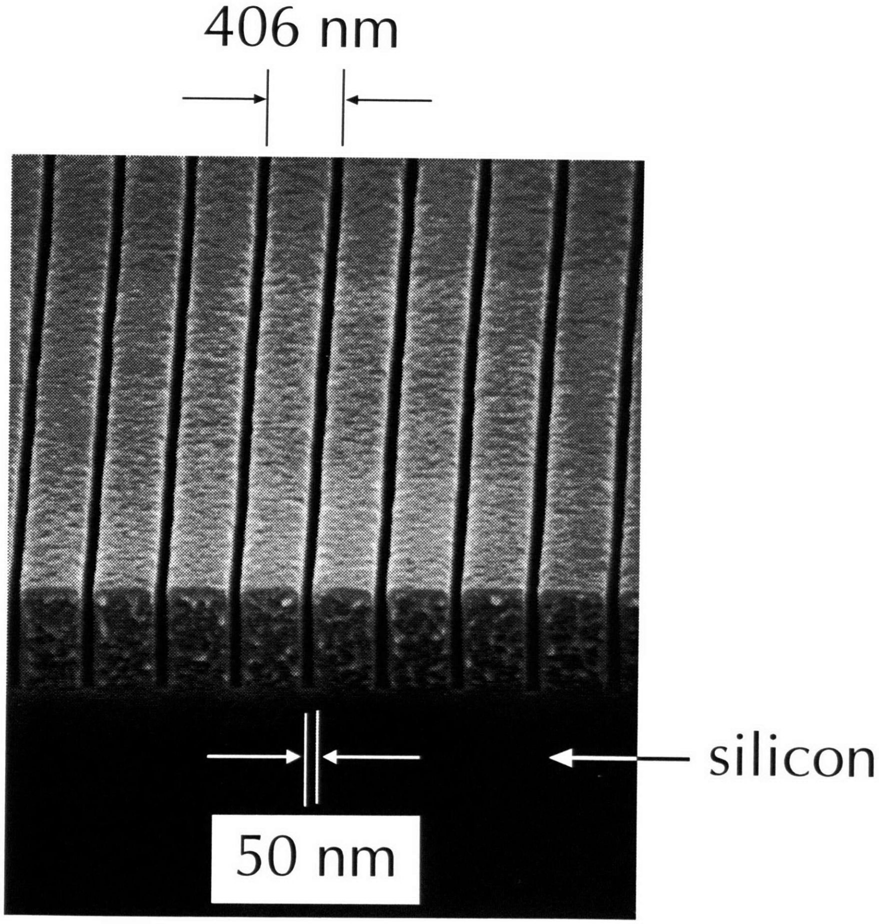

Figure 3-34: Pattern transfer into PMMA using x-ray lithography of the grating mask shown in Figure 3-32(*b*) ($\Lambda = 406$ nm, 90% duty cycle).

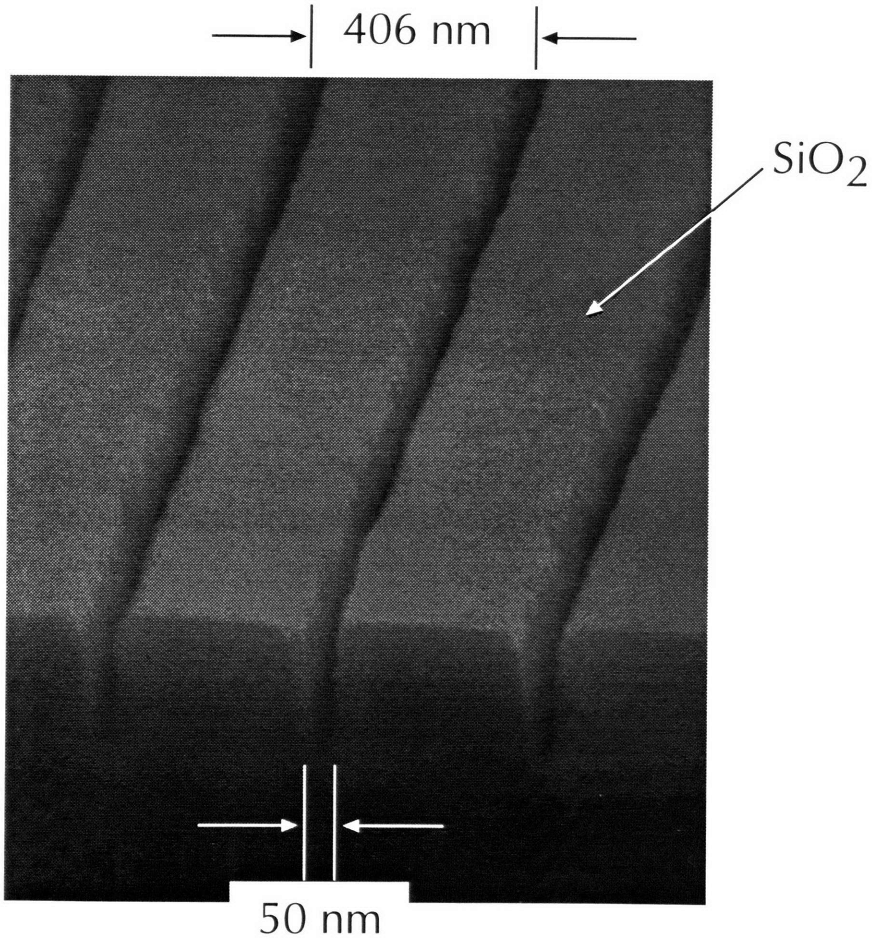

Figure 3-35: Pattern transfer of the 406 nm-period grating shown in Figure 3-34 into InP with CH_4/H_2 RIE.

3.3.4 Summary

The technology driver for the development of the nanofabrication methods described in this section is the laterally-coupled DFB laser. Unlike conventional DFB lasers which rely on buried gratings for optical feedback, this device relies on lateral gratings, which are patterned on the substrate surface after both the epitaxial growth and the ridge-waveguide formation. The device structure of the LC-DFB laser requires that lithography be performed over deep topography (i.e. $\geq 1\mu$m). In this regard a technique using ion implantation has been developed to minimize the non-uniformity of spun-on resist on substrates containing significant topography. This technique, combined with x-ray lithography, was used to pattern transfer lateral gratings onto ridge-waveguides which are representative of actual device ridge-waveguides. Reactive-ion-etching processes have also been developed to pattern transfer into InP-based material. The pattern transfer methods described herein can be combined with spatial-phase-locked electron-beam lithography (for the definition of the requisite device grating patterns onto an x-ray mask, as described in Chapter 2) for the fabrication of LC-DFB lasers.

Chapter 4

Bragg-Grating-Based Optical Filters

As discussed in Chapter 3, Bragg gratings provide the necessary feedback and frequency-selectivity for efficient laser action. These gratings can also be used to implement narrow-band optical filters. Such filters are essential to high-capacity WDM optical communications systems. In order to increase the aggregate bit rate of WDM optical communications systems, the inter-channel spacing can be reduced (e.g. to ~0.5 nm) thereby increasing the channel density. As the channel spacing is reduced, however, the bandwidth of the demultiplexing optical filters must also be commensurately reduced (e.g. to ~0.1 nm).

The simplest optical filter in the class of Bragg-grating-based optical filters is the quarter-wave-shifted (QWS) Bragg resonator which is also referred to as a single-pole or Lorentzian filter. This filter is characterized by a single high-Q resonance. The transmission response of a typical QWS Bragg resonator as a function of wavelength (or, equivalently, frequency) is shown in Figure 4-1.

Further tailoring of the filter response can be achieved by cascading several single-pole filters of the same resonant frequency to form higher-order, or multiple-pole, filters [16,17,100]. The resonators in the cascade couple to one another across the grating

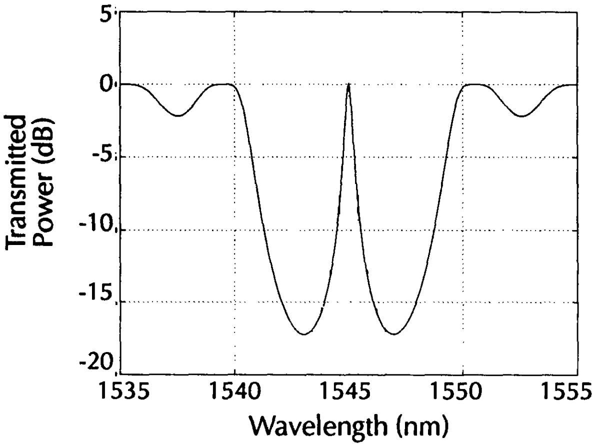

Figure 4-1: Transmission response of a QWS Bragg resonator as a function of wavelength.

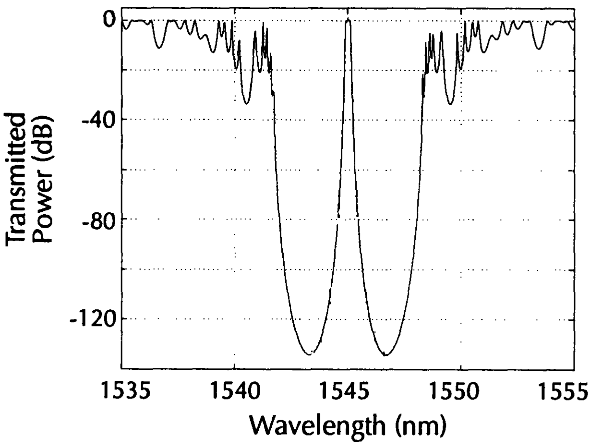

Figure 4-2: Transmission response of a 7th-order Butterworth filter as a function of wavelength.

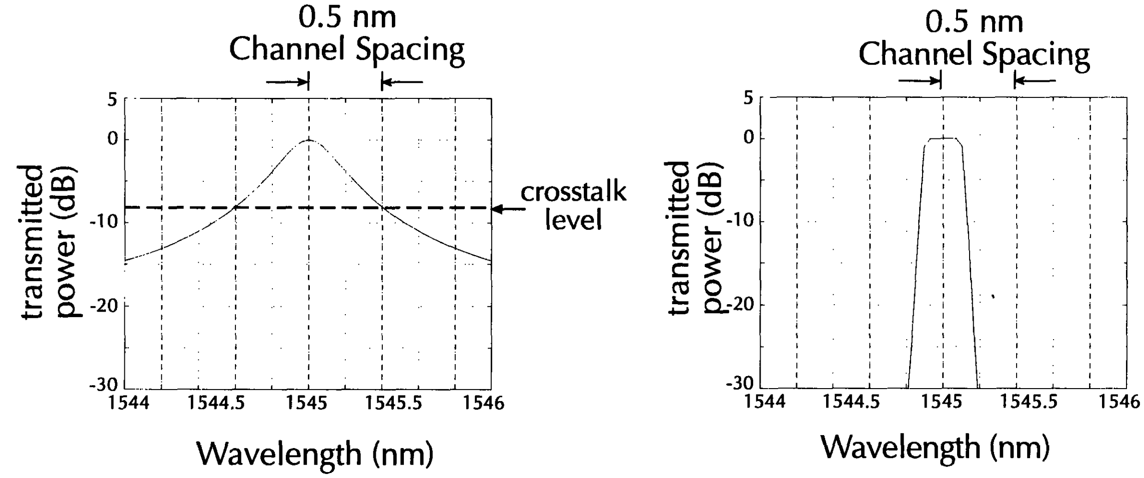

(*a*) (*b*)

Figure 4-3: Magnified views of Figures 4-1 and 4-2 near resonance: (*a*) QWS Bragg resonator and (*b*) 7th-order Butterworth filter. Also shown is the 0.5 nm channel spacing of a high-capacity WDM system. The response in (*b*) is flatter near resonance and also has a lower level of crosstalk than the response in (*a*).

lengths, thereby splitting the frequency degeneracy. The degree of coupling between resonators is determined by the resonator lengths (for a given grating strength, κ), which can be determined using standard filter synthesis techniques. Multiple-pole filters come in several forms: Gaussian, Butterworth and Chebyshev. Figure 4-2 shows the transmission response of a 7th-order Butterworth filter as a function of frequency.

Two important characteristics of a given filter are the filter response near resonance and the rate of fall-off away from resonance. A flatter response near resonance results in lower distortion and a faster fall-off away from resonance results in a lower level of inter-channel crosstalk. To compare the responses in Figures 4-1 and 4-2, magnified views near resonance are shown in Figure 4-3(*a*) and (*b*), respectively. Also shown in Figure 4-3 is the channel spacing of a high-capacity WDM system, 0.5 nm. As shown, the response of the 7th-order Butterworth is flatter near resonance and has a lower level of crosstalk compared to that for the single-pole QWS Bragg resonator.

The particular choice of one filter over another is dictated by the system constraints and requirements.

An even more complicated Bragg-grating-based optical filter is the integrated resonant channel-dropping filter (CDF), first proposed by Haus *et al.* [13] in 1992. The integrated resonant CDF is shown schematically in Figure 4-4. The theory of device operation is well-established and is described by Haus [13,17,101] and Damask [102–108]. The function of the device is to spatially separate, or "drop", just one channel from a WDM bit stream without terminating or otherwise disturbing the other channels in the bit stream. The CDF is constructed by weakly coupling two high-finesse QWS Bragg resonators to a central rib waveguide located between the two resonators. The central waveguide, the "bus", carries the WDM bit stream. Only that channel in the bit stream that excites, or is resonant with, the two side-coupled QWS Bragg resonators is removed from the bus into the left-most guide. The other channels do not excite the resonators and therefore travel through undisturbed. Figure 4-4 also shows the transmitted power as a function of normalized frequency δ/κ, where δ is the detuning away from the Bragg frequency and κ is the grating strength, for both the leftmost and middle guides. As shown, the signal guide contains the "dropped" channel at the Bragg frequency and, consequently, there is a notch in the transmission spectrum of the middle guide at the same frequency. The action of dropping a signal from the bit stream can be reversed to realize a narrow-band channel-adding filter. The ability to either add or drop a single narrow-band channel from a WDM bit stream augments the repertoire of functions that are available to the WDM system architect.

The basic component of the single-pole, the multiple-pole and the channel-dropping filter is the QWS Bragg resonator. The grating design involves the choice of both the grating length and the grating depth. To this end, extensive computer models have been developed [102,105,107,108]. Once a grating design exists, nanofabrication techniques must be employed to realize the design in a real, physical device. The

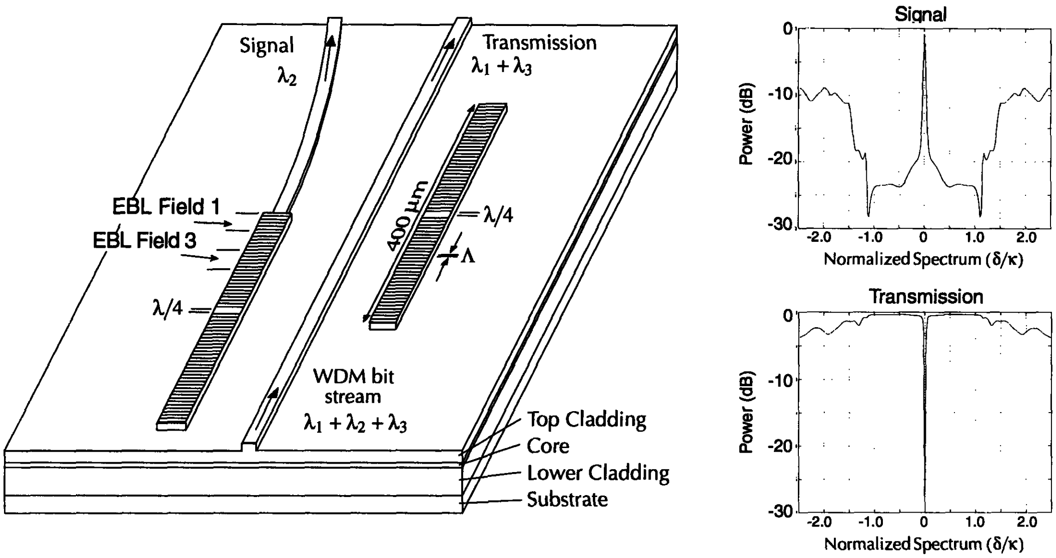

Figure 4-4: Schematic of the integrated resonant channel-dropping filter. The plots on the right show the transmitted power of the leftmost and middle guides as a function of normalized frequency. The leftmost guide contains the extracted signal from the WDM bit stream and the central guide has a corresponding notch.

structural requirements for the QWS Bragg resonators are stringent. In particular, the grating patterns are typically at least 400 μm-long, must maintain spatial coherence to better than $\lambda/150$ [103,106], must be localized to reside on top of the specified waveguides, and have a period of ~240 nm or ~510 nm for InP- or silica-based materials, respectively. Furthermore, there must be flexibility in the choice of the grating period to allow for the monolithic integration of devices of different Bragg frequencies.

Our approach to fabricate Bragg-grating-based optical filters is a mixed lithography approach. The rib waveguides are patterned with optical lithography (level 1) and reactive-ion-etching (RIE). The grating corrugation patterns are written with a vector scan EBL system[1] [109] on an x-ray mask (level 2) using SPLEBL, as described in Chapter 2. These grating patterns are then transferred with XRL and RIE into the rib waveguides. Figure 4-5 illustrates the two levels. Both cross-type and

---

[1] the IBM VS-6 system in Yorktown Heights, NY.

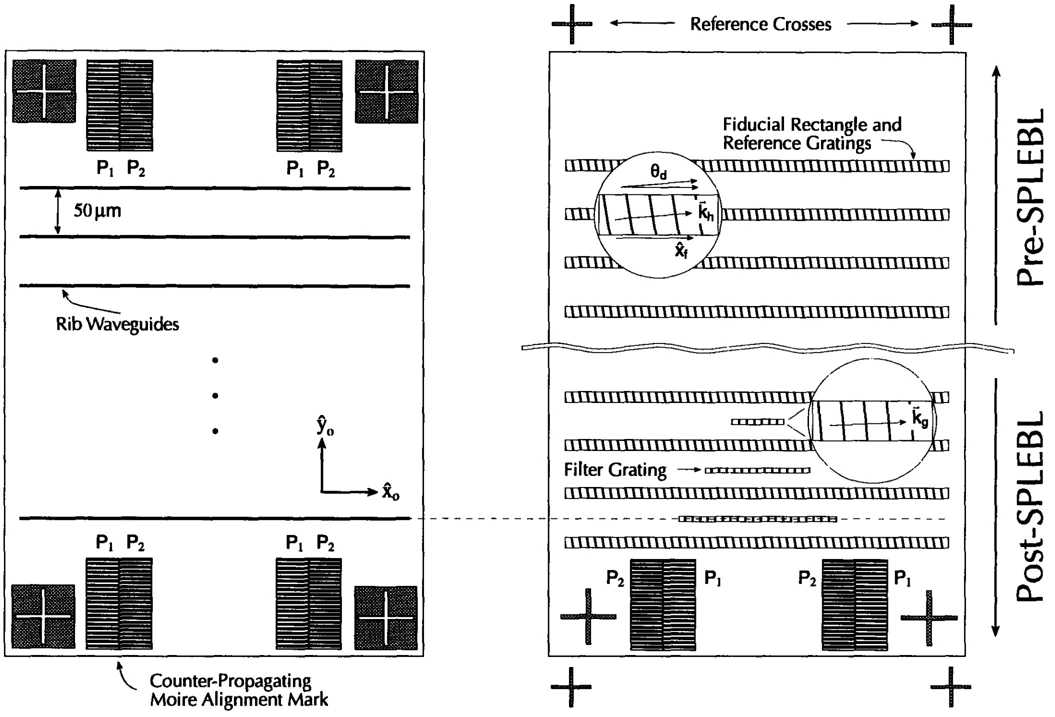

(*a*) (*b*)

Figure 4-5: Depiction of (*a*) the rib waveguide optical mask (level 1) and (*b*) the filter grating x-ray mask (level 2) before and after patterning with SPLEBL. The upper part of (*b*) shows the fiducial grating patterns alone, while the lower part of (*b*) includes the e-beam-defined filter grating patterns, complimentary alignment crosses and counterpropagating moiré marks of periods p_1 and p_2.

interferometric broad-band imaging (IBBI) moiré alignment marks [110] are used to achieve the requisite overlay of the two mask levels. In this chapter the techniques to transfer the grating patterns on the x-ray mask to the waveguide substrate are described. These techniques are equally-applicable to the fabrication of any of the three types of filters mentioned above. To demonstrate these techniques, high-quality QWS Bragg resonators in a silica-on-silicon materials system were fabricated and tested. Preliminary results on multiple-pole filters have also been obtained.

It is worth noting that filters similar to those described above were demonstrated in the microwave regime over forty years ago using metallic cavity resonators [111,112].

coefficients are A_m and A_{-m}.

To solve (3.6) and (3.7), solutions of the form $\exp(\gamma z)$ are assumed. For perfect antireflection (AR) coated facets the boundary conditions are $A(-L/2) = B(L/2) = 0$. These yield the eigenvalue equation [56]

$$\pm j\kappa \sinh(\gamma L) = \gamma \tag{3.10}$$

and the dispersion relation

$$(\alpha - j\delta)^2 = \gamma^2 - \kappa^2 \tag{3.11}$$

where

$$\kappa^2 = \kappa_{ab}\kappa_{ba}. \tag{3.12}$$

For a given coupling coefficient κ (and cavity length L), (3.10) gives an eigenvalue γ and (3.11) gives a corresponding threshold gain constant α and resonant frequency (determined from δ).

In general, the coupling coefficient is complex-valued and can be expressed as

$$\kappa = \kappa_r + j\kappa_i \tag{3.13}$$

where κ_r and κ_i are the real and imaginary components, respectively, of the coupling coefficient.

3.1.1 Index coupling

For the above example, we considered an index modulation. This dictates that $A_m(x) = A^*_{-m}(x)$ since n_1 is a real quantity. The unperturbed fields $\phi_a(x)$ and $\phi_b(x)$ are usually calculated ignoring any gain or loss which may exist in the waveguide, so these quantities are real, as is the propagation constant β. Therefore, we

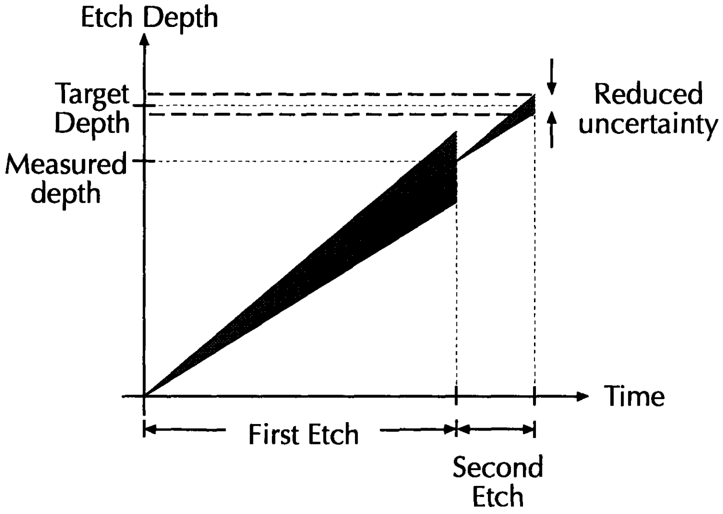

Figure 4-8: Plot illustrating two-step RIE process. An etch depth measurement is performed after the first etch-step followed by a second etch-step. The final uncertainty in the total etch depth is reduced by a factor of approximately the ratio of the second etch-step time to the total etch time.

depths determined by the precision with which the etch rate has been characterized. The resist from a diagnostic pattern is then selectively-removed with RIE (Plasma Therm 7000, 10 mtorr, 50 V, 15 sccm O_2), and the etch depth after the first etch-step is measured. The RIE conditions for this selective-removal step are chosen such that there is minimal sputtering of the underlying oxide (due to an overetch of the resist) since significant sputtering compromises the accuracy of the etch depth measurement. 7000, 10 mtorr, 200 V, 25 sccm He, 15 sccm CF_4) is performed. Care must be taken to reduce sputtering when selectively-removing the resist after the first etch-step. When compared to a single-step RIE procedure, the uncertainty in the final etch depth obtained using this method is reduced by a factor of approximately the ratio of the second etch-step etch time to the total etch time. In this way etch depths of 151±2 nm and 150±2 nm as measured by ellipsometry and profilometry, respectively, were achieved for a target etch depth of 150 nm.

In the more recent past, approximately twenty years ago, filters utilizing surface acoustic waves (SAW) have been demonstrated [16,100]. For SAW devices the wavelengths of interest are approximately two orders of magnitude larger (several 10's of μm's) and for this reason the patterning of the filter gratings was achieved with conventional technology - that is, optical lithography. With the development of SPLEBL, which can meet the requirements of both resolution and spatial phase coherence, equivalent optical filters can be demonstrated.

4.1 Fabrication Approach

The rib waveguide substrates are comprised of three successive film depositions onto high-resistivity, 10 cm-diameter silicon wafers: 3.9 μm-thick wet SiO_2 for the lower cladding; 154 nm-thick LPCVD Si_3N_4 for the core, subsequently annealed for 2 hrs. at 1000°C; and 340 nm LPCVD low-temperature SiO_2 (LTO) for the upper cladding, subsequently annealed for 2 hrs. at 950°C, which reduced the thickness to 315 nm. Rib waveguides are patterned in the top cladding of these substrates using optical lithography and RIE, after which the grating patterns are transferred into the rib waveguides by XRL and RIE. Various aspects of the grating pattern transfer process are described in the following sections.

4.1.1 Self-aligned process

A self-aligned process, so-called because it restricts the grating to lie solely on top of the rib waveguide, was developed to transfer the grating patterns on the x-ray mask onto the rib waveguide. The virtue of this method is the wide lateral alignment tolerance it affords. The process steps are shown schematically in Figure 4-6. First, the rib waveguides are aligned to the $(0\bar{1}\bar{1})$ cleavage plane of the silicon crystal and patterned in 1.3 μm of photoresist (Figure 4-6(a)). Next, the rib waveguides are reactive-ion-etched (Plasma Therm 7000, 10 mtorr, 200 V, 25 sccm He, 15 sccm CF_4)

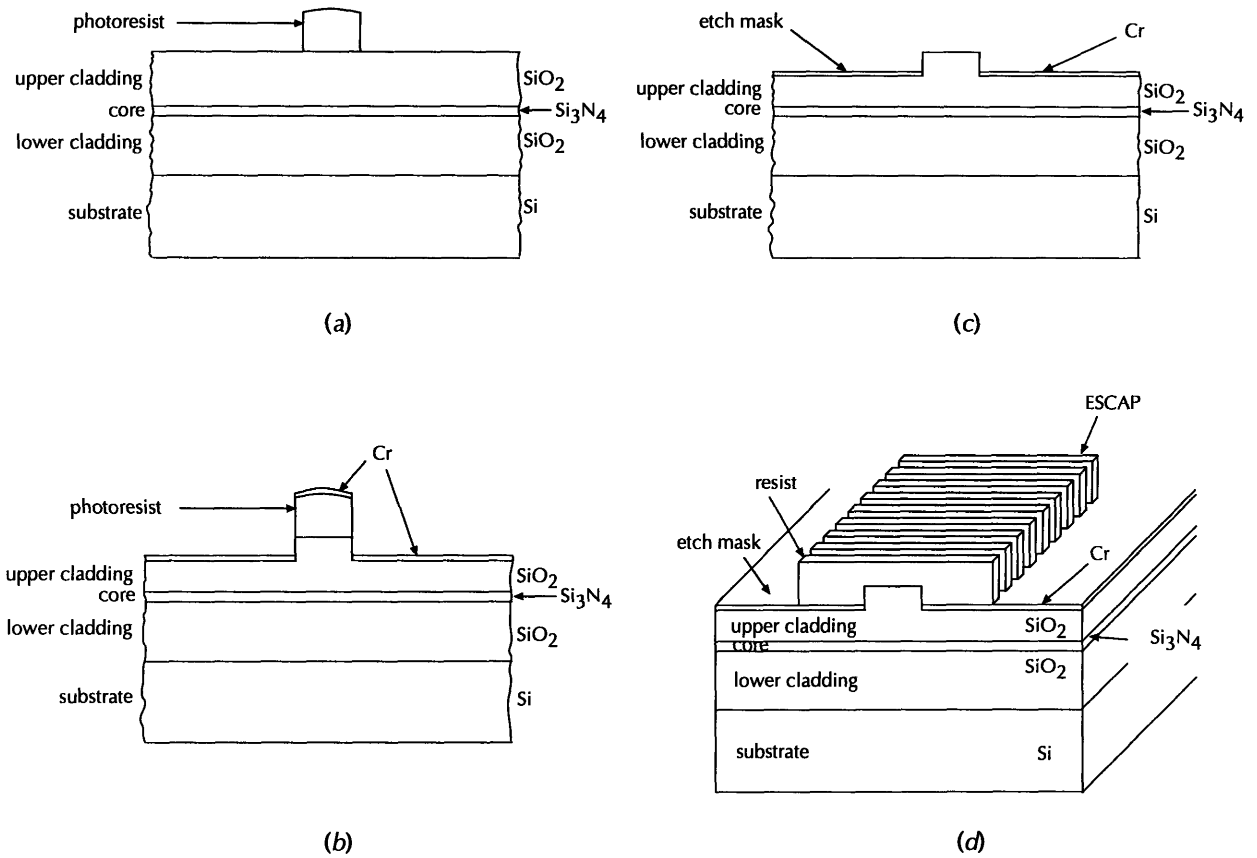

Figure 4-6: Self-aligned process steps: (*a*) pattern rib waveguides, (*b*) pattern transfer into upper cladding and evaporate etch mask, (*c*) liftoff etch mask and (*d*) spin on resist and pattern Bragg grating.

to the target etch depth, typically ~200-220 nm, and fifty nanometers of chromium (Cr) is evaporated over the wafer (Figure 4-6(*b*)). A liftoff of the Cr is then performed (Figure 4-6(*c*)). At this point, only the top faces of the rib waveguides are not covered with Cr. An adhesion promoter, hexamethyldisilizane, is then spun-on followed by 400 nm of the "environmentally-stable chemically-amplified photoresist", ESCAP [113], which is baked on a vacuum hotplate at 150 °C for 90 sec.

The rotational alignment between the x-ray mask and the rib waveguide patterns uses aligment crosses within the chip area. Since they are separated by approximately 4 mm and can be superimposed to within 1 μm by viewing in a microscope, the angular misalignment is within 0.03°. Lateral alignment is not critical in the self-aligned process because the written gratings are much wider (5 μm) than the rib waveguides (2 μm). After exposure with the Cu_L x-ray line (1.32 nm) the resist is postbaked on a vacuum hotplate at 142 °C for 40 sec and developed in Microposit MF321 (Figure 4-6(*d*)). RIE (Plasma Therm 7000, 10 mtorr, 200 V, 25 sccm He, 15 sccm CF_4) is then performed, transferring the gratings into the rib waveguide to the target depth, but not into the surrounding substrate which was covered with Cr. Finally, the ESCAP and Cr are removed. Figure 4-7 shows a schematic drawing along with a scanning electron micrograph of a filter grating ($\Lambda = 511$ nm) etched into a 2 μm-wide rib waveguide using the self-aligned process.

4.1.2 Step-and-repeat XRL

The high sensitivity and stability of the ESCAP allowed a step-and-repeat procedure to be implemented as follows. An x-ray exposure was performed on the optical waveguide substrate using the self-aligned process described in the previous section. An aperture sized 7 X 7 mm was used during the x-ray exposure to prevent the exposure of adjacent dice. After this first x-ray exposure, two additional mask-to-substrate alignments and x-ray exposures were performed, after which the ESCAP is postbaked on a vacuum hotplate at 142°C for 40 sec. All three of the exposed dice were then developed simultaneously in Microposit MF321. Although the first die experienced an 8 hr. delay between x-ray exposure and post-exposure bake, the resist profiles of this die were comparable to those of the other two.

After development, the Bragg gratings were transferred into the top SiO_2 cladding layer by RIE (Plasma Therm 7000, 10 mtorr, 200 V, 25 sccm He, 15 sccm CF_4). At this point the ESCAP was stripped in an oxygen plasma and the substrate cleaned in a solution of H_2O:H_2O_2:NH_4OH (5:1:1) at 80°C for 10 min. Once again, HMDS was spun-on followed by a 400 nm-thick layer of ESCAP, and another series of three alignment and exposures performed. By repeating this process, 9 separate dice (3 sets

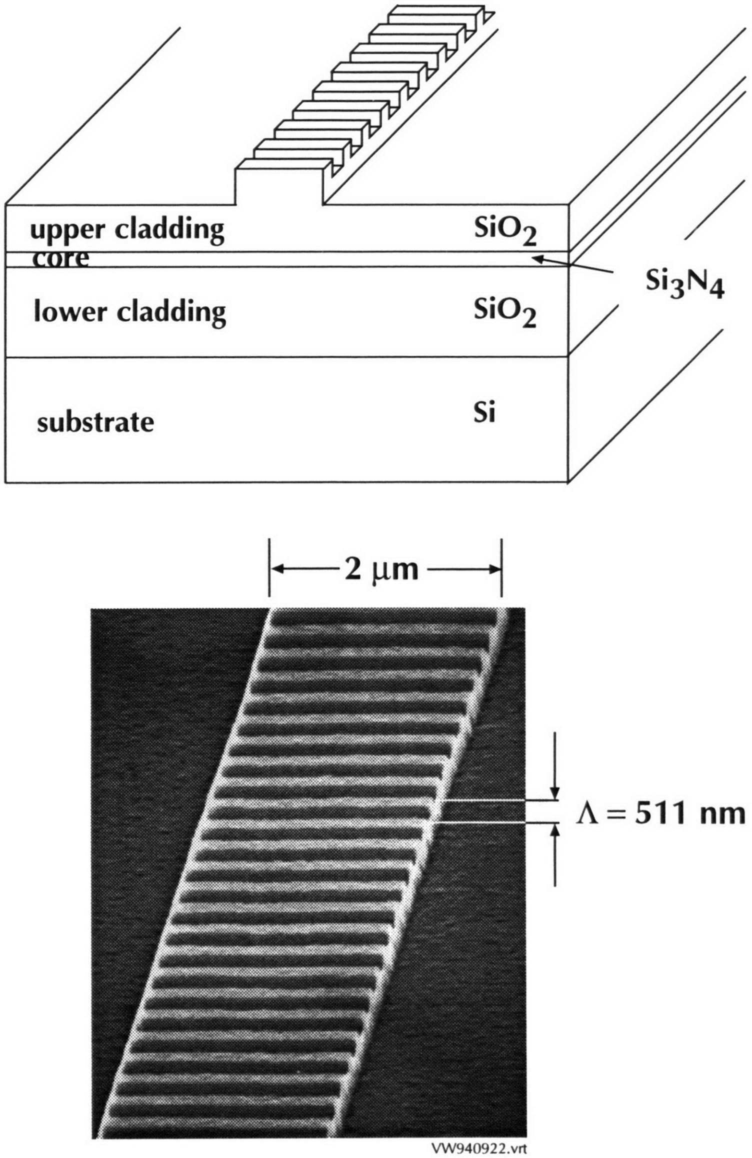

Figure 4-7: Schematic and scanning electron micrograph of a self-aligned grating (Λ = 511 nm) etched into a rib waveguide of width 2 μm..

of 3) were successfully step-and-repeated on the substrate. After the pattern transfer of the last set of dice, the ESCAP was stripped in an oxygen plasma and the Cr was stripped by wet-chemical etching. The multiplicity of dice on one substrate allows one to etch each die to a different grating depth. In this way, the grating strength can be varied across a single wafer which allows for a more accurate analysis of the effects of the grating strength on device performance.

4.1.3 Two-Step RIE

The gratings for a particular filter are designed for a given grating strength, κ, which is determined by the grating depth (for a given waveguide geometry). The designated κ-value is dictated by the constraints of the WDM system such as channel density and crosstalk. Depending on the particular type of filter, errors in κ, $\Delta\kappa$, have different effects. For a single-pole filter, $\Delta\kappa > 0$ (< 0) results in a decreased (increased) resonance linewidth and an increased (decreased) stopband width. The Lorentzian shape of the resonance, however, is preserved. For a multiple-pole filter, errors in κ have more complicated effects. $\Delta\kappa > 0$ results in under-coupling of the resonators, which in turn narrows the filter response and decreases the rate of roll-off away from the center resonance. $\Delta\kappa < 0$ results in over-coupling of the resonators, which in turn widens the filter response and and increases the ripple in the passband. For a CDF, an error in κ will among other things affect the inter-channel crosstalk which, in turn, affects the channel capacity of the WDM system. In particular, $\Delta\kappa > 0$ decreases the level of crosstalk, and vice versa. Clearly, κ and therefore the grating etch depth must be accurately-controlled.

For increased grating etch depth control, a two-step RIE procedure was used. A plot illustrating the basic concept is shown in Figure 4-8. Based on the etch rate of monitor samples, the first etch-step (Plasma Therm 7000, 10 mtorr, 200 V, 25 sccm He, 15 sccm CF_4) is carried out to achieve an etch depth slightly less than the target etch depth. The etch depth achieved after this first etch-step lies within a range of

Field oxide (lower cladding) index	1.45
Silicon nitride (core) index	1.97
LTO (upper cladding) index	1.45
Effective index (n_{eff})	1.493
Group index (n_g)	1.72
Waveguide loss	0.53 dB/cm

Table 4.1: Summary of device parameters for QWS Bragg resonators.

4.2 Single-Pole Filters - Results

The first generation of Bragg-grating-based optical filters studied were single-pole filters. SPLEBL was used to pattern QWS Bragg resonator gratings as well as uniform gratings (for measurements of the grating strength, κ) on an x-ray mask, as described in Section 2.4. These grating patterns were then transferred onto a rib waveguide substrate using the techniques described above. The resonator lengths were varied between ~450 μm (7 EBL fields) to ~850 μm (13 EBL fields). Furthermore, grating patterns were written at three different grating periods - 509, 513 and 517 nm. The rib waveguide width and height were 2.0 μm and 0.2 μm, respectively. The grating depth, grating duty cycle and grating strength were 118 nm, 0.54 and 73 cm^{-1}, respectively. The remaining device parameters are summarized in Table 4.1.

Figure 4-9 shows the measured transmission response of 6 QWS Bragg resonators, ranging in length from ~325 μm (5 EBL fields) to ~1100 μm (17 EBL fields). The center wavelength is these filters is at 1535.4 nm. There are several key points to note. First, a clear resonance is observed in all cases. Second, the linewidth of these resonances decrease or equivalently the resonator Q-values increases for increasing lengths. The resonator Q-values range from 3,000 to 50,000. The decreasing linewidths as expected are due to the increasing reflectivities of the Bragg gratings. Another consequence of the increased grating reflectivity is the decreased in-band baseline level, which saturates at ~40 dB due to the measurement limit of the spectrometer. Finally, the amplitude of the resonance decreases. This decrease, however, is not directly attributable to material loss. Rather, it is due to a measurement limi-

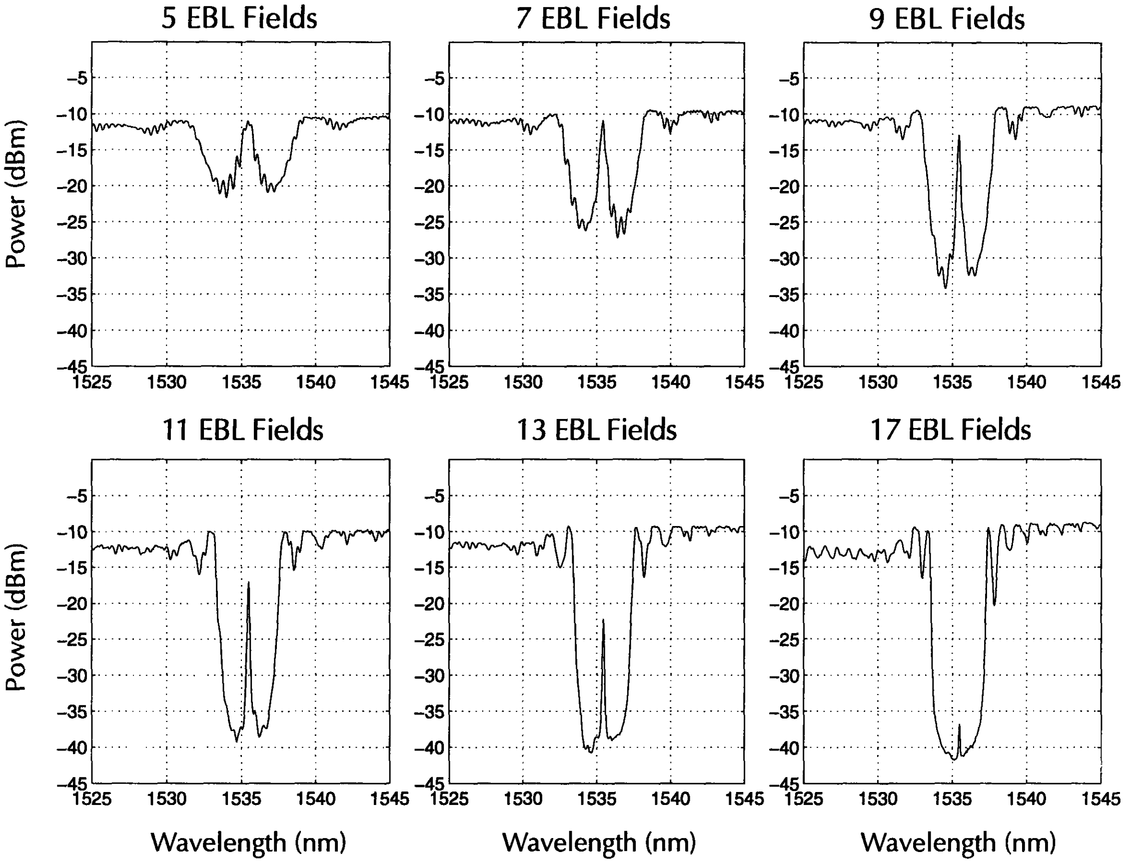

Figure 4-9: Transmission response for 6 QWS Bragg resonators of different lengths, ranging from ~325 μm (5 EBL fields) to ~1100 μm (17 EBL fields).

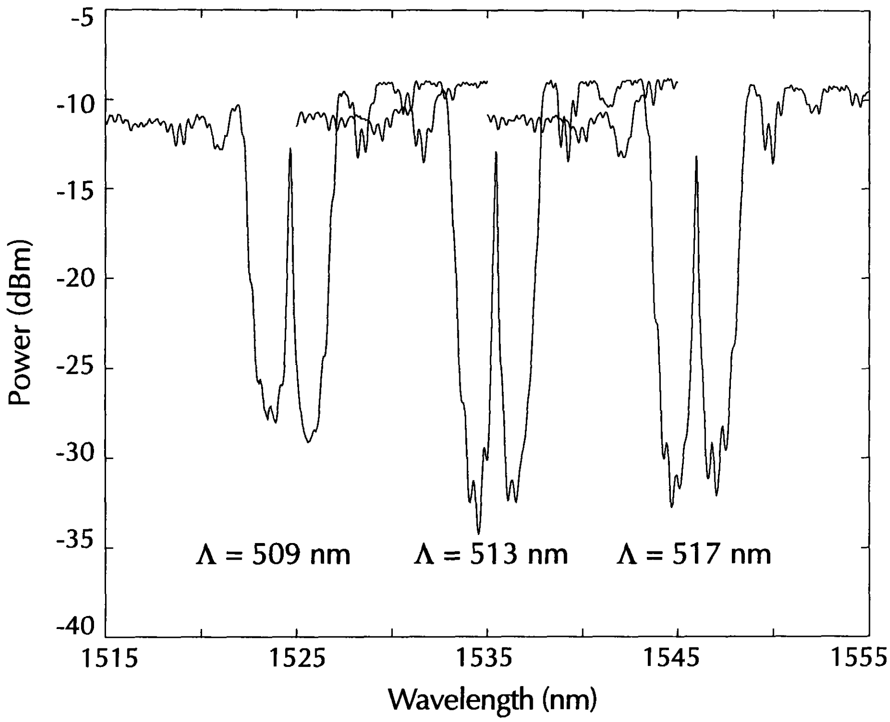

Figure 4-10: Transmission response of QWS Bragg resonators of 3 different periods - 509, 513 and 517 nm.

tation of the spectrometer. The filter function of the spectrometer averages the peak with the immediately surrounding roll-off of the resonance, resulting in an overall decrease in the peak intensity.

Figure 4-10 plots the transmission response of QWS Bragg resonators at the 3 different periods of 509, 513 and 517 nm. A clear resonance is observed in each case. The center wavelengths are 1524.6, 1535.4 and 1546.0 nm. The ability to pattern Bragg gratings at various periods on the same substrate is essential for monolithic integration of grating-based optical filters.

Figure 4-11 shows the transmission response of a QWS Bragg resonator (9 EBL fields long). The resonance is well-centered within the stopband and has a full-width

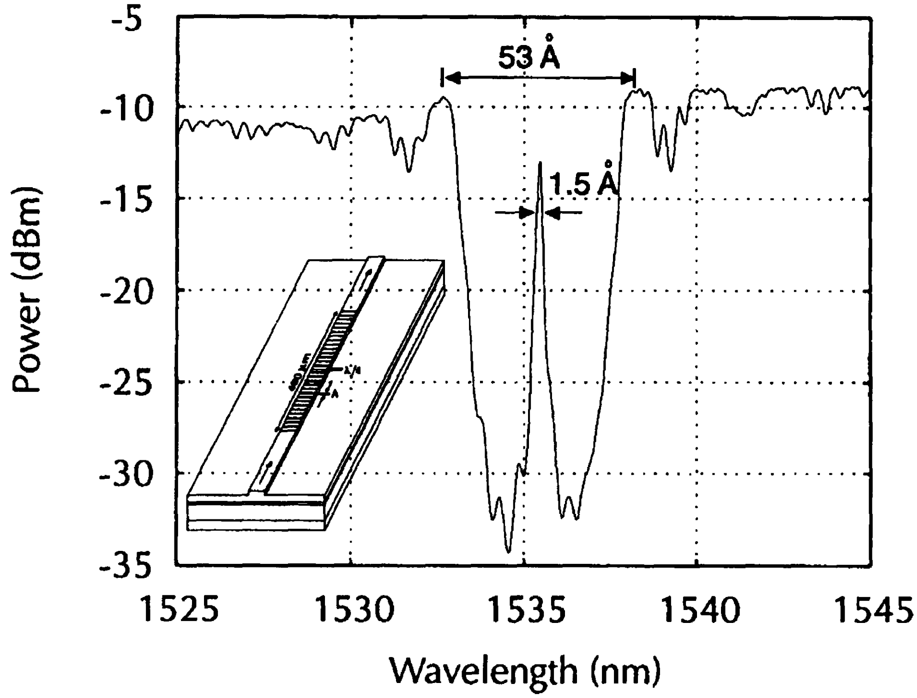

Figure 4-11: Transmission response of a QWS Bragg resonator which spans 9 EBL fields. The resonance linewidth and the stopband width are 1.5 *Å* and 53 *Å*, respectively.

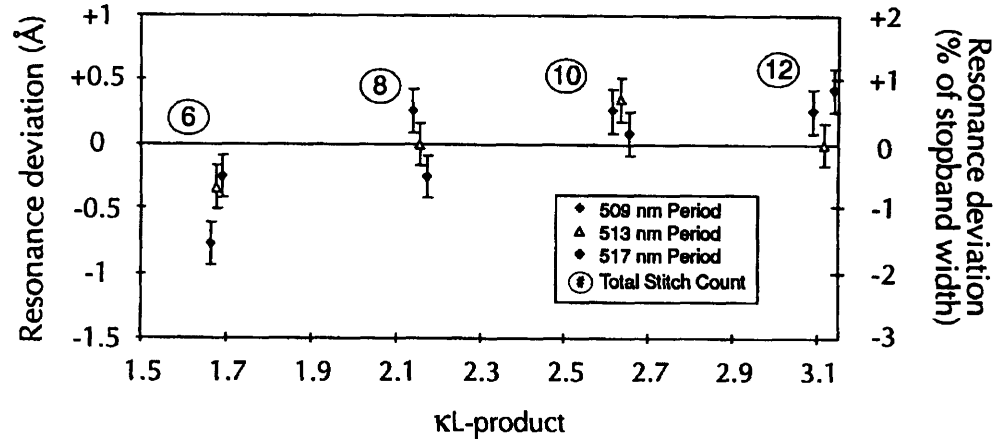

Figure 4-12: Plot showing the resonance deviation of 12 QWS Bragg resonators of 4 different κL-products and 3 different periods. The deviations are all less than 2% of the stopband width suggesting that the Bragg gratings have good spatial coherence.

at half-maximum of 1.5 Å. The stopband width measures 53 Å. The high-frequency fringes in the response are due to Fabry-Perot reflections between the substrate facets and the Bragg gratings.

The reproducibility of resonance placement is an important consideration for the incorporation of Bragg-grating-based filters in WDM systems. The precision of resonance placement rests largely on the fidelity of the patterned gratings, in particular, the spatial coherence. Figure 4-12 shows the resonance deviation from a designated center wavelength of 12 QWS Bragg resonators of different κL-products and grating periods. As shown, the deviations are all less than 1 Å which corresponds to less than 2% of the stopband width. Such small deviations suggest Bragg gratings with good spatial-phase coherence. Recently, however, a direct measurement of the stitching errors of the gratings defined by SPLEBL was made. The results of this measurement indicate stitching errors which are significantly larger than expected based on both the measured optical responses and the theoretical models which have been developed. It is speculated that the larger-than-expected stitching errors were introduced through an error in the field correction software during the process of phase-locking. Further work needs to be done to directly correlate the grating coherence to the measured optical responses.

4.3 Multiple-Pole Filters - Results

The second generation of Bragg-grating-based optical filters investigated were multiple-pole filters. As for the single-pole filters, SPLEBL was used to define the grating patterns onto an x-ray mask, and the patterns were transferred onto rib waveguide substrates as decribed above. Gaussian, Butterworth and Chebyshev filters up to 9-th order were designed and fabricated. Details of the design and grating layout are described in reference [114]. Preliminary results have been obtained for the Gaussian filters. Figure 4-13 shows the transmission response of 1st-, 3rd-, 5th- and 7th-order Gaussian filters. In all cases a clear resonance and stopband are observed. The observed resonance linewidth and filter roll-off, however, is limited by the 0.1 nm resolution limit of the spectrometer. Furthermore, the response on the long-wavelength side of the stopband is indicative of a Gaussian multiple-pole filter response. Presently, further measurements of the other multiple-pole filters are being performed. Finally, as in the case of the single-pole filter gratings, the measured stitching errors of the SPLEBL-defined gratings indicate larger-than-expected stitching errors. Possible solutions to remedy this situation are currently being investigated.

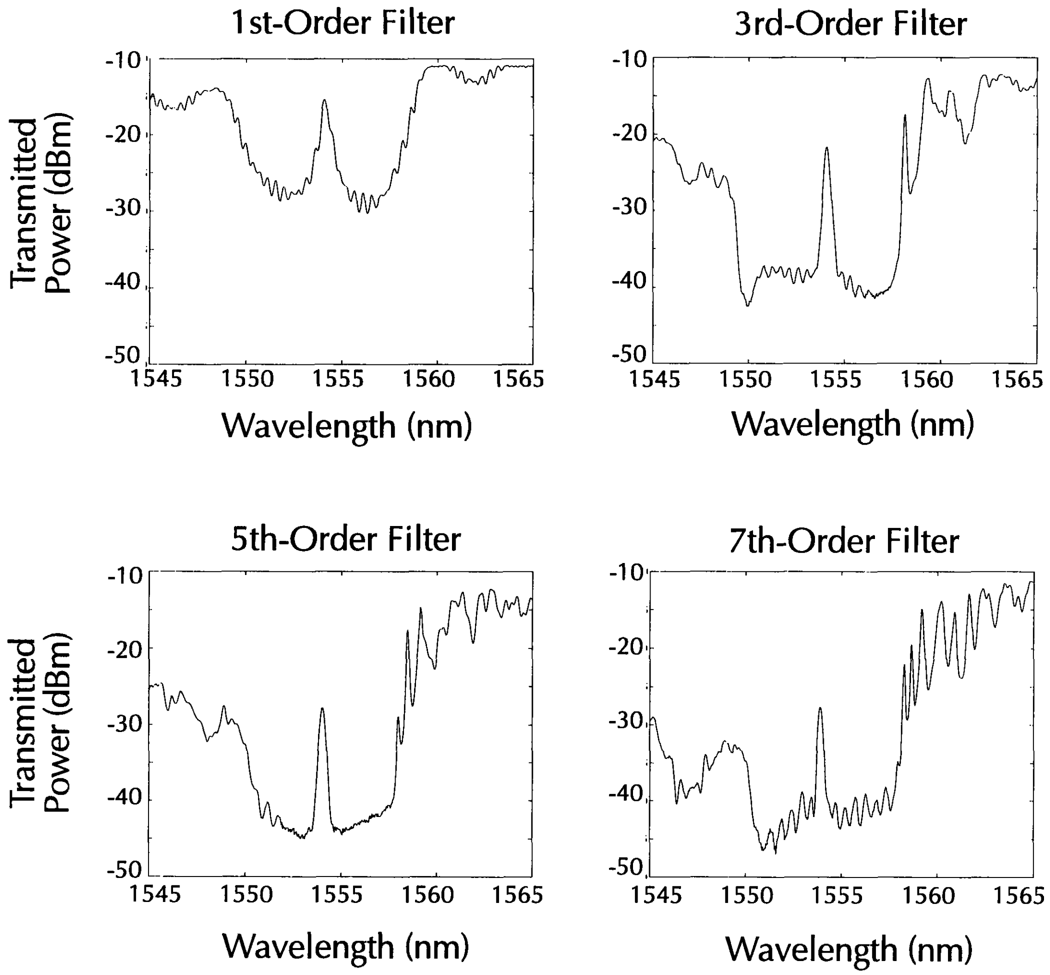

Figure 4-13: Transmission response of 1st-, 3rd-, 5th- and 7th-order Gaussian filters. A clear resonance and stopband is observed in all cases. The resonance linewidth and fall-off, however, is limited by the 0.1 nm resolution limit of the spectrometer. The side-lobes on the long-wavelength side of the stopband are indicative of a Gaussian multiple-pole filter response.

Chapter 5

Summary and Future Research

It is clear that optical communications systems will play a key role in future information technology. Such systems have emerged as the method of choice for handling the high data capacities required in applications such as interactive video and high-definition television. Among the various system architectures, wavelength-division-multiplexed (WDM) architectures appear to be one of the most promising, offering a potential information capacity exceeding 1 THz! In a WDM system the available optical frequency bandwidth is filled with many closely-spaced signals or channels. The ensemble of channels forms a multi-frequency 'bit stream'. Optimal WDM system performance is achieved when this 'bit stream' is as dense (i.e. as closely-spaced) as possible within the limitations imposed by inter-channel crosstalk. Given this fact a reliable and flexible means of both forming and resolving the 'bit stream' is required. The 'bit stream' can be formed with a combination of laser transmitters and multiplexers and resolved with demultiplexers. The task, therefore, rests on the design and fabrication of these system components. The phenomenon of distributed feedback (DFB) or equivalently Bragg reflection, which provides the narrow-band frequency-selectivity required in densely-packed WDM systems, is well-suited for the development of high-performance lasers and Bragg-grating-based optical filters, which serve as multiplexers and demultiplexers.

The goal of this research has been the development of nanofabrication technology for the realization of DFB lasers and Bragg-grating-based optical filters for optical communications. The operation of these devices demands that the grating nanostructures preserve the coherence of the optical waves with which the nanostructures interact. The most flexible means of defining the requisite grating patterns is with electron-beam lithography (EBL). A shortcoming of EBL, however, is the phase-coherence-destroying stitching errors which occur in patterns spanning many EBL fields, such as the grating patterns in DFB lasers and Bragg-grating-based optical filters.[1] This fact demands the use of spatial-phase-locked (SPL) EBL, a new paradigm of EBL which has demonstrated a standard deviation of phase-locking repeatability of less than 1 nm [22], for defining the grating patterns. A second shortcoming of EBL is the low throughput of the writing process. An alternative approach utilizes x-ray lithography (XRL) for the pattern transfer of the grating patterns. In this work our approach is a mixed-lithography strategy. SPLEBL is used to define the device grating patterns onto a SiN_x x-ray mask. XRL is then used to transfer these patterns onto a waveguide substrate, which is patterned using optical lithography. We believe this represents the most powerful and flexible fabrication approach towards the goal of obtaining high-yield, high-performance and high-volume production of DFB devices for optical communications.

The basic concept of SPLEBL is that a fiducial grating or grid pattern which has the property of long-range spatial phase coherence is used as a reference for the electron-beam during the writing process. This fiducial pattern, which resides on the substrate surface, provides direct feedback on the position of the electron-beam with respect to the substrate, unlike other commonly-used secondary referencing techniques. In the initial implementation of SPLEBL a segmented grating was used.

---

[1] Distortions within a single EBL field can also destroy the phase-coherence of a grating. This so-called *intra*-field distortion, however, can be minimized with the proper calibration of the position digital-to-analog converters [21] and the use of small field sizes to eliminate the component of the distortion due to aberrations in the electron optics.

Techniques based on holographic lithography have been developed for fabricating segmented grating x-ray masks as well as uniform grating and uniform grid x-ray masks. SPLEBL was used to pattern the segmented grating x-ray masks with both DFB and Bragg-grating-based optical filter patterns. After these masks are fabricated, pattern transfer techniques must be employed to realize the grating nanostructures. Two types of devices, each with its own fabrication sequence, were investigated: (*i*) the laterally-coupled (LC) DFB laser and (*ii*) optical filters based on quarter-wave-shifted (QWS) Bragg resonators.

The fabrication of conventional DFB lasers involves an epitaxial regrowth step. The initial epitaxial growth of the laser material is interrupted at which point a grating is patterned on the substrate. The patterned substrate is then inserted back into the growth chamber where the epitaxial growth is resumed. This regrowth process increases the process complexity and consequently decreases the device yield. A LC-DFB laser is one in which lateral gratings are patterned after the completion of both the epitaxial growth of the laser material and the formation of a ridge-waveguide. In this way the grating fabrication can be decoupled from the epitaxy step.

Computer simulations based on the imaginary-distance beam-propagation method have been performed to validate the feasibility of the LC-DFB structure. Both the conventional vertical-mesa structure and a recently proposed reverse-mesa structure were analyzed. It was shown that by proper design of both the waveguide and the grating parameters lateral coupling can provide a level of feedback comparable to existing DFB laser geometries. This fact along with the simplified processing of LC-DFB lasers due to the lack of an epitaxial regrowth step makes such lasers attractive candidates for WDM applications. The primary requirement to maximize the optical feedback is that the lateral gratings reside as close to the ridge sidewall as possible. The primary obstacle to the lateral grating fabrication is the non-uniformity of spun-on resist on substrates with deep topography (i.e. ≥ 1 μm) such as that on a typical ridge waveguide substrate. To this end, a novel process utilizing ion implantation was proposed and demonstrated to eliminate resist non-uniformity. This process combined with XRL (or any other appropriate lithography technology) and RIE can be straightforwardly applied to the fabrication of lateral gratings for LC-DFB lasers.

With the development of the nanofabrication technology in this thesis, one is poised to apply this technology towards the realization of LC-DFB lasers. Perhaps the best approach is to use SPLEBL to define device gratings at several grating periods where the range of grating periods is chosen to account for uncertainties in values of the effective index. Although vertical-mesa structures have been used in this work, the fabrication techniques are equally-applicable for reverse-mesa structures, which appear to offer improved lateral coupling over vertical-mesa structures. The demonstration of LC-DFB lasers through the combination of XRL with its high process latitude and SPLEBL with its flexibility will have a significant impact on the optical communications community.

Bragg-grating-based optical filters - single-pole, multiple-pole and integrated resonant channel-dropping filters - have also served as motivation for this thesis work. The basic component in all of these devices is the QWS single-pole Bragg resonator. In this work single-pole and multiple-pole filters in a silica-based materials system were investigated. SPLEBL was used to define the Bragg grating patterns and XRL was used to pattern transfer these patterns onto a rib waveguide substrate. A self-aligned process was developed along with a scheme for step-and-repeating the Bragg grating patterns onto multiple dice on a rib waveguide substrate. A two-step reactive-ion-etching process has also been developed for accurate control of the grating etch depth. High-quality QWS Bragg resonators have been fabricated using the above techniques and preliminary results for multiple-pole filters have been obtained. These in-line filters are the first step towards the realization of integrated resonant channel-dropping filters. The single-pole and multiple-pole filter device results described in this thesis lend credence to and validate our fabrication approach. In addition, they represent the first utilization of SPLEBL for device applications. Presently, SPLEBL is being pioneered solely at MIT. Undoubtedly, as the technology of SPLEBL is refined and improved, it will find more widespread use in other research labs and perhaps even industry for future applications requiring phase-coherent nanostructures.

As is the case of the work on the LC-DFB described earlier, there are many paths of future research for Bragg-grating-based optical filters. First, although a stochastic model has been developed to analyze the effects of stitching errors on filter performance, a correlation of this model with experimental results needs to be performed. Another path of investigation is the development of indium phosphide-based optical filters, which can be monolithically-integrated with active devices such as lasers and detectors. Finally, the design and fabrication of single-side-coupled receivers, which address the issue of synchronous coupling, are the next natural progression towards the demonstration of integrated resonant channel-dropping filters.

Bibliography

[1] H. Hillmer, S. Hansmann, and H. Burkhard, "1.53 μm InGaAsP-InP first-order $\lambda/4$-shifted distributed feedback lasers with high coupling coefficients," *IEEE J. of Quant. Elec.*, vol. 27, p. 1753, June 1991.

[2] S. Takano, T. Sasaki, H. Yamada, M. Kitamura, and I. Mito, "Sub-MHz spectral linewidth in 1.5 μm separate-confinement-heterostructure (SCH) quantum-well DFB LD's," *Elec. Lett.*, vol. 25, p. 356, Mar. 1989.

[3] B. Borchert, K. David, B. Stegmüller, R. Gessner, M. Beschorner, D. Sacher, and G. Franz, "1.55 μm gain-coupled quantum-well distributed feedback lasers with high single-mode yield and narrow linewidth," *IEEE Photon. Tech. Lett.*, vol. 3, p. 955, Nov. 1991.

[4] M. Okai, S. Sakano, and N. Chinone, "Wide range continuous tunable double-sectioned distributed feedback lasers," in *European Conference on Optical Communications*, p. 122, 1989.

[5] M. Aoki, M. Suzuki, M. Takahashi, H. Sano, T. Ido, T. Kawano, and A. Takai, "High-speed (10 gbit/s) and low-drive voltage (1 V peak-to-peak) InGaAs/InGaAsP MQW electroabsorption modulator integrated DFB laser with semi-insulating buried heterostructure," *Elec. Lett.*, vol. 28, p. 1157, June 1992.

[6] M. Suzuki, H. Tanaka, H. Taga, S. Yamamoto, and Y. Matsushima, "$\lambda/4$-shifted DFB laser/electroabsorption modulator integrated light source for multigigabit transmission," *IEEE J. of Light. Tech.*, vol. 10, p. 90, Jan. 1992.

[7] U. Koren, B. I. Miller, M. B. Young, M. Chien, A. H. Gnauck, P. D. Magill, S. L. Woodward, and C. A. Burrus, "Strained-layer multiple quantum well distributed bragg reflector lasers with a fast monitoring photodiode," *Appl. Phys. Lett.*, vol. 58, p. 1239, Mar. 1991.

[8] C. E. Zah, F. J. Favire, B. Pathak, R. Bhat, C. Caneau, P. S. D. Lin, A. S. Gozdz, N. C. Andreadakis, M. A. Koza, and T. P. Lee, "Monolithic integration of multiwavelength compressive strained multiquantum-well distributed feedback laser array with star coupler and optical amplifiers," *Elec. Lett.*, vol. 28, p. 2361, Dec. 1992.

[9] J. B. D. Soole, A. Scherer, H. P. LeBlanc, N. C. Andreadakis, R. Bhat, and M. A. Koza, "Monolithic InP/InGaAsP/InP grating spectrometer for the 1.48-1.56 μm wavelength range," *Appl. Phys. Lett.*, vol. 58, p. 1949, May 1991.

[10] C. Dragone, "An NXN optical multiplexer using a planar arrangement of two star couplers," *Photon. Tech. Lett.*, vol. 3, p. 813, Sept. 1991.

[11] M. Kuznetsov, "Cascaded coupler Mach-Zender channel dropping filters for wavelength-division multiplexed optical systems," *J. of Light. Tech.*, vol. 12, p. 226, Feb. 1994.

[12] M. Levy, L. Eldada, R. Scarmozzino, J. R. M. Osgood, P. S. D. Lin, and F. Tong, "Fabrication of narrow-band channel-dropping filters," *IEEE Photon. Tech. Lett.*, vol. 4, p. 1378, Dec. 1992.

[13] H. A. Haus and Y. Lai, "Narrow-band optical channel-dropping filter," *J. of Light. Tech.*, vol. 10, no. 1, p. 57, Jan. 1992.

[14] J.-L. Archambault, P. S. J. Russell, S. Barcelos, P. Hua, and L. Reekie, "Grating-frustrated coupler: a novel channel-dropping filter in single-mode optical fiber," *Opt. Lett.*, vol. 19, p. 180, Feb. 1994.

[15] K. Okamoto, K. Takiguchi, and Y. Ohmori, "16 channel optical add/drop multiplexer using silica-based arrayed-waveguide gratings," in *Optical Fiber Communications '95 - Postdeadline Papers*, p. 10, 1995.

[16] H. A. Haus and R. V. Schmidt, "Transmission response of cascaded gratings," *IEEE Trans. on Sonics and Ultra.*, vol. 24, p. 94, Mar. 1977.

[17] H. A. Haus and Y. Lai, "Theory of cascaded quarter wave shifted distributed feedback resonators," *IEEE J. of Quant. Elec.*, vol. 28, p. 205, Jan. 1992.

[18] G. P. Agrawal, J. E. Geusic, and P. J. Anthony, "Distributed feedback lasers with multiple phase-shift regions," *Appl. Phys. Lett.*, vol. 53, p. 178, July 1988.

[19] S. Nilsson, T. Kjellberg, T. Klinga, R. Schatz, J. Wallin, and K. Streubel, "Improved spectral characteristics of MQW-DFB lasers by incorporation of multiple phase-shifts," *J. of Light. Tech.*, vol. 13, p. 434, Mar. 1995.

[20] A. Moel, W. Chu, K. Early, Y.-C. Ku, E. E. Moon, F. Tsai, H. I. Smith, M. L. Schattenburg, C. D. Fung, F. W. Griffith, and L. E. Haas, "Fabrication and characterization of high-flatness mesa-etched silicon nitride x-ray masks," *J. Vac. Sci. Technol. B*, vol. 9, p. 3287, Dec. 1991.

[21] E. H. Anderson, V. Boegli, M. L. Schattenburg, D. P. Kern, and H. I. Smith, "Metrology of electron beam lithography systems using holographically-produced reference samples," *J. Vac. Sci. Technol. B*, vol. 9, p. 3606, Dec. 1991.

[22] J. Ferrera, V. V. Wong, S. Rishton, V. Boegli, E. H. Anderson, D. P. Kern, and H. I. Smith, "Spatial-phase-locked electron-beam lithography: Initial test results," *J. Vac. Sci. Technol. B*, vol. 11, p. 2342, Dec. 1993.

[23] D. L. Spears and H. I. Smith, "High-resolution pattern replication using soft x-rays," *Elec. Lett.*, vol. 8, p. 192, Feb. 1972.

[24] D. C. Flanders, H. I. Smith, H. W. Lehmann, R. Widmer, and D. C. Shaver, "Surface relief structures with linewidths below 2000 Å," *Appl. Phys. Lett.*, vol. 32, no. 2, p. 112, Jan. 1978.

[25] D. C. Flanders and H. I. Smith, "Polyimide membrane x-ray lithography masks - Fabrication and distortion measurements," *J. Vac. Sci. and Technol.*, vol. 15, no. 3, p. 995, May 1978.

[26] A. M. Hawryluk, N. M. Ceglio, R. H. Price, J. Melngailis, and H. I. Smith, "Gold transmission gratings with submicrometer periods and thicknesses >0.5 μm," *J. of Vac. Sci and Technol.*, vol. 19, no. 4, p. 897, Nov. 1981.

[27] E. H. Anderson, C. M. Horowitz, and H. I. Smith, "Holographic lithography with thick photoresist," *Appl. Phys. Lett.*, vol. 43, no. 9, p. 874, Nov. 1983.

[28] E. H. Anderson, *Fabrication and Electromagnetic Applications of Periodic Nanostructures.* PhD thesis, Massachusetts Institute of Technology, 1988.

[29] W. Chu, *Inorganic X-ray Mask Technology for Quantum-Effect Devices.* PhD thesis, Massachusetts Institute of Technology, 1993.

[30] M. L. Schattenburg, I. Tanaka, and H. I. Smith, "Microgap x-ray nanolithography," *Microelectronic Engineering*, vol. 6, p. 273, 1987.

[31] A. Moel, M. L. Schattenburg, J. M. Carter, and H. I. Smith, "Microgap control in x-ray nanolithography," *J. of Vac. Sci. and Technol. B*, vol. 7, p. 1692, Nov. 1989.

[32] M. L. Schattenburg, K. Early, Y.-C. Ku, W. Chu, M. I. Shepard, S.-C. The, H. I. Smith, D. W. Peters, R. D. Frankel, D. R. Kelly, and J. P. Drumheller, "Fabrication and testing of 0.1 μm-linewidth x-ray masks," *J. Vac. Sci. Technol. B*, vol. 8, p. 1604, Dec. 1990.

[33] K. R. Early, *Experimental Characterization and Physical Modeling of Resolution Limits in Proximity Printing X-Ray Lithography.* PhD thesis, Massachusetts Institute of Technology, 1991.

[34] Y.-C. Ku, *Fabrication of Distortion Free X-ray Masks Using Low Stress Tungsten.* PhD thesis, Massachusetts Institute of Technology, 1991.

[35] M. L. Schattenburg, N. A. Polce, H. I. Smith, and R. Stein, "Fabrication of flip-bonded mesa masks for x-ray lithography," *J. of Vac. Sci. and Technol. B*, vol. 11, p. 2906, 1993.

[36] J. M. Carter, unpublished.

[37] M. L. Schattenburg, C. R. Canizares, D. Dewey, K. A. Flanagan, M. A. Hamnett, A. M. Levine, K. S. K. Lum, R. Manikkalingam, T. H. Markert, and H. I. Smith, "Transmission grating spectroscopy and the advanced x-ray astrophysics facility," *Opt. Eng.*, vol. 30, p. 1590, 1991.

[38] R. C. Weast, M. J. Astle, and W. H. Beyer, eds., *CRC Handbook of Chemistry and Physics.* Boca Raton, Florida: CRC Press, Inc., 66th edition ed., 1985.

[39] M. Nakaishi, M. Yamada, and M. Nakamura, "Backside helium cooling of x-ray masks in reactive ion etching processes," in *Proceedings of the 1989 International Symposium on MicroProcess Conference*, (Kobe, Japan), p. 99, 1989.

[40] K. P. Giapis, G. R. Scheller, R. A. Gottscho, W. S. Hobson, and Y. H. Lee, "Microscopic and macroscopic uniformity control in plasma etching," *Appl. Phys. Lett.*, vol. 57, no. 10, p. 983, Sept. 1990.

[41] M. Mondol, H. Li, G. Owen, and H. I. Smith, "Uniform-stress tungsten on x-ray mask membranes via He-backside temperature homogenization," *J. of Vac. Sci. and Technol. B*, vol. 12, no. 6, p. 4024, Nov. 1994.

[42] Enthome-OMI, Inc., Westhaven, CT.

[43] M. Burkhardt, *Fabrication Technology and Measurement of Coupled Quantum Dot Devices.* PhD thesis, Massachusetts Institute of Technology, 1995.

[44] Kenneth Yee, unpublished.

[45] H. I. Smith, S. D. Hector, M. L. Schattenburg, and E. H. Anderson, "A new approach to high fidelity e-beam lithography based on an in-situ global fiducial grid," *J. Vac. Sci. Technol. B*, vol. 9, p. 2992, Dec. 1991.

[46] H. I. Smith, M. L. Schattenburg and E. H. Anderson. U. S. Patent No. 5,136,169, August 1992.

[47] J. Ferrera, "Highly coherent gratings for optoelectronics: An application of spatial-phase-locked electron beam lithography," Master's thesis, Massachusetts Institute of Technology, 1994.

[48] J. M. Carter, D. B. Olster, M. L. Schattenburg, A. Yen, and H. I. Smith, "Large-area, free-standing gratings for atom interferometry produced using holographic lithography," *J. Vac. Sci. Technol. B*, vol. 10, no. 6, p. 2909, Dec. 1992.

[49] K. Utaka, S. Akiba, K. Sakai, and Y. Matsushima, "$\lambda/4$-shifted InGaAsP/InP DFB lasers by simultaneous holographic exposure of positive and negative photoresists," *Elec. Lett.*, vol. 20, p. 1008, Nov. 1984.

[50] M. Shirasaki, H. Soda, S. Yamakoshi, and H. Nakajima, "$\lambda/4$-shifted DFB-LD corrugation formed by a novel spatial phase modulating mask," in *Proceedings of the European Conference on Optical Communications '85*, p. 9999, 1985.

[51] M. Okai, S. Tsuji, M. Hirao, and H. Matsumura, "New high resolution positive and negative photoresist method for $\lambda/4$-shifted DFB lasers," *Elec. Lett.*, vol. 23, p. 370, Apr. 1987.

[52] H. Sugimoto, Y. Abe, T. Matsui, and H. Ogata, "Novel fabrication method of quarter-wave-shifted gratings using ECR-CVD SiN_x films," *Elec. Lett.*, vol. 23, p. 1260, 1987.

[53] M. Okai, S. Tsuji, N. Chinone, and T. Harada, "Novel method to fabricate corrugation for a $\lambda/4$-shifted distributed feedback laser using a grating photomask," *Appl. Phys. Lett.*, vol. 55, p. 415, July 1989.

[54] A. A. Krasnoperova, Z. Chen, E. Difrabrizio, M. Gentili, and F. Cerrina, "A novel technique for high aspect ratio high resolution pattern on membranes," in *Proceedings of the 39th International Conference on Electron, Ion and Photon Beam Technology and Nanofabrication 1995*, June 1995.

[55] T. E. Bell, "Single-frequency semiconductor lasers," *IEEE Spectrum*, vol. 20, p. 43, Dec. 1983.

[56] H. Kogelnik and C. V. Shank, "Coupled-wave theory of distributed feedback lasers," *J. Appl. Phys.*, vol. 43, p. 2327, May 1972.

[57] H. A. Haus, *Waves and Fields in Optoelectronics.* Prentice-Hall, Inc., 1984.

[58] G. P. Agrawal and N. K. Dutta, *Long-Wavelength Semiconductor Lasers.* Van Nostrand Reinhold Company, 1986.

[59] H. A. Haus and C. V. Shank, "Antisymmetric taper of distributed feedback lasers," *J. Quantum Elec.*, vol. 12, p. 532, 1974.

[60] P. Zhou and G. S. Lee, "Mechanism of phase-shifted distributed-feedback laser with linearly chirped grating for stable-mode operation," *J. of Appl. Phys.*, vol. 70, p. 1902, Aug. 1991.

[61] Y. Nakano and K. Tada, "Analysis, design and fabrication of GaAlAs/GaAs DFB lasers with modulated stripe width structure for complete single longitudinal mode oscillation," *IEEE J. of Quant. Elec.*, vol. 24, p. 2017, 1988.

[62] K. Tada, Y. Nakano, and A. Ushirokawa, "Proposal of a distributed feedback laser with nonuniform stripe width for complete single-mode oscillation," *Electron. Lett.*, vol. 20, p. 82, Jan. 1984.

[63] H. Soda, H. Wakao, H. Sudo, T. Tanahashi, and H. Imai, "GaInAsP/InP phase-adjusted distributed feedback lasers with a step-like nonuniform stripe width structure," *Electron. Lett.*, vol. 20, p. 1016, Nov. 1984.

[64] M. Kitamura, M. Yamaguchi, K. Emura, I. Mito, and K. Kobayashi, "Lasing mode and spectral linewidth control by phase tunable distributed feedback lasers with double channel planar buried heterostructure (DFB-DC-PBH LD's)," *IEEE J. of Quant. Elec.*, vol. 21, p. 415, May 1985.

[65] W. Streifer, R. Burnham, and D. Scifres, "Effect of external reflectors on longitudinal modes of distributed feedback lasers," *J. Quantum Elec.*, vol. 11, p. 154, Apr. 1975.

[66] C. H. Henry, "Performance of distributed feedback lasers designed to favor the energy gap mode," *IEEE J. of Quant. Elec.*, vol. 21, p. 1913, Dec. 1985.

[67] W. Streifer, D. R. Scifres, and R. D. Burnham, "Coupled wave analysis of DFB and DBR lasers," *IEEE J. of Quant. Elec.*, vol. 13, p. 134, Apr. 1977.

[68] R. F. Kazarinov and C. H. Henry, "Second-order distributed feedback lasers with mode selection provided by first-order radiation losses," *IEEE J. of Quant. Elec.*, vol. 21, p. 144, Feb. 1985.

[69] T. Makino and J. Glinski, "Effects of radiation loss on the performance of second-order DFB semiconductor lasers," *IEEE J. of Quant. Elec.*, vol. 24, p. 73, Jan. 1988.

[70] Y. Nakano, H.-L. Cao, K. Tada, Y. Luo, M. Dobashi, and H. Hosomatsu, "Absorptive-grating gain-coupled distributed-feedback MQW lasers with low threshold current and high single-longitudinal-mode yield," *Jpn. J. Appl. Phys. - Part 1*, vol. 32, p. 825, Feb. 1993.

[71] Y. Luo, Y. Nakano, K. Tada, T. Inoue, H. Hosomatsu, and H. Iwaoka, "Fabrication and characteristics of gain-coupled distributed feedback semiconductor lasers with a corrugated active layer," *IEEE J. of Quant. Elec.*, vol. 27, p. 1724, June 1991.

[72] Y. Nakano, Y. Luo, and K. Tada, "Facet reflection independent, single longitudinal mode oscillation in a GaAlAs/GaAs DFB laser equipped with gain-coupling mechanism," *Appl. Phys. Lett.*, vol. 55, p. 1606, 1989.

[73] K. David, G. Morthier, P. Vankwikelberge, R. G. Baets, T. Wolf, and B. Borchert, "Gain-coupled DFB lasers versus index-coupled and phase-shifted DFB lasers: A comparison based on spatial hole burning corrected yield," *IEEE J. of Quant. Elec.*, vol. 27, p. 1714, June 1991.

[74] R. G. Baets, K. David, and G. Morthier, "On the distinctive features of gain coupled DFB lasers and DFB lasers with second-order grating," *IEEE J. of Quant. Elec.*, vol. 29, p. 1792, June 1993.

[75] G. Morthier and P. Vankwikelberge, "Improved performance of AR-Coated DFB lasers by the introduction of gain coupling," *IEEE Photon. Tech. Lett.*, vol. 2, p. 170, Mar. 1990.

[76] W. T. Tsang, F. S. Choa, M. C. Wu, Y. K. Chen, R. A. Logan, A. M. Sergent, and C. A. Burrus, "Long-wavelength InGaAsP/InP distributed feedback lasers incorporating gain-coupled mechanism," *IEEE Photon. Tech. Lett.*, vol. 4, p. 212, Mar. 1992.

[77] M. Aoki, T. Tsuchiya, K. Nakahara, M. Komori, K. Uomi, and T. Ohtoshi, "High-power, wide-temperature-range operation of InGaAsP/InP strained-layer MQW lasers with a reverse-mesa ridge-waveguide structure," in *Optical Fiber Communications '95 - Technical Digest*, p. 255, 1995.

[78] L. M. Miller, J. T. Verdeyen, J. J. Coleman, R. P. Bryan, J. J. Alwan, K. J. Beernink, J. S. Hughes, and T. M. Cockerill, "A distributed feedback ridge waveguide quantum well heterostructure laser," *IEEE Photon. Tech. Lett.*, vol. 3, p. 6, Jan. 1991.

[79] M. Korn, T. Korfer, A. Forchel, and P. Roentgen, "First-order distributed feedback gratings (92.5-105 nm period) for GaInP/AlGaInP lasers emitting in the visible range," *J. Vac. Sci. Technol. B*, vol. 8, p. 1404, Nov. 1990.

[80] R. D. Martin, S. Forouhar, S. Keo, R. J. Lang, R. G. Hunsperger, R. Tiberio, and P. F. Chapman, "InGaAs-GaAs-AlGaAs laterally-coupled distributed feedback (LC-DFB) ridge laser diode," *Elec. Lett.*, vol. 30, p. 1058, June 1994.

[81] R. Tiberio, P. F. Chapman, R. D. Martin, S. Forouhar, and R. J. Lang, "Laterally-coupled distributed feedback laser fabricated with electron beam lithography and chemically assisted ion beam etching," *J. Vac. Sci and Technol. B*, vol. 12, p. 3746, Nov. 1994.

[82] Y. Itaya, T. Matsuoka, K. Kuroiwa, and T. Ikegami, "Longitudinal mode behavior of 1.5 μm range GaInAsP/InP distributed feedback lasers," *IEEE J. of Quant. Elec.*, vol. 20, p. 230, Mar. 1984.

[83] F. S. Choa, W. T. Tsang, R. A. Logan, R. P. Gnall, U. Koren, T. L. Koch, C. A. Burrus, M. C. Wu, Y. K. Chen, P. F. Sciortino, A. M. Sergent, and P. J. Corvini, "Very high sidemode-suppression-ratio distributed-bragg-reflector lasers grown by chemical beam epitaxy," *Elec. Lett.*, vol. 28, p. 1001, May 1992.

[84] T. Kjellberg, S. Nilsson, T. Klinga, B. Broberg, and R. Schatz, "Investigation on the spectral characteristics of DFB lasers with different grating configurations made by electron-beam lithography"," *J. of Light. Technol.*, vol. 11, p. 1405, Sept. 1993.

[85] H. Soda, H. Ishikawa, and H. Imai, "Design of DFB lasers for high-power single-mode operation," *Elec. Lett.*, vol. 22, p. 1047, 1986.

[86] S. Ogita, Y. Kotaki, M. Matsuda, Y. Kuwahara, and H. Ishikawa, "Long-cavity multiple-phase-shift distributed feedback laser diode for linewidth narrowing," *J. of Light. Tech.*, vol. 8, p. 1596, Oct. 1990.

[87] T. Kimura and A. Sugimura, "Linewidth reduction by coupled phase-shift distributed feedback lasers," *Elec. Lett.*, vol. 23, no. 19, p. 1014, Sept. 1987.

[88] J. E. A. Whiteaway, B. Garrett, G. H. B. Thompson, A. J. Collar, C. J. Armistead, and M. J. Fice, "The static and dynamic characteristics of single and multiple phase-shifted DFB laser structures," *IEEE J. of Quant. Elec.*, vol. 28, p. 1277, May 1992.

[89] K. Handa, S. T. Peng, and T. Tamir, "Improved perturbation analysis of dielectric gratings," *Appl. Phys.*, vol. 5, p. 325, 1975.

[90] S. Jüngling and J. C. Chen, "A study and optimization of eigenmode calculations using imaginary-distance beam-propagation method," *IEEE J. of Quant. Elec.*, vol. 30, p. 2098, Sept. 1994.

[91] C. E. Zah, R. Bhat, T. P. Lee, Z. Wang, D. Darby, D. C. Flanders, and J. J. Hsieh, "Recent progress on uncooled 1.3-μm lasers for loop applications," in *Optical Fiber Communications '95 - Technical Digest*, p. 251, 1995.

[92] Z. Wang, D. B. Darby, P. Whitney, R. Panock, and D. C. Flanders, "High-power, high-speed, low-noise operation of uniformly p-doped 1550-nm InGaAlAs compressively strained MQW ridge-waveguide lasers," in *Optical Fiber Communications '95 - Technical Digest*, p. 252, 1995.

[93] J. P. Biersack and L. G. Haggmark, "A Monte Carlo computer program for the transport of energetic ions in amorphous targets," *Nucl. Instr. and Meth.*, vol. 174, p. 257, 1980.

[94] I. Adesida and L. Karapiperis, "The range of light ions in polymeric resists," *J. of Appl. Phys.*, vol. 56, no. 6, p. 1801, Sept. 1984.

[95] E. Andideh, I. Adesida, T. Brock, C. Caneau, and V. Keramidas, "Short-period gratings for long-wavelength optical devices," *J. Vac. Sci and Technol. B*, vol. 7, no. 6, p. 1841, Nov. 1989.

[96] I. Adesida, K. Nummila, E. Andideh, J. Hughes, C. Caneau, R. Bhat, and R. Holmstrom, "Nanostructure fabrication in InP and related compunds," *J. Vac. Sci. and Technol. B*, vol. 8, no. 6, p. 1357, Nov. 1990.

[97] B.-T. Lee, T. R. Hayes, P. M. Thomas, R. Pawelek, and J. P. F. Sciortino, "SiO_2 mask erosion and sidewall composition during CH_4/H_2 reactive ion etching of InGaAsP/InP," *Appl. Phys. Lett.*, vol. 63, no. 23, p. 3170, Dec. 1993.

[98] J. W. McNabb, H. G. Craighead, H. Temkin, and R. A. Logan, "Anisotropic reactive ion etching of InP in methane/hydrogen based plasmas," *J. Vac. Sci. and Technol. B*, vol. 9, no. 6, p. 3535, Nov. 1991.

[99] S. D. Hector, *Optimization of Image Formation in X-ray Lithography Using Rigorous Electromagnetic Theory and Experiments.* PhD thesis, Massachusetts Institute of Technology, 1994.

[100] P. S. Cross and R. V. Schmidt, "Coupled surface-acoustic-wave resonators," *Bell Sys. Tech. Journal*, vol. 56, no. 8, p. 1447, Oct. 1977.

[101] H. A. Haus and Y. Lai, "Narrow-band distributed feedback reflector," *J. of Light. Tech.*, vol. 9, p. 754, June 1991.

[102] J. Damask, "A new photonic device: The integrated resonant channel-dropping filter," Master's thesis, Massachusetts Institute of Technology, 1993.

[103] J. N. Damask, J. Ferrera, V. V. Wong, H. I. Smith, and H. A. Haus, "Limitations and solutions for the use of integrated $\lambda/4$-shifted distributed bragg resonators in wavelength-division multiplexing applications," in *International Symposium on Integrated Optics: Nanofabrication Technologies and Device Integration*, (Lindau, Germany), SPIE, 1994.

[104] J. N. Damask and H. A. Haus, "Wavelength-division demultiplexing using channel-dropping filters," *J. of Light. Tech.*, vol. 11, p. 424, 1993.

[105] J. N. Damask, "Spectral engineering of integrated resonant channel-dropping filters," to be published.

[106] J. N. Damask, "A stochastic analysis of the coherence-degradation effects of stitching errors along a DBR grating," to be published.

[107] J. N. Damask, "Phase-matching requirements for side-coupled bragg resonators," to be published.

[108] J. N. Damask, "Analysis of fabrication paradigms for synchronous side-coupled bragg resonators," to be published.

[109] E. Kratschmer, S. A. Rishton, H. E. Luhn, D. P. Kern, and T. H. P. Chang, "Piezo locking stage for nanometer electron-beam lithography," *J. Vac. Sci. Technol. B*, vol. 7, p. 1418, 1989.

[110] A. Moel, E. E. Moon, R. D. Frankel, and H. I. Smith, "Novel on-axis interferometric alignment method with sub-10 nm precision," *J. Vac. Sci. and Tech. B*, vol. 11, no. 6, p. 2194, Dec. 1993.

[111] R. M. Fano and A. W. Lawson, "Microwave filters using quarter-wave couplings," Tech. Rep. 8, Massachusetts Institute of Technology, Research Laboratory of Electronics, June 1946.

[112] R. M. Fano and A. W. Lawson, "Microwave filters using quarter-wave couplings," *Proc. IRE*, p. 1320, Nov. 1947.

[113] courtesy of Don Hofer IBM Almaden Research Center, San Jose, CA.

[114] V. V. Wong, J. Ferrera, J. N. Damask, T. E. Murphy, H. I. Smith, and H. A. Haus, "Distributed bragg grating integrated-optical filters: synthesis and fabrication," *to appear in Nov/Dec 1995 issue of J. of Vac. Sci. and Technol. B.*